Doctoral school: Science of Matter, Radiation and Environment

Discipline: Diluted media and fundamental optics

Dissertation

Development of an Atmospheric Pressure Interface for Analysis of Environmental Samples by Two-Step Laser Mass Spectrometry

by

Vikas MADHUR

Thesis submitted in partial fulfillment of the requirements for the degree of

Doctor of Philosophy of the University of Lille

Defended on 16 September 2024 in front of the defense committee composed of:

President of the committee:	
M. Cristian Focsa	Professor, Université de Lille
Reviewers:	
M. Fréderic Aubriet	Professor, Université de Lorraine, Metz
M. Silviu Gurlui	Professor, Université de Iasi, Roumanie
Examinators:	
M. Bérenger Gans	CNRS Research Fellow, Université Paris Saclay
Mme. Anne Zehnacker-Rentien	CNRS Research director, Université Paris Saclay
Thesis Director:	
M. Michael Ziskind	Associate Professor, Université de Lille
Thesis Co-Supervisors:	
M. Yvain Carpentier	Associate Professor, Université de Lille
M. Sébastien Legendre	Project Manager, Horiba France SAS, Loos

THESE

présentée à l'Université de Lille

pour l'obtention du titre de

DOCTEUR DE L'UNIVERSITE DE LILLE

Spécialité : Milieux dilués et optique fondamentale

Par

Vikas MADHUR

Développement d'une interface à pression atmosphérique pour l'analyse d'échantillons d'interêt environnemental par désorption laser, ionisation laser et spectrométrie de masse

Soutenue le 16 septembre 2024 devant la Commission d'Examen composée de:

Président du Jury:	
M. Cristian Focsa	Professor, Université de Lille
Rapporteurs:	
M. Fréderic Aubriet	Professeur, Université de Lorraine, Metz
M. Silviu Gurlui	Professeur, Université de Iasi, Roumanie
Examinateurs:	
M. Bérenger Gans	Chargé de Recherche CNRS, Université Paris Saclay
Mme. Anne Zehnacker-Rentien	Directrice de Recherche CNRS, Université Paris Saclay
Directeurs de thèse	
M. Michael Ziskind	Maitre de Conférences, Université de Lille
Co-encadrant:	
M. Yvain Carpentier	Maitre de Conférences, Université de Lille
M. Sébastien Legendre	Chef de Projet Horiba France SAS, Loos

Résumé

Les techniques de spectrométrie de masse fonctionnant le plus souvent sous vide poussé, l'analyse d'échantillon nécessite une phase de préparation et de manipulation qui peut s'avérer extrêmement délicate, en particulier pour les échantillons d'intérêt environnemental les plus volatils. Ces travaux visent précisément à concevoir et à optimiser une interface d'échantillonnage qui facilite le transfert d'échantillons de la pression atmosphérique à un environnement sous vide pour l'analyse par désorption laser/ionisation Laser/spectrométrie de masse à temps de vol (L2MS), connue pour sa sensibilité et sa sélectivité élevées. La spectroscopie Raman complètera cette analyse en fournissant des informations vibrationnelles détaillées sur les échantillons.

On étudiera différentes configurations pour l'interface en testant leur efficacité dans le transfert d'échantillons liquides et solides. Pour les échantillons liquides, deux configurations avec des vannes pulsées simples seront comparées, tandis que pour les échantillons solides, cinq configurations différentes impliquant une ou deux vannes seront évaluées et optimisées, en fonction de leur capacité à transférer efficacement et proprement les molécules dans la chambre à vide pour l'analyse. Ces travaux démontreront la capacité de l'interface à analyser divers échantillons modèles, en particulier des Hydrocarbures Aromatiques Polycyliques (PAH). L'étude soulignera également l'importance du chauffage et de la synchronisation entre les processus de désorption, d'ouverture des vannes, et d'ionisation afin d'optimiser les performances, de limiter la pollution de la chambre sous vide et de réduire les pertes lors du transfert.

Cette thèse contribuera également à la validation d'une technique de débromation d'échantillons de plastique contenant des retardateurs de flamme bromés en vue de leur recyclage et de leur valorisation. Pour l'occasion on comparera les spectres obtenus via le dispositif fonctionnant avec l'interface d'échantillonnage à pression atmosphérique au dispositif de pointe d'analyse sous vide disponible au laboratoire.

Mots-clés: spectrométrie de masse, desorption laser, ionisation laser, interface à pression atmosphérique, plastiques bromés, spectroscopie Raman

Abstract

Conventionnal MS techniques, which operate under high vacuum, pose challenges in sample preparation and handling, particularly for environmental samples. To address these issues, this research focuses on designing and optimizing a sampling interface that facilitates the transfer of samples from atmospheric pressure to a vacuum environment for MS analysis.

The study employs Two-Step Laser Mass Spectrometry (L2MS) as the primary analytical techniques. L2MS, known for its high sensitivity and selectivity, couples laser desorption and laser ionization with Time-of-Flight (ToF) mass spectrometry, allowing precise analysis of chemical compositions. Raman Spectroscopy complements this by providing detailed vibrational information about the samples.

The research explores various configurations for the sampling interface, testing their effectiveness in transferring both liquid and solid samples. For liquid samples, two configurations with single valves are compared, while for solid samples, five different setups involving one and two valves are evaluated. These configurations are assessed based on their ability to transfer molecules efficiently into the vacuum chamber for MS analysis.

This work demonstrates the ability of the interface to analyze various model samples, in particular Polycyclic Aromatic Hydrocarbons (PAH). The study also highlights the importance of heating and synchronization between the desorption, valve opening and ionization processes in order to optimize performance, limit pollution of the vacuum chamber and reduce transfer losses.

This thesis also contributes to the validation of a technique for debrominating plastic samples containing brominated flame retardants, with a view to their recycling and recovery. For this purpose, the spectra obtained using the atmospheric pressure sampling interface will be compared with the state-of-the-art vacuum analysis system available in the laboratory.

Keywords: laser desorption, laser ionization, mass spectrometry, atmospheric pressure sampling interface, brominated plastics, Raman spectroscopy

Acknowledgements

When I started my PhD, I had no clear understanding of what it would involve or how I would manage the financial, administrative, and emotional challenges. I was new to both the PhLAM lab and the environment, and there was an initial fear of not knowing anyone or how I would adapt. However, after meeting Dr. Yvain Carpentier, I gained the confidence to move forward, and his support has been crucial whenever I faced doubts. I am deeply grateful to have had him as one of my supervisors.

I would also like to sincerely thank my main supervisor, Dr. Michael Ziskind, for his guidance and support throughout my thesis. I am thankful for my collaboration with HORIBA Scientific and the assistance from my supervisor Dr. Sébastien Legendre. I am fortunate to have worked alongside exceptional colleagues such as Dr. Claire Pirim, and postdocs Dmitrii Egorov, Tirhthankar Mitra, and Venkateshwar Rao in the PhLAM team.

It is an honor to have had the opportunity to present my work to the defense committee. I extend my heartfelt thanks to Prof. Frédéric Aubriet, Prof. Silviu Gurlui, Prof. Cristian Focsa, Dr. Berenger Gans, and Dr. Anne Zehnacker-Rentien for reviewing and evaluating my PhD thesis. I am particularly grateful to Prof. Frédéric Aubriet and Prof. Silviu Gurlui for their dedication in reviewing my manuscript.

My deepest thanks go to the members of CERLA, especially the technical and administrative staff, including Benedicte Calimet and Marc Le Parquier, for their support throughout my journey.

I am also incredibly grateful to my lab friends—Siveen Thlaijeh, Kawssar Haider, Joelle Al Aseel, and Christelle Hanoun—for the engaging discussions and coffee breaks that kept me motivated.

I would also like to thank my friend Junaid Akhter, who supported me during the early days of my master's studies in France. I could not have completed this journey without the constant support and encouragement of my friends: Shubham Semwal, Jash Mehta, Akash Naik, Smita Panda, Parvathy Sarma, Ganesh Jabotra, Priya Rane, Sravan Kumar, and especially Simon Verbeke, who was a great support toward the end of my thesis.

Finally, I am profoundly grateful to my family for their unwavering belief and support, which has been my strength throughout this process. Their constant encouragement, even during the toughest times, has been my foundation. I am forever thankful to my parents, my brother, and my sister.

Table of Contents

List of Acronyms

ABS	acrylonitrile butadiene styrene
AFM	atomic force microscopy
AP	atmospheric pressure
API	atmospheric pressure interface
BFR	brominated flame retardant
BPA	bisphenol A
CBI	corona beam ionization
CI	chemical ionization
CID	collision induced dissociation
DAPI	discontinuous atmospheric pressure interface
DBD	dielectric barrier discharge
DBDE	decabromodiphenyl ether
DBDI	dielectric barrier discharge ionization
DESI	desorption electrospray ionization
DHB	dihydrobenzoic acid
DHB	2,5-Dihydrobenzoic Acid
EASSI	easy ambient sonic spray ionization
EEE	electrical and electronic equipment
EI	electron Ionization
ELDI	electrospray laser desorption ionization
ESI	electrospray ionization
HBCD	hexabromocyclododecane
HIPS	high impact polystyrene
HR	high resolution
ICR	ion cyclotron resonance
ICS	intensity correction system
IMS	imaging mass spectrometry

L2MS	two step laser mass spectrometry
LA	laser ablation
LADBDE	laser ablation dielectric barrier discharge
LAESI	laser ablation electrospray ionization
LC	liquid chromatography
LD	laser desorption
LDI	laser desorption/ionization
MALDESI	matrix assisted laser desorption electrospray ionization
MALDI	matrix assisted laser desorption/ionization
MCP	microchannel plate
MPI	multiphoton ionization
MS	mass spectrometry
MSI	mass spectrometry imaging
Nd:YAG	neodymium-doped yttrium aluminum garnet
OBDE	octabromodiphenyl ether
OD	outer diameter
PAH	polycyclic aromatic hydrocarbon
PBDE	polybrominated diphenyl ether
PC	polycarbonate
PCB	printed circuit board
PEEK	polyether ether ketone
PFTBA	perfluorotributylamine
PIRL	picosecond infrared laser desorption
PMT	photomultiplier tube
PSI	paper spray ionization
PTFE	polytetrafluoroethylene
QMS	quadrupole mass spectrometer
R2PI	resonance two photon ionization
REMPI	resonance enhanced multiphoton ionization
RF	radiofrequency

RIT	rectilinear ion trap
SF	space focus
SICRIT	soft ionization by chemical reaction in transfer
SIMS	secondary ion mass spectrometry
SNOM	scanning near field optical microscopy
SPI	single photon ionization
SR	Standard resolution
TBBPA	tetrabromobisphenol A
ToF	time of flight
UV	ultraviolet
WEEE	waste electrical and electronic equipment

List of Figures

List of Tables

Chapter 1 Introduction

Over the years, with the advancement of technology, Mass spectroscopy (MS) has been widely used as a tool to accurately identify, quantify, and characterize molecules based on their mass, structure and fragmentation pattern.

Based on the needs, MS can be performed using different techniques. Apart from the different types of MS, the environment in which MS is performed is very important as it changes the instrument's performance and application. MS can be either performed in vacuum or atmospheric conditions. In Vacuum Mass Spectrometry, the MS process occurs in an environment with low pressure. This has several advantages such as reduced collisions between ions and gas molecules, resulting in good resolution as it minimizes the broadening of ion peaks. This results in enhanced resolution with extended mass range. In Atmospheric Pressure Mass Spectrometry, the MS occurs at or near atmospheric pressure. Without the need for creating a vacuum, this method greatly simplifies sample handling, making MS more accessible for routine analyses. Additionally, this also removes the complexity of sample preparation and lastly, MS at atmospheric conditions allows for real-time monitoring. These important factors contribute to making atmospheric MS invaluable for environmental analysis such as monitoring air quality, detecting pollutants and also for clinical studies such as testing of tissues and bodily fluids without the need for extensive preparation of the sample.

Usage of MS at atmospheric pressure can help us unravel the molecules present in the air we breathe, the water we drink, and the soil beneath our feet. All can have a direct impact on the crisis we are facing in the 21st century with the increasing pollution. This thesis is aimed towards developing a new coupling instrument for MS analysis environmental samples at atmospheric pressure.

This project has been done in collaboration with HORIBA Scientific and PhLAM (Physique des Lasers, Atomes et Molécules) Laboratory at the University of Lille. HORIBA Scientific is invested

in advancing precision instrumentation and aims to bring cutting-edge solutions to diverse scientific domains. The company globally leads the manufacturing of instruments and optical equipment. The PhLAM laboratory at the University of Lille is a dynamic research lab specializing in laser physics, atomic and molecular physics, and related interdisciplinary areas. The ANATRAC (Traces Analysis) group of PhLAM, aim to investigate physiochemical properties of aerosols. The collaborative efforts between industry and academia have resulted in this thesis. Through analysis and instrumental development, this thesis aims to create a novel device that will not only advance scientific knowledge but also contribute to real-world applications.

In Chapter 2, we explore different MS techniques and lay the groundwork for understanding the state of the art in MS technology and its revolutionary potential in atmospheric studies. In the same chapter, we navigate through the current state of the art of MS and give a more comprehensive view of a few MS techniques and its components along with their working principle.

Materials and methods used to advance MS techniques have been explained in Chapter 3. The focus is on two step laser mass spectrometry (L2MS), highlighting the experimental setups and devices employed to acquire signals. This chapter also covers Raman Spectroscopy, a complementary technique that provides detailed chemical information through vibrational analysis of samples by identifying the chemical bond, functional group and molecular structure.

Chapter 4 delves into the development of the atmospheric interface for transferring samples from atmospheric pressure to a vacuum for analysis. Various configurations and their effectiveness are evaluated through experiments with different chemical samples, both liquid and solid.

In Chapter 5, the thesis examines the Raman and MS analysis of plastics, particularly focusing on Brominated Flame Retardants (BFRs). This chapter includes experiments that confirm the removal of bromine from plastic samples. It also provides an initial comparison between the atmospheric pressure mass spectrometer presented in the previous chapter and a cutting-edge mass spectrometer operating under ultra-high vacuum.

Finally, Chapter 6 presents the overall conclusions and perspectives of the research, summarizing the advancements made and suggesting future directions for further enhancing atmospheric pressure mass spectrometry.

Chapter 2 State of the Art

2.1 Mass Spectrometry

Mass Spectrometry (MS) has widespread applications in modern science, from analyzing atmospheric particulates [1] to detecting trace amount of illicit drugs or explosives [2], from identifying proteins in human and fossils [3] to diagnosing tumor cells in living beings [4] and performing molecular analyzes at sub-cellular level [5]. Mass spectrometry (MS) has long been a keystone of analytical chemistry, serving as a powerful tool for the identification and quantification of molecules across a diverse range of applications.

The core principle underlying mass spectrometry involves the ionization of chemical compounds, resulting in the generation of charged molecules or molecular fragments and atoms. These ions are subsequently measured based on their mass-to-charge ratios (*m/z*) allowing the determination of molecular mass (see Figure 2.1).

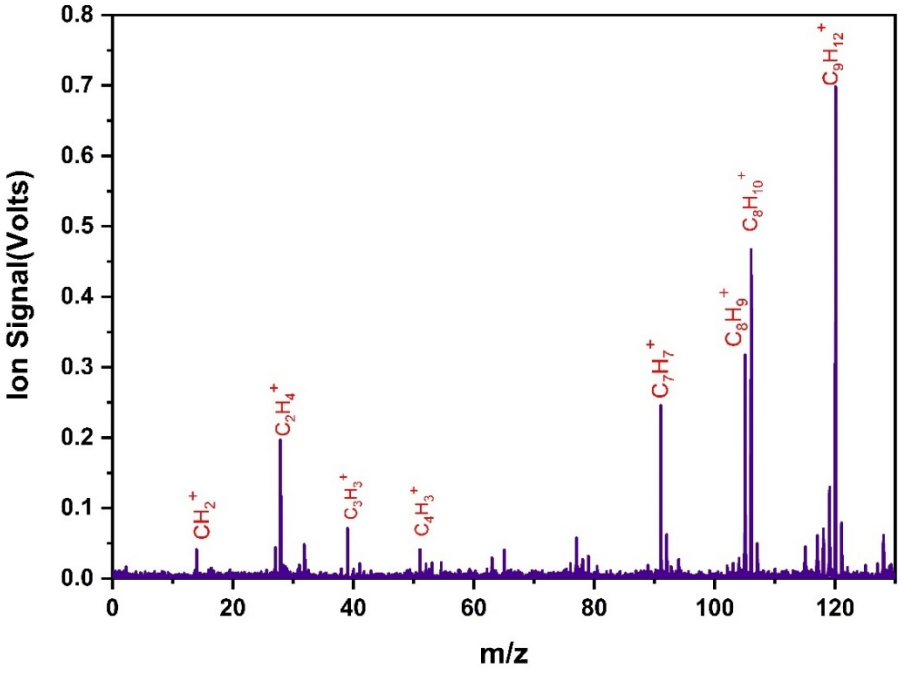

Figure 2.1 Typical Mass Spectrum of kerosene showing the separation of ions based on their mass to charge ratio.

A standard mass spectrometer [6] comprises three fundamental components (see Figure 2.2): an ion source responsible for effectively ionization, a mass analyzer that facilitates the precise

separation of ions, and a detector engineered to discern and quantify the generated ions. Notably, detectors, mass analyzers, and certain ion sources operate within high-vacuum conditions. This vacuum setup allows ions to move freely without colliding with other gas molecules or atoms. Maintaining this vacuum is important for accurate and precise measurements. Sample molecules are inserted into the vacuum chamber of the instrument through a sample inlet.

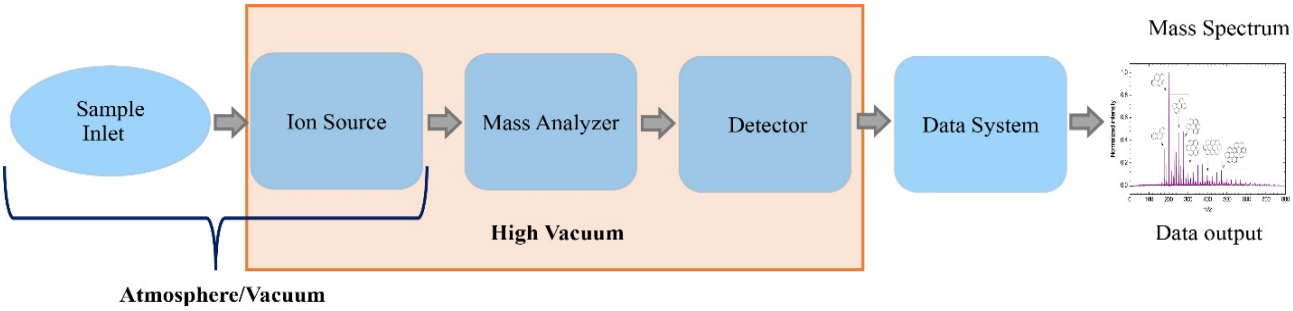

Figure 2.2 Schematic diagram of the mass spectrometry technique.

The ionization of compounds can be accomplished through various methods, which are determined by the chemical characteristics of the substances being analyzed, the desired level of sensitivity for detection, and the analytical method in use. Beyond selecting the appropriate ionization source, there are also a range of mass analyzers to choose from. Furthermore, different types of detectors are employed to convert the ionic current, which has traversed the analyzer, into an analyzable signal. Subsequent sections will delve into these components in a comprehensive manner.

2.1.1 Ionization Source

In the realm of mass spectrometry, the ionization process stands as the crucial first step, where complex molecules are transformed into ions for subsequent analysis. The choice of an appropriate ionization source profoundly influences the sensitivity, selectivity, and overall success of a mass spectrometric analysis.

Principles of Ionization

Ionization in mass spectrometry involves the conversion of neutral molecules into ions. The ionization methods employed range from "soft" techniques, which preserve molecular structures, to "hard" methods causing extensive fragmentation [7].

Classification of Ionization Sources

- **Electron Ionization (EI)**

In electron ionization, a beam of electrons is directed towards the sample, causing the ejection of electron from the sample molecules in the gas phase and generating positively ions [8]. The high-energy electrons can cause fragmentation of the sample molecules, resulting in the formation of fragment ions, which makes it a hard ionization technique. Electron ionization is widely used in various applications, including the analysis of organic compounds, identification of unknown substances, and determination of isotopic composition. This ionization process can be represented by the following reaction:

$$M + e^- \rightarrow M^+ + 2e^-$$

Where M represents the neutral molecule, e^-represents the high energy electron, M^+ represents the resulting positive ion.

- **Electrospray Ionization (ESI)**

Electrospray Ionization (ESI) is a soft ionization method in mass spectrometry where a liquid sample transforms into charged droplets [9]. In this technique, a liquid sample is introduced into the ionization source, typically through a capillary or needle. A high voltage is applied to the capillary, creating an electric field that causes the liquid to form a fine spray of charged droplets. As the droplets move through the source, solvent molecules evaporate, leaving behind multicharged analyte ions. These ions are then drawn into the mass spectrometer for analysis. ESI is particularly useful for analyzing large and polar molecules, such as proteins and peptides, since *z* could be high (10 to 20 is easily reachable), *m/z* is often low, even for heavy molecules, and thus is easily accessible to a ToF/MS. Moreover, series of multicharged peaks are often observed for the same species, which could facilitate its assignment.

- **Chemical Ionization (CI)**

Chemical Ionization (CI) is a technique in mass spectrometry where a reagent gas is ionized to create ions [10],[11] . These ions then react with the sample molecules, leading to their ionization. Unlike Electron Ionization (EI), which uses high-energy electrons, CI involves softer ionization, causing less fragmentation of the sample molecules.

In CI, the sample is introduced into the ionization source along with a reagent gas. The gas is ionized, forming reactant ions. These reactant ions then collide with the sample molecules, leading to the formation of ionized analyte molecules. CI is particularly useful for analyzing polar and non-volatile compounds [12], as well as large biomolecules like proteins and carbohydrates, due to its gentle ionization process. It minimizes fragmentation, allowing the analysis of intact molecules, and is effective for substances that are difficult to vaporize, preserving their structural integrity for accurate identification and quantification.

- **Matrix-Assisted Laser Desorption/Ionization (MALDI)**

Matrix-Assisted Laser Desorption/Ionization (MALDI) is a powerful ionization technique used to analyze large biomolecules polymers and organic compounds. In MALDI, the sample is mixed with a matrix, which absorbs the laser energy and helps ionize the sample molecules [13], [14].
First, the sample-matrix mixture is deposited on a target surface. When the target is irradiated with a laser, the matrix absorbs the laser energy, vaporizes, and transfers energy to the sample molecules. This energy causes the sample molecules to ionize, forming ions. These ions are then accelerated into the mass spectrometer for analysis in the case of ToF/MS.
MALDI is especially valuable for analyzing proteins, peptides, nucleic acids, and other large biomolecules polymers. It enables researchers to study complex biological samples and obtain detailed information about their composition. The technique's ability to handle high-mass molecules and provide precise molecular weight measurements makes it a widely used method in various scientific fields, including proteomics, genomics, and drug discovery.

- **Electrospray Laser Desorption Ionization (ELDI)**

ELDI is a technique that combines the principles of electrospray ionization and laser desorption to enable the direct, sensitive, and rapid analysis of chemical compounds on sample surfaces. In ELDI, a laser is used to desorb and ionize the sample, while the electrospray process facilitates the generation of ions from the sample. For enhanced ionization, fine carbon powders suspended in the solution are often used to assist in creating a uniform surface for laser desorption, which helps in the efficient transfer of energy to the sample. This technique is capable of characterizing both polar and nonpolar compounds dissolved in solvents, making it versatile for various types of analyses. ELDI has been applied in the rapid analysis of solid materials under ambient conditions

and is effective in detecting proteins and synthetic organic compounds. As a soft ionization technique, ELDI minimizes fragmentation.

- **Secondary Ions Mass Spectrometry**

Secondary Ion Mass Spectrometry (SIMS) is an analytical technique used to characterize the elemental and isotopic composition of sample with high sensitivity and spatial resolution. In SIMS, a focused primary ion beam bombards the sample surface, causing the ejection of secondary ions [15]. These secondary ions are then analyzed in a mass spectrometer to determine their mass-to-charge ratio.

The primary ions used in SIMS are typically energetic and can penetrate the surface of the sample. Upon impact, they sputter atoms and molecules from the surface, creating a plume of secondary ions. SIMS can provide detailed information about the elemental and isotopic composition, as well as the chemical structure of the surface layers of materials.

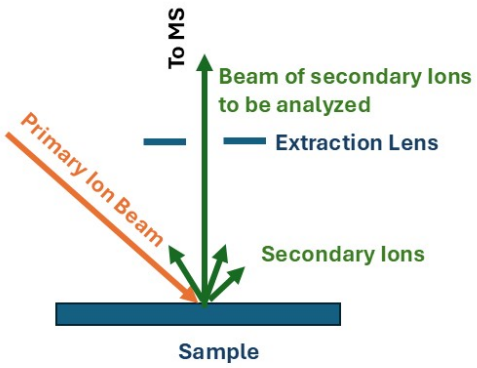

Figure 2.3 Schematic depiction of SIMS

- **Photoionization**

Photoionization is a process in mass spectrometry where photons, typically in the ultraviolet range, are used to ionize atoms or molecules. When photons with sufficient energy are absorbed by the sample, they can remove electrons from the atoms or molecules, resulting in the formation of positive ions [16].

In photoionization, the sample is exposed to a beam of photons with specific energy levels. When the photons interact with the sample, they transfer energy to the electrons, allowing them to overcome the binding energy of the atoms or molecules [17]. As a result, electrons are ejected,

leading to the formation of positive ions. These ions can then be analyzed in a mass spectrometer to determine their mass-to-charge ratio.

Photoionization is particularly useful for ionizing samples with low ionization potentials. It is commonly used in research areas such as spectroscopy, analytical chemistry, and environmental analysis, providing valuable information about the composition.

Table 2.1: Comparison of Various Ionization Techniques in Mass Spectrometry: An Overview of Their Principles, Advantages, and Disadvantages.

Ionization Technique	Principle	Advantages	Disadvantages
Electron Ionization (EI)	A beam of high-energy electrons is directed towards the sample, causing ionization and fragmentation.	Widely applicable for organic compounds; provides detailed fragmentation patterns aiding structural elucidation.	Can cause extensive fragmentation, making it difficult to identify the molecular ion; not suitable for large, non-volatile, or fragile molecules.
Electrospray Ionization (ESI)	A liquid sample is transformed into charged droplets, which are then desolvated, leaving behind charged analyte ions.	Suitable for large and polar molecules; produces multiply ions, facilitating the analysis of high-mass molecules.	Limited by the solvent and sample preparation; can be affected by ion suppression in complex mixtures.
Chemical Ionization (CI)	A reagent gas is ionized, and these ions then react with the sample molecules to ionize them.	Softer ionization than EI, leading to less fragmentation; good for analyzing intact molecules of polar and non-volatile compounds.	Requires careful selection of the reagent gas; less informative for structural elucidation due to reduced fragmentation.
Matrix-Assisted Laser Desorption/Ionization (MALDI)	The sample is mixed with a matrix that absorbs laser energy, aiding in the desorption and ionization of the sample.	Ideal for large biomolecules; allows analysis of proteins, peptides, and other macromolecules with minimal fragmentation.	Matrix selection is critical

Electrospray Laser Desorption Ionization (ELDI)	Combines electrospray ionization and laser desorption to ionize molecules from sample surfaces.	Enables direct analysis of compounds on surfaces; can handle both polar and nonpolar compounds.	Relatively new technique; might require specialized equipment and optimization for best results.
Secondary Ion Mass Spectrometry (SIMS)	Uses a primary ion beam to sputter secondary ions from the surface of a sample for analysis.	High sensitivity and spatial resolution; capable of surface analysis and depth profiling.	Can cause sample damage; quantitative analysis can be challenging due to matrix effects.
Photoionization	Photons are used to ionize atoms or molecules by ejecting electrons.	Effective for ionizing species with low ionization potentials; produces minimal fragmentation.	Requires photons of precise energy; not suitable for all types of samples, especially those requiring higher energy for ionization as it needs vuv laser.

2.1.2 Mass Analyzer

With the development of ionization sources capable of vaporizing and ionizing molecules, enhancing mass analyzer performance in terms of speed, accuracy, and resolution has become essential. In the early 20th century, the first mass analyzers utilized magnetic fields to differentiate ions based on their path curvature within the magnetic field. Modern mass analyzers have undergone significant design changes in recent years, now providing much higher accuracy, increased sensitivity, and a broader mass range. As ionization techniques have advanced, mass analyzers have had to adapt to meet the demands of analyzing a diverse array of samples.

There are different types of mass analyzers, categorized based on how ions are introduced: continuous mode allows a constant flow of ions, while pulsed mode introduces ions at specific intervals. Pulsed mode typically accumulates ions from a continuous flow, releasing them in pulses.

In addition to single mass analyzers like magnetic sectors, quadrupoles, and time-of-flight (ToF) analyzers, hybrid systems (MS/MS) have gained prominence. Quadrupole analyzers have become popular due to their cost-effectiveness. Ion trap MS temporarily accumulates ions before separating them, while tandem/hybrid MS systems combine multiple units to achieve specific analytical goals. Each of these mass analyzers has distinct features, advantages, and drawbacks,

making them suitable for different applications. This section delves into the principles governing these analyzers, comparing their characteristics and applications.

- **Time-of-Flight (ToF) MS**

Time-of-Flight Mass Spectrometry (ToF MS) operates as a pulsed and non-scanning mass spectrometer, featuring a design comprising an accelerator, a field-free region, and a detector housed in a high vacuum chamber called a flight tube (refer to Figure 2.4)

In ToF MS, ions with different mass-to-charge ratios (*m/z*) are separated and detected based on the time they take to travel through a field-free region [6]. Initially, ions generated in an ionization region are accumulated and sent into the flight tube in pulses. Here, they receive acceleration through a high voltage applied between electrodes.

The kinetic energy (K.E.) of these ions can be expressed as follows:

$$KE_{ion} = \frac{1}{2}mv^2 = zeV \tag{2.1}$$

Where m is mass of the ion and v is velocity of the ion, z is charge of the ion, e is elementary charge, and V is acceleration voltage applied to ions.

With a constant acceleration voltage and kinetic energy, each ion travels at its unique velocity inside the flight tube. Lighter ions exhibit higher velocities, reaching the ion detector faster, while heavier ions travel at comparatively lower speeds.

The time of flight (T) is directly proportional to the square root of *m/z*.

$$T = \frac{distance}{velocity} = \sqrt{\frac{m}{z}} \times \frac{L}{\sqrt{2eV}} \tag{2.2}$$

In other words, for a fixed flight distance (L), ions with smaller *m/z* values reach the detector before those with larger *m/z* values. By maintaining consistent parameters, the time of flight (T) translates directly into *m/z*, thereby generating a mass spectrum in ToF MS. Remarkably, ToF MS has no time-of-flight limit, theoretically enabling measurement across an unlimited mass range.

Due to its operational principle, ToF MS systems introduce ions into the analyzer only after the previous group has reached the detector. Consequently, ToF MS aligns well with ionization methods that ionize molecules in pulses, like laser ionization. Advancements that minimize

differences in ion kinetic energy, including the use of reflectron and pulsed extraction methods, have elevated ToF MS systems for high-resolution mass spectrometry applications.

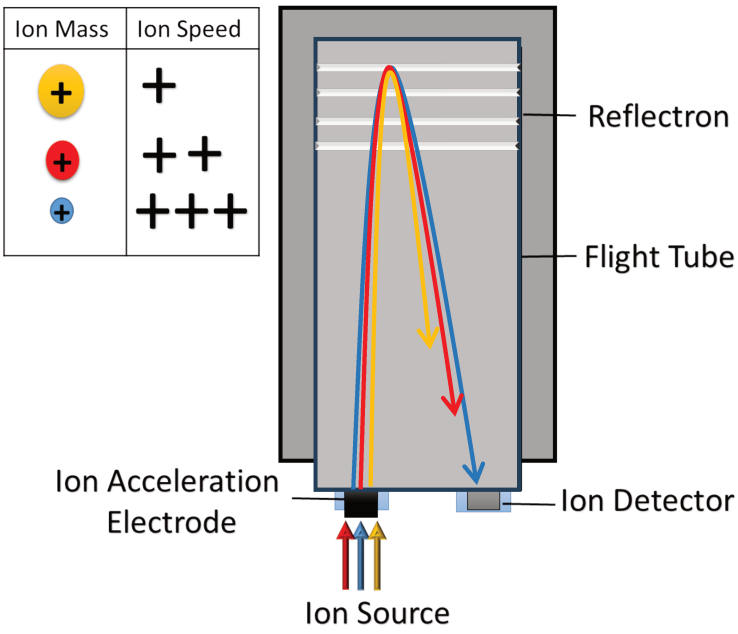

Figure 2.4 Schematic of a ToF MS

- **Magnetic Sector MS**

The magnetic sector mass spectrometer, a long-standing and historically significant continuous mass spectrometry model, employs magnetic fields to sort ions based on their mass-to-charge ratios (*m/z*) (see Figure 2.5). Initially, high voltage accelerates the ions into the magnetic sector. Here, they encounter a magnetic field, leading to deflection according to Fleming's left-hand rule (Fleming's left-hand rule can predict the direction/force of the movement when there is an electric current moving in an applied magnetic field). As a result, ions are accelerated in a direction perpendicular to the current and magnetic field, resulting in a curved deflection path for the ions in the magnetic sector MS. This deflection varies based on their *m/z*, with lighter ions experiencing greater deflection [6].

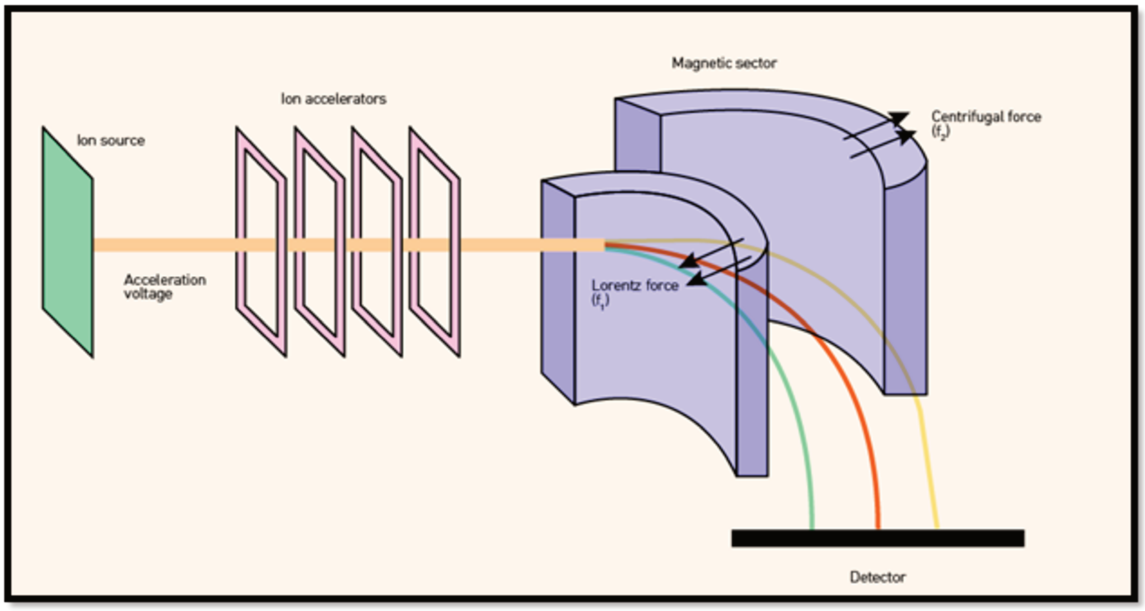

Figure 2.5 Schematic of magnetic sector.

Ions experience a Lorentz force (f_1) due to the magnetic field.

$$f_1 = Bzev \tag{2.3}$$

In equation (2.3), *B* is magnetic flux density, *z* is charge of the ion, e is elementary charge, and *v* is velocity of the ion.

Additionally, as ions change direction, a centrifugal force (f_2) from the curved path acts on them.

$$f_2 = \frac{mv^2}{r} \tag{2.4}$$

In equation (2.4), m is mass of the ion, and r is path radius.

To reach the detector, these forces must balance, requiring ions to travel along a curved path with a specific radius (r)

$$f_1 = f_2 = Bzev = \frac{mv^2}{r} \tag{2.5}$$

The ions' kinetic energy due to acceleration voltage V applied to ions is represented as

$$KE_{ion} = \frac{1}{2}mv^2 = zeV \tag{2.6}$$

By eliminating ion velocity (v), Equations (2.5) and (2.6) simplify into Equation (2.7).

$$\frac{m}{z} = \frac{eB^2r^2}{2V} \tag{2.7}$$

Magnetic flux density (B) scanning while maintaining constant acceleration voltage (V) and path radius (r) enables detection of various masses (m) along the same path.

In practice, a single ion detector is used, with magnetic flux density (B) being scanned while acceleration voltage (V) and path radius (r) remain constant. Consequently, ions of different masses (m) pass through the magnetic field sequentially, generating individual mass spectra per scan. This process defines the ion transmission and scanning mode of magnetic sector mass analyzers. Additionally, there are dual-focusing mass spectrometers combining both electric and magnetic sectors, enhancing mass resolution by converging ions of identical mass.

Magnetic sector mass spectrometers offer high resolution and dynamic range, typically ranging from 10 to 10,000 $m/\Delta m$ (depending on acceleration voltage and instrument design). Single-focusing models can achieve resolutions around 2000 $m/\Delta m$, while dual-focusing models reach tens of thousands. Previously, only dual-focusing magnetic sector spectrometers could achieve such high resolutions before the emergence of high-performance time-of-flight (ToF) and ion-cyclotron-resonance (ICR) mass spectrometers.

Despite their capabilities, enhancing magnetic sector mass spectrometers requires raising magnetic field strength, leading to larger and costlier systems. Additionally, these systems demand an exceptionally high vacuum level of 10^{-8} mbar, posing challenges for further development.

- **Quadrupole MS**

The single quadrupole mass analyzer functions by scanning ions and facilitating their transmission. It consists of four parallel cylindrical metal rods with hyperboloidal interiors, positioned equidistantly from the center axis within a vacuum chamber (refer to Figure 2.6). Direct current (D.C.) and high frequency alternating current, or radiofrequency (RF), are applied to the quadrupole. This configuration allows ions with specific (*m/z*) to pass through the quadrupole and reach the detector. The detected ions are then converted into a signal and sent to a computer for further analysis.

Initially, ions produced in the ionization unit are accelerated in the z-direction (as indicated by the green arrow in Figure 2.6) using a relatively low voltage of a few dozen volts. These ions pass through a small opening and enter the quadrupole. Diagonally opposite poles receive voltage of the same polarity, while adjacent poles have opposite voltage polarities, represented gray rods in Figure 2.6. When a combination of direct current and high-frequency alternating current is applied to these poles, it creates an electric field with a rapidly varying phase within the quadrupole. Consequently, ions passing through this field oscillate in the x- and y-directions. By adjusting specific parameters, ions within a particular *m/z* range maintain stable oscillations (resonance ions) and successfully pass through the quadrupole to reach the detector (as shown in Figure 2.6). In contrast, ions with different *m/z* values experience unstable oscillations (non-resonance ions), leading them to collide with the poles, exit the system, and remain undetected.

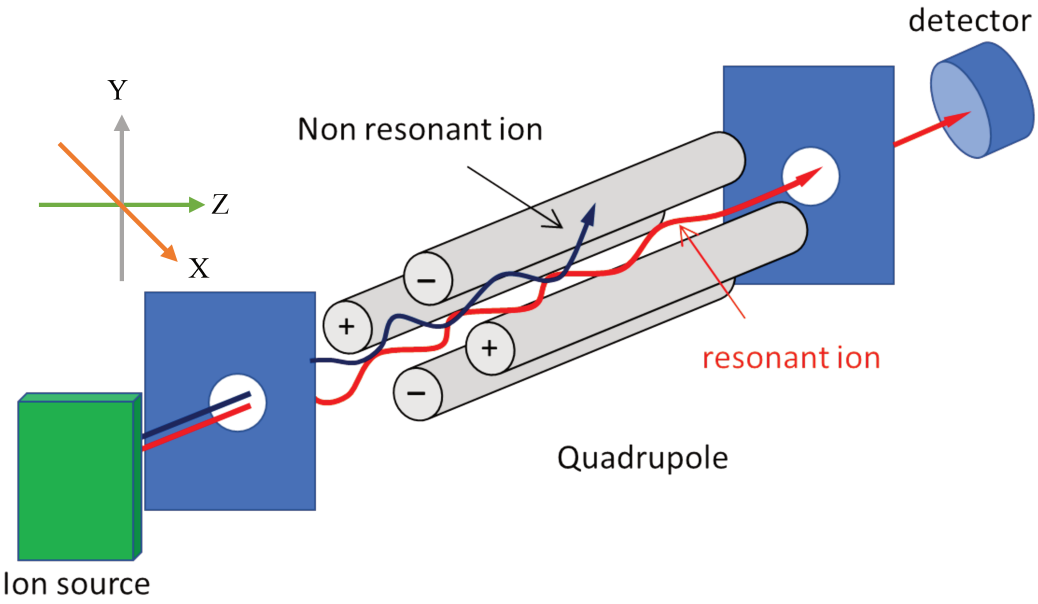

Figure 2.6 Schematic of Quadrupole MS functioning.

In a quadrupole mass spectrometer, the oscillation of ions follows the Mathieu Equation (Equation 2.8), whatever their initial velocity or position.

$$\frac{m}{z} = K\frac{V}{r^2\omega^2} \tag{2.8}$$

Where, *m* is mass of the ion, *z* is charge of the ion, *K* is constant, *V* is applied voltage, *r* is effective distance between the electrodes and ω is oscillation frequency.

Figure 2.7 serves as a visual representation of how this equation is solved, essentially depicting the Mathieu stability diagram. This diagram outlines the stable regions for ions within a quadrupole MS system.

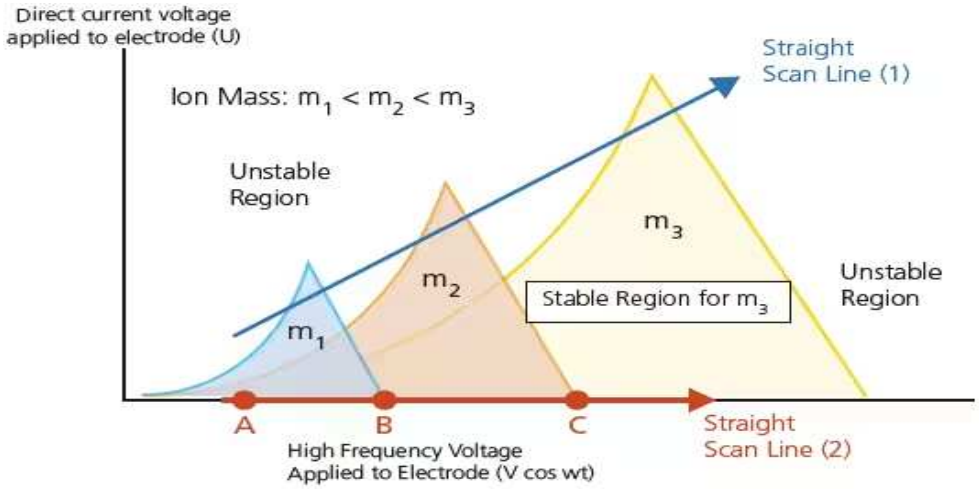

Figure 2.7 Mathieu stability diagram for the quadrupole MS system's stable ion regions [18].

The shaded areas in Figure 2.7 highlight the specific conditions necessary for stable ion oscillation, dictated by the mass and oscillation frequency of the ions, as defined in the Mathieu Equation [6]. Each shaded region corresponds to different ion masses, such as m_1, m_2, and m_3. By adjusting the voltage while maintaining a constant ratio between direct current voltage (on the y-axis) and high frequency alternating current voltage (on the x-axis), a linear scan line 1 is achieved. This scan line traverses through the respective stability regions for ions with masses m_1, m_2, and m_3. Consequently, these ions pass through the quadrupole sequentially in the same order (m_1, m_2, and m_3). This process results in a mass spectrum that covers ions with masses ranging from small to large.

Quadrupole Mass Spectrometer (MS) boasts a compact design, robustness, and affordability, making them widely used as general-purpose analytical instruments. Unlike other MS systems that require high vacuum levels, quadrupole MS can function effectively at lower vacuum levels (around 10^{-2} to 10^{-3} Pa) due to their efficient ion transmission design, and lower sensitivity to collisions.

Quadrupole MS systems offer excellent scan speed and sensitivity, with a maximum scan speed of 15,000 amu per second, enabling faster measurements compared to magnetic sector MS. Their

mass range extends up to 2000 *m/z*, allowing qualitative analysis within a practical range of molecular masses.

- **Ion Trap MS**

The ion trap mass spectrometer operates on principles somewhat like the quadrupole system but with notable distinctions. An ion trap typically comprises a ring-shaped electrode positioned between two end-cap electrodes, with an ionization unit at the entrance and a detector at the exit. While the ring electrode serves as an entrance and exit, it operates differently from the voltage-controlled quadrupole system. In an ion trap, the electrodes are typically not voltage-biased, resulting in ion movement along the horizontal axis.

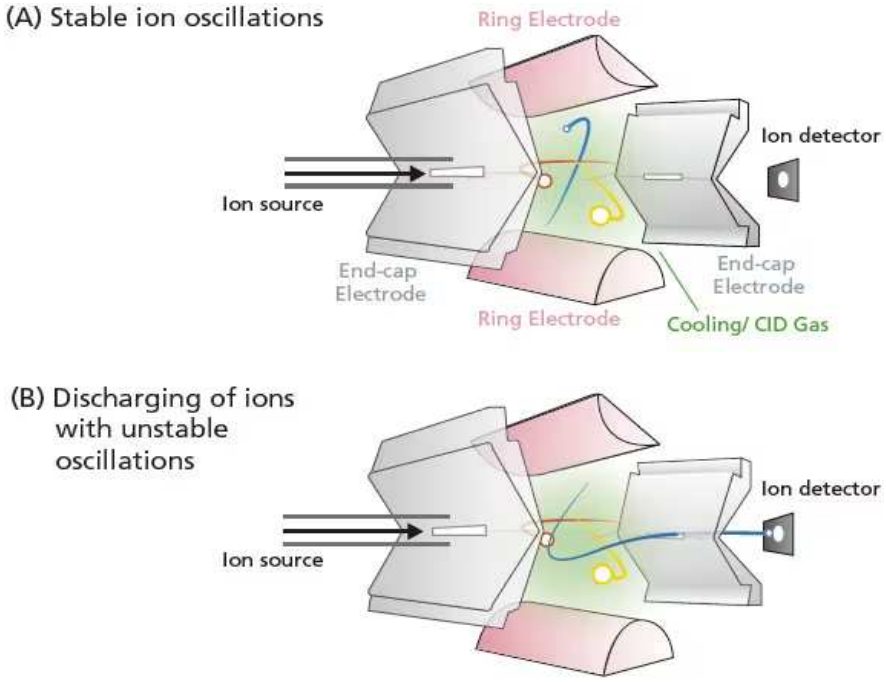

Figure 2.8 Diagram of Ion Trap MS [18].

During the analysis process, the end-cap electrodes are initially grounded, followed by the application of a low radiofrequency (RF) voltage to the ring electrode. Ions are introduced into the trap in a pulse mode, temporarily confining all of them within the electrode. Within the trap, ions of varying mass engage in stable oscillations. To detect a specific ion, the RF voltage gradually increased. As the voltage rises, the oscillations of ions with a precise mass-to-charge ratio become unstable, causing them to be discharged through an aperture in one of the end-cap electrodes.

In contrast to quadrupole systems, where oscillating ions pass through the quadrupole to reach the detector, ion trap systems separate and detect ions by discharging those with unstable oscillations from the system into the detector [6].

Advantages of ion traps are that they are compact in size, relatively cheap, and have good sensitivity and mass resolution.

- **Orbitrap MS**

The Orbitrap mass analyzer takes elements from various other types of mass analyzers. It comprises two cup-shaped outer electrodes and a spindle-like central electrode, electrically isolated from each other. By applying voltage between the outer and central electrodes, a linear electric field forms along the axis, with a strong radial component attracting ions toward the central electrode [6]. Ions are introduced tangentially between the central and outer electrodes through a slot in one of the outer electrodes.

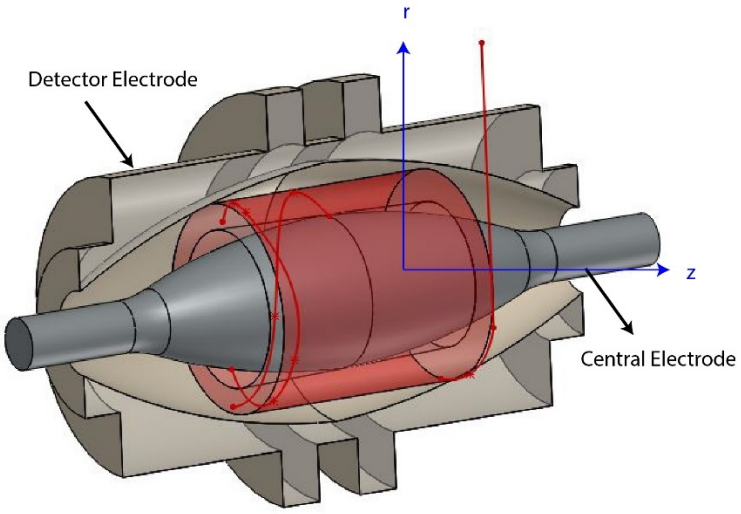

Figure 2.9 Schematic of Orbitrap MS adapted from [19].

Gradually increasing the voltage on the inner electrode increases the electric field, causing ions to move closer to the inner electrode until they reach a desired orbit within the trap. Once in orbit, the electric field stabilizes, the ions move with different rotational frequencies, but their axial frequency remains constant. This results in ions of specific mass-to-charge ratios forming rings that oscillate along the inner spindle in circular orbits.

A radial electric field created by voltage between the central and outer electrodes bends ion trajectories toward the central electrode, countered by tangential velocity producing a centrifugal force [20]. With specific parameters, ions maintain nearly circular spirals, or orbits, inside the trap. The conical shape of the electrodes generates an axial electric field that guides ions toward the widest part of the trap. Outer electrodes are utilized for current detection. The digitized image current (As an ion approaches a piece of metal, it will induce an increasing "image charge" on said metal. For example, as positive ions approach a piece of metal, negative charges build up on the surface due to electrostatic attraction. As the ions get closer and closer to the metal, more charges build up on the surface. This increase in image charge is referred to an "image current". Conversely, as positive ions move away from the piece of metal, the amount of negative charge on the surface will decrease, causing an image current in the opposite direction.) in the time domain undergoes Fourier transformation into the frequency domain, yielding a mass spectrum. Notably, Orbitrap employs image current, distinguishing it from other methods using traditional detection devices.

The Orbitrap's key advantages include its compact size and exceptional mass resolution (> 150,000) with 1-5 ppm mass accuracy [21].

Table 2.2: Advantages and Limitations of different mass analyzers.

Mass Analyzer	Description	Advantages	Limitations
Time-of-Flight	Non-scanning Pulsed	• High sensitivity and ion transmission • High mass resolution • Excellent mass range • Fast scan speed	• Requires fast data acquisition. • Require pulse extraction voltages
Magnetic Sector	Scanning Continuous	• High mass resolution • High dynamic range • High reproducibility • High sensitivity	• Expensive and bulky • Slow scan speed • High vacuum required. • Difficult to couple with pulsed ionization techniques and LC
Quadrupole	Scanning Mass Filter Continuous	• Compact and simple • Relatively cheap • Good selectivity (SIM)	• Limited mass range • Low mass resolution

		• Moderate vacuum required → well suited for coupling to LC	
Ion Trap	Trap Pulsed	• Small and relatively cheap • High sensitivity • Good mass resolution • Compact	• Limited dynamic range • Limited ion trap volume • Limited mass resolution • Requires pulse introduction to MS
Orbitrap	Trap Pulsed	• Very high mass resolution • Very high mass accuracy • Highly sensitive • Compact	• Expensive • Complex • Limited mass range • Limited dynamic range

2.1.3 The Detector

In mass spectrometry, the detector plays a crucial role in identifying ions. Its operating principle is based on the amplification of the current mass separated ions into a measurable signal. Different types of detectors are used depending on their sensitivity, spatial information retention, dynamics and suitability for mass. Most used detectors are discussed in this section.

- **Faraday Cup**

Faraday cups are among the earliest detectors used in mass spectrometry. Fundamentally, a faraday cup is a piece of metal positioned inside the vacuum chamber of the mass spectrometer, which is integrated to the instrument's electronics. Electric field is employed to push ions into the metal piece. When ions strike the metal, electrons flow through the circuit to meet the ions and neutralize them at the Faraday cup's surface. This current can be measured and amplified by the instrument's electronics. The amount of current is proportional to the number of ions hitting the Faraday cup. The limitation of Faraday cups, compared to newer detectors, is their reduced sensitivity, mainly because the Faraday cup itself does not inherently amplify the signal.

- **Array Detector**

Array detectors are devices used in mass spectrometry systems to simultaneously measure multiple ions or particles. These detectors consist of an array of individual detectors, each capable of

detecting a specific ion or particle [22]. The use of array detectors allows for the simultaneous measurement of multiple ions, improving the efficiency and speed of mass spectrometry analysis. Array detectors offer a powerful tool for the simultaneous measurement of ions in mass spectrometry, enabling efficient and accurate analysis of complex samples.

- **Electron Multiplier Detector**

Electron Multiplier detector works based on the concept of "dynodes". A dynode is simply an electrode in vacuum which emits electrons when an ion or electron of sufficient kinetic energy collides on its surface. These released electrons are then accelerated and multiplied as they pass through a series of dynodes (electron multiplier stages). Each dynode multiplies the number of electrons, leading to an exponential increase in signal strength. This intensified signal is then collected, providing a more robust and measurable output.

- **Microchannel Plate Detector**

MCP detectors operate on the principle of electron cascading. When a charged particle (such as an ion) strikes the surface of the MCP, it releases a primary electron. This primary electron then enters one of the microchannels in the MCP. Inside these microchannels, a high electric field causes the primary electron to collide with the channel walls, generating secondary electrons. These secondary electrons, in turn, trigger more electron emissions as they travel through the microchannels. This process results in a cascade effect, where a single primary electron leads to the emission of several electrons, significantly amplifying the signal.

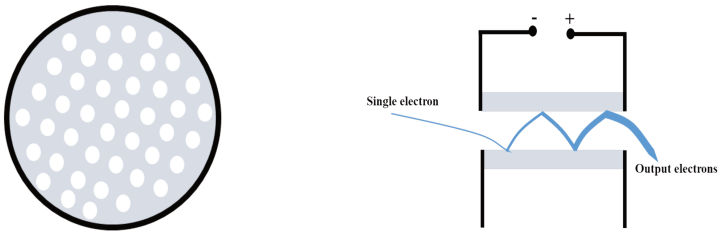

Figure 2.10 (a) Front view of MCP (b) electron avalanche in a single channel

- **Photomultiplier Tube Detector**

A PMT operates based on the principle of photoelectric effect, where incident photons strike a photocathode and release photoelectrons. The released photoelectrons are then accelerated and multiplied through a series of dynode stages within the PMT. Each dynode stage is at a higher potential than the previous one, causing the photoelectrons to undergo a cascade of secondary emission, resulting in an amplified electron current. The amplified electron current is then collected at an anode, producing an electrical signal proportional to the incident light intensity. The PMT assembly includes multiple dynode channels, each with its own set of dynode pathways, allowing for the amplification and collection of photoelectrons from different portions of the incident light. The grid within the PMT assembly helps direct the photoelectrons to the appropriate dynode pathways, ensuring efficient amplification and signal detection.

Table 2.3: Overview of detector types in mass spectrometry: Principles, advantages, and disadvantages

Detector Type	Principle of Operation	Advantages	Disadvantages
Faraday Cup	Use a metal piece to collect ions. Electrons flow to neutralize the ions, inducing a measurable current.	- Simple design –Direct current measurement	- Low sensitivity - No inherent signal amplification
Array Detector	Consists of multiple individual detectors to simultaneously measure multiple ions or particles.	- High throughput - Simultaneous multiple ion measurement	- Can be complex and expensive
Electron Multiplier Detector	Utilizes a series of dynodes where initial electrons are multiplied through successive collisions, amplifying the signal.	- High sensitivity - Good for detecting low abundance ions	- Subject to wear and requires high voltage
Microchannel Plate (MCP) Detector	Operates via electron cascading within microchannels, amplifying the signal as charged particles initiate a cascade of secondary electron emissions.	- High sensitivity and fast response - Capable of spatial resolution	- Limited dynamic range - Performance degradation over time
Photomultiplier Tube (PMT) Detector	Employs the photoelectric effect to release photoelectrons, which are then multiplied through a series of dynodes.	- Extremely sensitive to light - High signal amplification	- Sensitive to magnetic fields - Requires careful shielding from light

2.2 Towards Atmospheric Pressure MS

Historically, mass spectrometers have operated primarily within high-vacuum environments. These instruments excel in their ability to achieve exquisite sensitivity and resolution, making them indispensable tools for quantitative and qualitative analyses. Traditional high-vacuum MS systems, such as quadrupole, ion trap, and time-of-flight (ToF) mass analyzers, have found utility in elucidating the elemental composition, structure, and fragmentation patterns of compounds. These instruments are widely employed in applications ranging from small molecule quantification in environmental studies to the characterization of complex biological molecules in proteomics and metabolomics.

Despite their strengths, traditional high-vacuum mass spectrometers have certain limitations. Foremost among these is the requirement for vacuum-compatible sample introduction and ionization techniques. This necessity has traditionally imposed constraints on the types of samples that can be analyzed, often necessitating extensive sample preparation to remove volatile components or solvents incompatible with vacuum conditions. This limitation is particularly salient when dealing with delicate biological specimens, volatile organic compounds, or samples from complex matrices. High vacuum mass spectrometers typically require small sample sizes. Analyzing large or scarce samples can be challenging, especially when the sample size is limited. Traditional high vacuum mass spectrometers can be complex, and expensive in maintenance, as they have to go through pressure changes during the sample insertion.

Recent years have witnessed a paradigm shift in mass spectrometry with the advent of ambient ionization techniques. These methods allow for the direct analysis of samples under near-ambient conditions, circumventing the need for high-vacuum systems.

Ambient ionization was introduced in the early 2000s, which brough a new revolution in the field of mass spectrometry. As defined by Prof. R. Graham Cooks, ambient ionization refers to “the ionization of unprocessed or minimally modified samples in their native environment, and it refers to the ionization of condensed phase samples in air” [23]. Since its inception, many researchers have contributed to the development of techniques and devices for sampling and ionization at atmospheric conditions, in order to reduce instrument and experimental complexity, and time required for sample preparation.

2.2.1 Ambient Ionization Techniques

Most ambient ionization techniques are either derived from spray-based ionization or laser-based ionization.

Spray-based ambient ionization techniques, such as **Desorption Electrospray Ionization (DESI)** [24], [25], [26]**, Easy Ambient Sonic Spray Ionization (EASSI)** [27], [28]**, Paper Spray Ionization (PSI)** [29], [30]**, Electrospray-assisted Laser Desorption/Ionization (ELDI)**[31], [32], [33]**, and Matrix-assisted Laser Desorption Electrospray Ionization (MALDESI)** [34], [35], [36]**,** employ the innovative approach of generating charged solvent droplets to directly ionize samples in their native environment under atmospheric conditions. These methods streamline the ionization process by atomizing a solvent towards the sample surface, where an electrical potential or sonic energy charges the solvent droplets. Upon contact, these droplets facilitate the solubilization, desorption, and extraction of analytes from the sample surface. The ionization of analytes is achieved through electrospray ionization (ESI)-like mechanisms, where the evaporation of solvent from the droplets increases the charge density until the droplets release the analytes as gas-phase ions. ELDI and MALDESI further expand these capabilities by combining laser desorption with electrospray ionization, enhancing the efficiency and specificity of ion generation. ELDI utilizes a laser to desorb analytes before ionizing them with an electrospray, while MALDESI applies a matrix to assist in the laser desorption process before employing an electrospray for ionization. The generated ions are then analyzed by mass spectrometry.

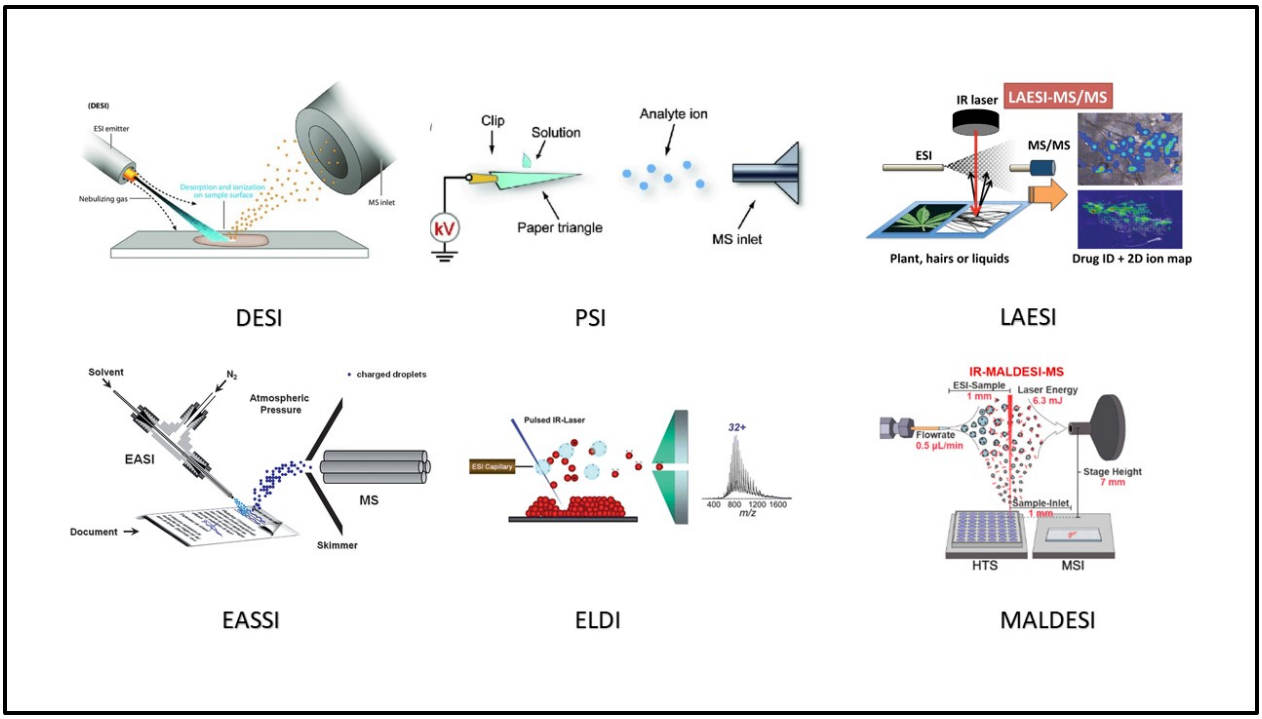

Figure 2.11 Spray assisted ionization techniques, DESI [37]*, PSI* [29]*, LAESI* [38]*, EASSI* [27]*, ELDI* [31]*, MALDESI* [34].

Laser-based ionization techniques, specifically **Laser Desorption/Ionization (LDI)** and **Atmospheric Pressure Matrix-Assisted Laser Desorption/Ionization (AP-MALDI)**, offer sophisticated methods for generating ions from samples under ambient conditions.

LDI [39] focuses a laser beam directly onto the sample, causing molecules to desorb from the surface due to the laser's thermal energy. This method is particularly useful for analyzing solid samples and can achieve high spatial resolution, making it suitable for mass spectrometry imaging (MSI) applications. However, LDI typically requires the sample to be inherently ionizable or coated with a suitable material that aids in the desorption and ionization process, as it does not rely on a matrix to assist in ion generation.

AP-MALDI, [40], [41], [42], [43]on the other hand, is a variant of the traditional MALDI technique that operates at atmospheric pressure, enhancing its compatibility with other atmospheric pressure ionization methods and mass spectrometers. By incorporating a matrix material that absorbs laser energy, AP-MALDI facilitates the desorption and ionization of a

broader range of molecules, including those with low volatility or thermal instability. The matrix serves as a medium that absorbs laser energy, transferring it to the analyte molecules to promote their desorption and ionization without decomposition. This feature makes AP-MALDI particularly advantageous for the analysis of large biomolecules, such as proteins and peptides.
Both LDI and AP-MALDI represent critical advancements in the field of mass spectrometry, expanding its applicability to diverse research areas, from proteomics and metabolomics to material science and forensic analysis. By enabling the direct analysis of complex samples with high sensitivity and specificity, laser-based ionization techniques continue to play a pivotal role in advancing our understanding of molecular composition and dynamics across various scientific disciplines.

The realm of mass spectrometry (MS) has expanded significantly with the development of various innovative ionization techniques beyond traditional methods. Among these, several unique approaches utilize specific physical or chemical principles to ionize samples under ambient conditions or with minimal preparation. Here's an overview of some distinctive techniques that have contributed to broadening the applications of MS:

Picosecond Infrared Laser Desorption (PIRL)
PIRL [44], [45] utilizes a picosecond infrared laser to non-thermally desorb biomolecules from a sample by exciting vibrational modes specific to the molecular bonds within the matrix or sample. This technique is especially beneficial for the analysis of large, non-volatile biomolecules like proteins and peptides, as it minimizes sample decomposition and fragmentation by avoiding excessive heating.

Laser Ablation Dielectric Barrier Discharge (LADBD)
LADBD [46], [47], [48] combines laser ablation with dielectric barrier discharge (DBD) ionization. In this technique, a laser is used to ablate material from the sample surface, which is then ionized by a DBD plasma generated at atmospheric pressure. LADBD is characterized by its ability to ionize a wide range of compounds, including inorganic materials, with high efficiency and minimal fragmentation.

Laser Desorption Corona Beam Ionization (LD-CBI)

LD-CBI integrates laser desorption with corona discharge ionization [49]. A laser desorbs analytes from the sample surface, which are subsequently ionized by a corona beam generated by a high-voltage needle electrode. This method is advantageous for its simplicity and the generation of minimal fragmentation, making it suitable for the analysis of small to medium-sized molecules.

SpiderMass

SpiderMass is a novel technique designed for in vivo and real-time analysis of biological tissues. It employs vibrational excitation of water molecules within the sample to facilitate desorption and ionization of biomolecules directly from living tissues[50], [51], [52].

Laser Ablation Chemical Ionization (LA-CI)

LA-CI [53] uses laser ablation to desorb analytes from the sample, followed by chemical ionization in a reaction chamber containing a reagent gas under atmospheric pressure. The technique benefits from the soft ionization properties of chemical ionization, preserving the molecular structure of analytes and enabling the analysis of a wide variety of compounds, including fragile molecules.

These techniques collectively enhance the versatility and application range of mass spectrometry by offering novel approaches to sample ionization. Each method brings distinct advantages to the table, from minimal sample preparation and preservation of molecular integrity to the capability of in vivo analysis. As the field of mass spectrometry continues to evolve, these and future innovations will undoubtedly open new avenues for research and diagnostics, pushing the boundaries of what can be achieved in molecular analysis.

Table 2.4: Ambient ionization techniques

Category	Technique	Description
Spray-based Ionization	Desorption Electrospray Ionization (DESI)	Generates ions by spraying charged solvent droplets onto a sample surface.
	Paper Spray Ionization (PSI)	Ionizes analytes from a paper substrate wetted with a sample and subjected to a high voltage.
	Laser Ablation Electrospray Ionization (LAESI)	Combines laser ablation of a sample with post-ablation electrospray ionization.
	Easy Ambient Sonic Spray Ionization (EASSI)	Uses sonic nebulization of a solvent to create charged droplets for ionization.
	Electrospray-assisted Laser Desorption/Ionization (ELDI)	Uses laser desorption in conjunction with electrospray ionization for sample analysis.
	Matrix-assisted Laser Desorption Electrospray (MALDESI)	Combines MALDI with electrospray ionization, utilizing a matrix to assist in desorption.
Laser-based Ionization	Laser Desorption/Ionization (LDI)	Directly ionizes/desorbs molecules from a sample using laser energy.
	Atmospheric Pressure MALDI (AP-MALDI)	A variant of MALDI that operates at atmospheric pressure for ionization.
Other Techniques	Picosecond Infrared Laser Desorption (PIRL)	Utilizes vibrational excitation of a matrix with a picosecond infrared laser for desorption.
	Laser Ablation Dielectric Barrier Discharge (LADBD)	Employs laser ablation followed by ionization through dielectric barrier discharge.
	Laser Desorption Corona Beam Ionization (LD-CBI)	Combines laser desorption with ionization via corona discharge.
	SpiderMass	Uses vibrational excitation of water within samples for desorption and ionization.
	Laser Ablation Chemical Ionization (LA-CI)	Integrates laser ablation with chemical ionization for analyte ionization.

These ionization techniques operate at atmospheric pressure, while the mass analyzer and detectors require a vacuum environment. Over time, various researchers have developed specialized sampling interfaces to facilitate the transfer of ions from atmospheric conditions to the vacuum for analysis. These advancements will be discussed in the next section.

2.2.2 Sampling interface for transfer of ions from atmosphere to vacuum

In the development of ion transfer interface, the optimal approach to transfer ions from atmosphere to vacuum would be using conventional ion optics. However, ions at atmospheric pressure are dominated by collisions with the gas molecules, making conventional ion optics ineffective to focus the ions [54]. Therefore, the ions should be transported through a pressure reduction before entering the analyzer, which employed various methods and techniques to transfer the ions.

2.2.2.1 Continuous pinhole sampling

The simplest method to transport ions from the ionization region at atmospheric pressure to the analyzer at vacuum is to employ a small pinhole sampling aperture from ion source to the vacuum chamber [55]. The diameter of pinhole needs to be consistent with the pumping system and the vacuum requirement of the mass spectrometer. To maintain the required vacuum, this method is restricted to a diameter of few μm, which limit the analysis performance due to low sampling of ion current.

2.2.2.2 Continuous differential pressure sampling

To improve the analysis performance and increase sampling, researchers developed the sampling interface based on differential pressure. The concept of "differential pumping" refers to the use of variable pressure stages to facilitate the transition of ions from a higher-pressure region (atmosphere) to a lower-pressure region (vacuum) without significant loss or dispersion.

In this setup, differential pumping stages are strategically placed along the transfer path, each maintaining a pressure suited for efficient ion transmission. This staged approach helps overcome challenges associated with collisions between ions and gas molecules at atmospheric pressure, allowing for a more controlled and effective transfer into the mass spectrometer.

The design typically includes specific components such as skimmers, orifices, and ion optics that contribute to maintaining pressure differentials and directing the ions toward the mass analyzer. The careful arrangement of these elements ensures optimal ion transmission efficiency, crucial for accurate and sensitive mass spectrometric analysis.

In 2013 a patent was filed for the atmospheric pressure ionization inlet for mass spectrometry, in which they developed an interface based on continuous differential pumping [56]. The sampling interface includes capillary, with an opening towards the first pumping stage of pressure (1-10)

torr, and this region is called turbulent region. This sampling interface collects ions in a turbulent region downstream from the capillary exit. Then there is the second opening which is lower pressure than the first region. By facilitating the controlled flow of ions by maintaining the required pressure difference in each stage and electric field, interface enables accurate analyses.

Using the differential pressure concept for transferring of ions an active capillary plasma source was developed to reduce the loss during transfer of ions from atmosphere to vacuum and maximize the ionization of very small amount of substance at atmospheric pressure. This plasma ionization source is based on dielectric barrier discharge (DBD) [57]which is incorporated on a capillary providing both ionization and sampling.

Using the same ionization source, dielectric barrier discharge ionization (DBDI) Haisch, et al. worked on imaging at atmospheric pressure, in which he used laser ablation for solid sample (pain killer and coffee bean). DBDI has been commercialized as soft ionization by chemical reaction in transfer (SICRIT) [46]. They can reach high spatial resolution down to 10 µm for molecular imaging. They used nitrogen as a carrier gas and heating the transfer tube to be more effective.

2.2.2.3 Discontinuous sampling interface

Different schematic and concepts are used to develop sampling interface, to improve the signal and overcome the sampling loss during transfer. One of the interfaces is discontinuous atmospheric pressure interface (DAPI), using pinch valve. The concept of discontinuous interface is to open the ion introduction channel for a short time then close it during the subsequent pump down, mass analysis and ion clearance and reset period of each scan. In this while transferring the ions pinch valve is turned on and all the voltages are turned off, and all pumps are also off. Then after ions are transferred and collected in an ion trap, pinch valve is off and pumps are turned on, after waiting for certain time of required pressure for analysis, voltages are turned on and analysis is started. Worked done in 2008 on discontinuous atmospheric interface [58], they studied the comparison between ion transfer efficiency in the case of continuous transfer where they used differential pumping system with the discontinuous transfer, found 0.1 % and 0.2 % respectively.

In discontinuous atmospheric pressure interface with pinch valve is notably slow process and the transfer efficiency is at a maximum of 0.2%, indicating low efficiency level. Additionally, pumping system's capacity is reduced in comparison to a Mass Spectrometry (MS) system with continuous atmospheric pressure interface (API). In the case of DAPI long capillaries were used,

and due to coulomb repulsive effect (like-ions repel each other due to their positive charges), ions could be lost while travelling through long capillaries [59]. To improve the sampling and maintain low pressure inside the chamber, researchers came up with a new option of using solenoid valves. Solenoid valve is used to fast open the sealing ball which controls the flow of the ions from atmosphere to vacuum. In research published in 2014, they used pinhole and sealing ball to open and close the interface. To maintain the fast opening and closing of pinhole solenoid valve is connected to sealing ball. For the analysis this interface was opened for 27 ms and has to wait for 300 ms to reach the working pressure for rectilinear ion trap (RIT).

Ionization at atmospheric pressure can reduce the efficiency and resolution of mass spectrometric analyses. The complex environment at atmospheric pressure often leads to increased collisions between ions and neutral molecules, causing ion losses and broadening of mass spectral peaks. This results in lower sensitivity and decreased resolution, which can hinder the accurate identification and quantification of analytes. To overcome these challenges, researchers tried to transfer the ablated plume, which includes ions and neutral species, from atmospheric pressure to vacuum conditions where mass analyzers and detectors operate optimally. Sampling interfaces were developed over time to facilitate this transfer, minimizing ion losses, and their advancement is discussed below.

2.2.3 Sampling interface for transfer of ablated plume from atmosphere to vacuum

Sto et al. in the pursuit of moving towards the atmospheric pressure mass spectrometry, developed atmospheric pressure sampling interface in 2001 [60]. This interface facilitated the transfer of laser ablated molecules from atmospheric pressure to vacuum. It comprised a 20-µm-i.d. stainless steel capillary attached to the tapered end of a 20-cm-long, 10-mm-i.d. stainless steel tube, which was directed towards the electron impact ionizer of a QMS. Through precise positioning using a micro-actuator, the capillary inlet was situated extremely close (<5 µm) to the Scanning Near-Field Optical Microscopy (SNOM) (A microscopy technique used for studying nanostructure that breaks the far field resolution limit by utilizing the characteristics of evanescent waves.) tip, and the sample was tilted toward the capillary to enhance sampling efficiency. This interface functioned as a controlled leak, necessitating specific requirements for the vacuum pumps. Experimental

validation of this interface was conducted using an anthracene sample. Employing this system resulted in the appearance of the anthracene signal within approximately 20 milliseconds. Furthermore, the signal persisted for up to 1 second, attributed to multiple adsorption and desorption processes occurring on the interface tube's walls.

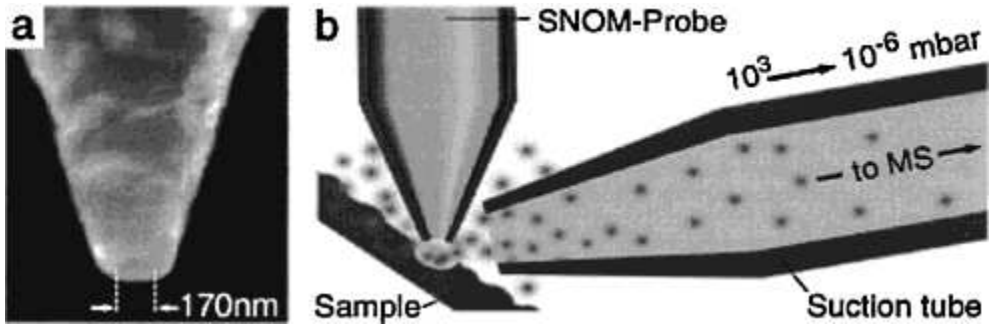

Figure 2.12 Schematic diagram of the near-field laser ablation/nanosampling interface for mass spectrometry taken from article [60].

With the continuation of the improvement of the sampling interface in 2006 [61], Setz et al. developed new sampling interface based on the principle of differential pumping, in which they used two nozzle-skimmers system to create two differentially pumped sections of the interface, as illustrated in Figure 2.13. The pressure in the two sections were 5×10^{-1} and 2×10^{-2} mbar respectively. Argon gas was introduced as a buffer gas to induce collisional cooling, thereby enhancing resolution for liquid samples.

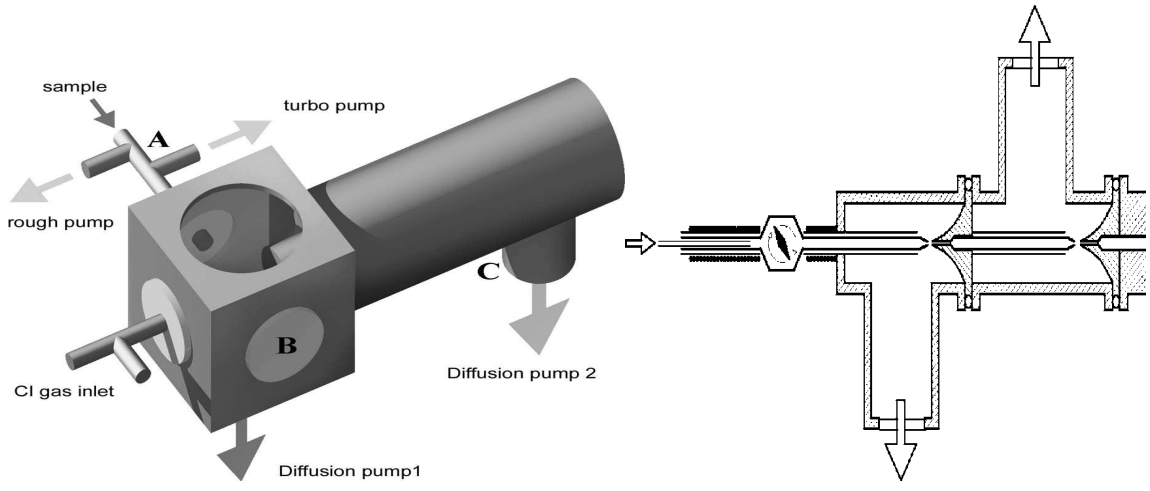

Figure 2.13 Illustration of the experimental setup with dual nozzle-skimmer units [61].

The ionization techniques encompassed Electron Impact and Chemical Ionization, both executed under vacuum conditions. Laser ablation, a critical component of the process, was conducted in an ambient environment, with the capillary inlet positioned in close proximity (< 1 mm) to the laser spot on the sample. In this configuration of transfer of ablated plume from atmosphere to vacuum, sample is placed right in front of the inlet of the capillary having an angle of incidence of 45° with respect to the laser beam and capillary inlet. To sample enough ablated species, the laser was free running.

Building upon this foundation, Schmitz et al. and colleagues introduced modifications to the sampling interface for imaging atmospheric pressure using SNOM limit by utilizing the characteristics of evanescent waves (electromagnetic wave that occurs near the boundary of a medium where total internal reflection of light happens). In modified sampling interface, instead of a two-stage pressure reducing interface [62], a one-stage design with only one nozzle-skimmer pair was used (see Figure 2.14), and typically 0.3-0.4 mbar pressure is achieved in this stage. The analysis involves samples comprising 2,5 Dihydrobenzoic Acid (DHB) and Anthracene and is tilted 15° for better sampling efficiency.

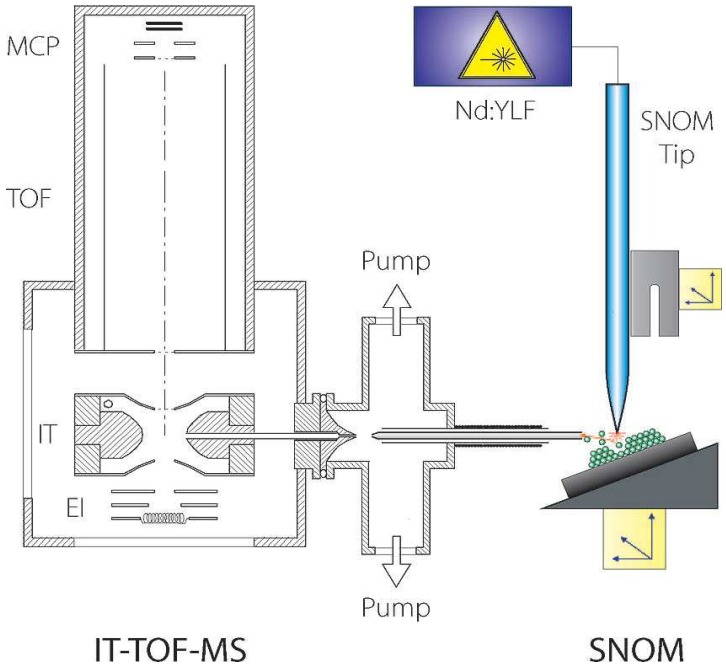

Figure 2.14 Illustration of experimental setup with single nozzle-skimmer unit to transfer ablated plume to ionize using electron impact [62].

In their pursuit of improved efficiency, Zhu et al. conducted a detailed exploration in 2011, refining the sampling interface to investigate sampling efficiency further. Their subsequent publication focused on enhancing the efficiency of sampling neutrals and ions in laser ablation-based nanoscale imaging mass spectrometry (IMS) [63]. They discovered that the sampling efficiencies of neutrals and ions were comparable in this technique. Laser ablation-based mass spectrometry involves collecting ions produced at atmospheric pressure for analysis. These ions must be transferred to a vacuum for analysis, typically done using a sampling capillary. However, focusing ions from atmospheric pressure to a vacuum aperture using only dc fields is challenging due to Gauss's law [64]. Gauss's law dictates that electric field lines diverge as they pass through a simple aperture, making it hard to focus ions onto a small spot in a vacuum. Consequently, only a fraction of ions generated at atmospheric pressure can be efficiently transferred to the vacuum for mass spectrometric analysis. To address this challenge, various ion optics techniques like electrostatic lenses, ion funnels, and differential pumping stages have been developed. These techniques use a combination of electric and magnetic fields to focus ions onto a small spot in a vacuum. However, these methods are intricate and require careful optimization to achieve high ion transmission efficiency.

In contrast, the neutral sampling approach proposed in the paper eliminates the need for ion optics. Instead, it samples neutrals from atmospheric pressure into the vacuum, followed by post ionization and mass spectrometric analysis. For their study on sampling efficiency, they employed a single-stage pressure-reducing interface with only one nozzle-skimmer pair, as depicted in Figure 2.14. To assess sampling efficiency, they placed a glass slide right behind the exit of the sampling capillary on the vacuum side. The material ablated from the sample was deposited on the glass slide, and its quantity was analyzed using Atomic Force Microscopy (AFM). The efficiency of collecting ablated material onto a collection plate positioned on the vacuum side of the sampling capillary was estimated to be approximately 10%. Some of the ablated mass was not sampled into the vacuum but instead got deposited between the ablation site and the capillary inlet.

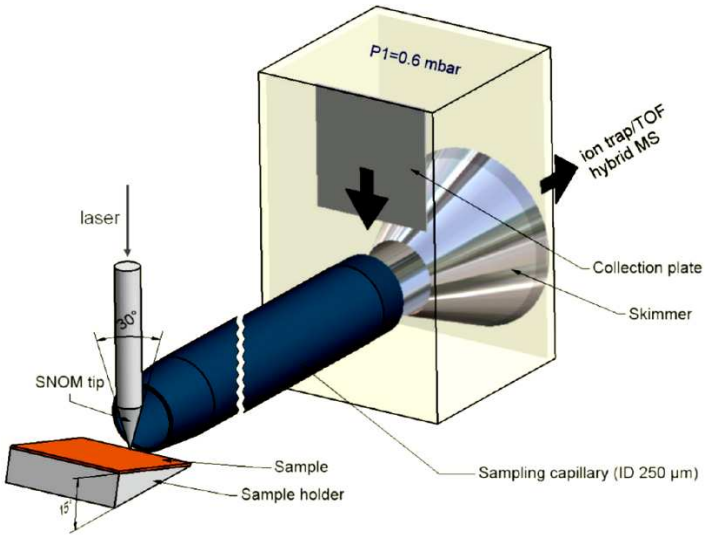

Figure 2.15 Schematic of the setup developed in [63] *for transporting neutral products from atmospheric near-field laser ablation into the vacuum environment of a mass spectrometer.*

Table 2.5: Comparison of articles I the field of sampling interface for ablated plume from ambient pressure to vacuum.

Articles	**Desorption at AP/vacuum**	**Ion source**	**Ionization at AP/vacuum**	**Differential pumping**	**Samples**	**Remarks**
Sto et al. (2001)	AP	Electron Impact	Vacuum	No differential pumping (Capillary is connected to MS for continuous flow)	**Solid** (Anthracene)	Maintaining pressure inside the vacuum chamber is difficult
Setz et al. (2006)	AP	Electron Impact	Vacuum	Two differential pressure regions	**Liquid** (perfluorotributylamine [PFTBA], Styrene, Bromobenzene **Solid** (Anthracene)	Ablation laser free running
Schmitz et al. (2008)	AP	Electron Impact	Vacuum	Single differential pressure region	2,5-Dihydrobenzoic Acid (DHB), and Anthracene	Redeposition of ablated material is not studied
Zhu et al. (2011)	AP	Electron Impact	Vacuum	Single differential pressure region	Anthracene	Ablated sampling efficiency 10%

Chapter 3 Materials and Methods

This chapter provides the fundamental principles, and a technical description of the instruments used in this thesis. It encompasses 3 analytical methods, including two step laser mass spectrometry (L2MS), Raman spectroscopy and FTIR. For L2MS, two instruments with different mass resolutions were used: a standard resolution spectrometer ($m/\Delta m$ ~1000) and a higher resolution ($m/\Delta m > 10^4$) spectrometer. The atmospheric interface developed in Chapter 4 is coupled to the former instrument. All three techniques, including the two L2MS configurations were used to analyze plastic samples in Chapter 5.

3.1 Two Step Laser Mass Spectrometry (L2MS)

The Two Step Laser Mass Spectrometry (L2MS) technique is based on the coupling of laser desorption, laser ionization, and Time of Flight (ToF) mass spectrometry. This laser-based technique has been extensively used by ANATRAC group, for the analysis of chemical composition of combustion by-products. The main advantages of L2MS are its high sensitivity (around femtomole/laser shot [65]) and selectivity.

In this work, two different L2MS instruments were employed, first one ("Standard Resolution" L2MS – SR-L2MS, developed in the laboratory see section 3.1.2.) will be adapted to analysis at ambient pressure and tested on carboneous species (Polycyclic aromatic Hydrocarbons – PAHs) extensively studied in the group (see Chap. 4). It is limited to a mass resolution of $m/\Delta m$ ~ 1000. The second one (HR-L2MS, Fasmatech S&T) overcomes this limitation: It can achieve a mass resolution of around 20,000, while offering similar performances in terms of sensitivity and selectivity. This device will provide a point of comparison with the SR-L2MS and the atmospheric-pressure interface developed in the thesis when analyzing plastic samples (see Chap. 5) and a reference for a future implementation of the interface.

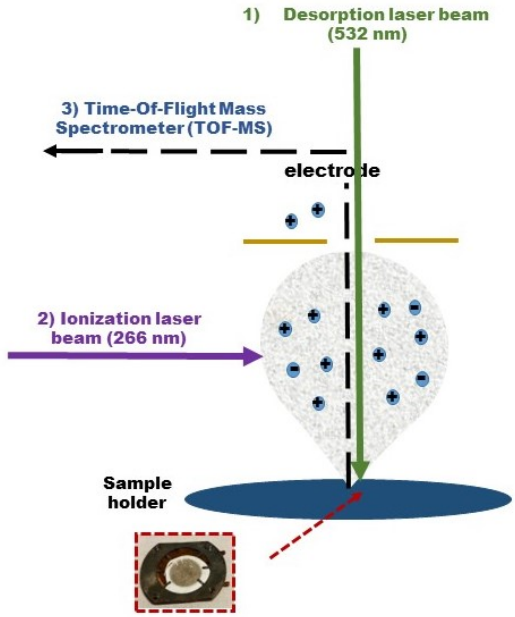

Figure 3.1 Depicts the sequential phases of the L2MS process: (i) Laser Desorption, where the sample's surface material is desorbed using a laser; (ii) Laser Ionization, involving the ionization of the desorbed material through another laser pulse; and (iii) Time-of-Flight Mass Spectrometry (ToF-MS), where the ions are sorted and analyzed based on their mass-to-charge ratio.

3.1.1 Principles

3.1.1.1 Laser Desorption

Interaction of laser light with a solid target can lead to four different phenomena depending on the peak irradiance at the sample surface. These conditions are commonly known as desorption, phase explosion, hydrodynamics sputtering and photomechanical spallation [66], [67]. Laser desorption is a unique, low-energy process that results in molecular ejection without causing damage to the sample surface. At very low irradiance only neutrals are generated in gas phase. In contrast, phase explosion, hydrodynamic sputtering, and photomechanical spallation, collectively referred to as laser ablation, are more intense processes that impact the bulk properties of the sample, often leading to partial or complete destruction of its surface. A significant fraction of ablated species are ions. Ablation phenomena play a crucial role in specific analytical techniques, with the phase

explosion serving as the foundation for techniques like MALDI (Matrix Assisted Laser Desorption Ionization).

A qualitative study done by Richard F. Haglund [68] described laser beam interaction with nonmetallic solids. This description assumes that the laser interaction can be decomposed into four phases.

I. The absorption of laser energy by single-photon or multi-photon processes (absorption properties of the solid sample at the laser wavelength and energy per photon are important).
II. Transformation of the incident energy through radiative and nonradiative relaxation processes (propagation of shock wave or heating, etc.).
III. Ejection of particles, molecules or atoms, as neutrals or ions, from the irradiated surface and its surroundings.
IV. Formation and expansion of dense plumes of neutral and ionized gas.

As explained earlier at low irradiance regime, direct ionization of ejected molecules can be avoided and only neutrals molecules are ejected. At this low irradiance regime, the ejection of matter from a surface can be described by molecular desorption processes, where the number of molecules N ejected from the sample surface can be predicted by Arrhenius type expression [69].

$$\mathrm{N} = \mathrm{A}\exp\left(-\frac{\mathrm{E}_s^*}{\mathrm{k_B}(\mathrm{T_0} + \mathrm{BI_{des}})}\right) \tag{3.1}$$

Where A is the pre-exponential factor, E_s^* is the activation energy, $\mathrm{k_B}$ the Boltzmann's constant, $\mathrm{T_0}$ the initial temperature of the surface, $\mathrm{I_{des}}$ the desorption irradiance and B thermal conversion efficiency. This model is only effective when $\mathrm{I_{des}}$ is below the threshold value. Above threshold the ejection mechanism shows the qualitative change, the thermal model is no longer valid, and a different description must be used.

Ablation and desorption is affected by laser wavelength [70], [71], [72]. In general, higher wavelength lowers the ablation rate. In detail shorter wavelength offer higher photon energies for bond breaking and ionization of sample [73]. At laser wavelengths of 532, 266, 213, and 157 nm, the corresponding photon energies are 2.33, 4.66, 5.83, and 7.90 eV, respectively. Absorption of laser energy by targeted sample varies with the laser wavelength and the absorption property of

the sample. Ablation processes can involve both thermal and non-thermal mechanisms, the choice of which depends on the wavelength of the laser. In a thermal process, electrons absorb laser light, transferring the energy to the atomic lattice, resulting in melting and vaporization of the target material. This thermal mechanism can induce significant fractionation due to differences in the latent heat of vaporization for various chemical elements. Alternatively, if the photon energy surpasses the bonding energy between neighboring atoms (typically a few eV), the laser radiation can directly break the atomic lattice, causing ion and atom ejection without traditional heating effects [74], [75].

Another critical factor influenced by laser wavelength is plasma shielding [76], [77]. The laser beam interacts with the expanding plasma plume generated during the early stages of the ablation process, depending on the pulse duration. Laser energy can be strongly absorbed or reflected by plasma, and the absorption coefficient of the plasma varies with the laser wavelength [77]. Typically, plasma absorption is higher at longer wavelengths. Short UV wavelengths, characterized by high photon energy, penetrate the plasma more efficiently, directly initiating bond breaking in the sample. These conditions contribute to a higher ablation rate and less fractionation.

3.1.1.2 Laser ionization

Ionization energy of a molecule is the minimum energy required to remove an electron from the molecule's outermost orbital. Once the electron is removed, the molecule becomes an ion with a positive charge. Various methods can be employed for ionization of desorbed species, each with their unique impact on the resulting mass spectrum.

Opting for hard ionization method which has high probability of fragmentation (breaking of parent molecule) can considerably reduce the amount of information that can be interpreted from a complex mass spectrum. On the other hand, photoionization, a type of soft ionization technique is a good alternative [78], since the photon energy can be tuned to match the ionization energy of the molecule belonging to a certain chemical class, fragmentation can be minimized or even avoided. Ionization is one of the most critical steps in the analytical process dedicated to the analysis of Polycyclic aromatic Hydrocarbons (PAHs). To make it easier to understand the energy required in the ionization of PAHs, Figure 3.2 shows ionization energy of some PAHs. The ionization energy is plotted as a function of the number of carbon atoms in the molecule[79]. In this it can be seen

as the carbon number increases and the aromatic structure becomes larger, the ionization energy begins to decrease.

Figure 3.2 shows that the ionization energy decreases from 8.1 eV to 7.1 eV in the case of small aromatic molecules (mass range 128-276 u). Most of the molecules (with masses in the range of 128-300 u) have ionization energy in the range of 6 eV to 9eV. Within this range, it is challenging to achieve single-photon ionization experimentally due to the requirement of a laser wavelength in the vacuum ultraviolet (VUV) region (<180 nm). However, with the availability of powerful laser, Multi Photon Ionization (MPI) can be performed.

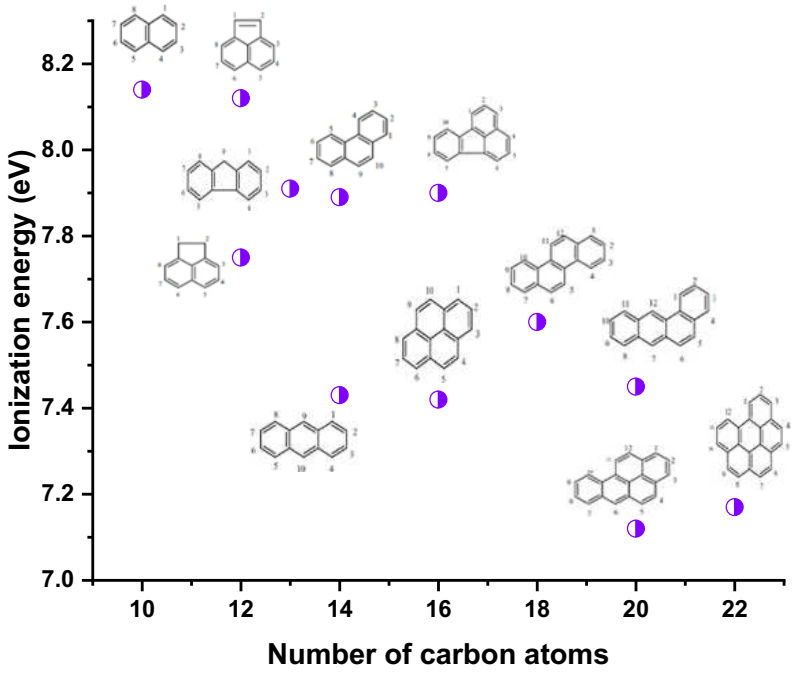

Figure 3.2 Ionization energy of some PAH as a function the number of carbon atoms contained in the molecule. Data is taken from the NIST database[79].

MPI uses multiple photons to ionize a molecule. Unlike Single-Photon Ionization (SPI), which uses a single photon with sufficient energy to directly remove an electron from the molecule's ground state. The probability of ionizing a molecule using multiple photons decreases quickly as the number of photons increases. The first photons excite the molecules from its ground state to excited state, which can be either virtual or real (Virtual states are fleeting, short-lived energy levels that exist only for a fraction of an oscillation of the electromagnetic field of the photon. Real

states, on the other hand, are stable energy levels that can exist for a much longer duration). Additional photons are absorbed until the molecule reaches the ionization potential.

REMPI is a specialized form of MPI that exploits the resonance phenomenon to enhance the ionization efficiency. Resonance occurs when a photon's energy matches the energy difference between two energy levels of the molecule. In REMPI, the first photon excites the molecule to a real intermediate state that exhibits a strong resonance with the incoming photons. This resonance increases the probability of absorbing subsequent photons, leading to a more efficient ionization process. When coupled with mass spectrometry, REMPI allows for selective analysis of resonant species with very high sensitivity. Figure 3.3 shows the ionization energy for different photoionization phenomena.

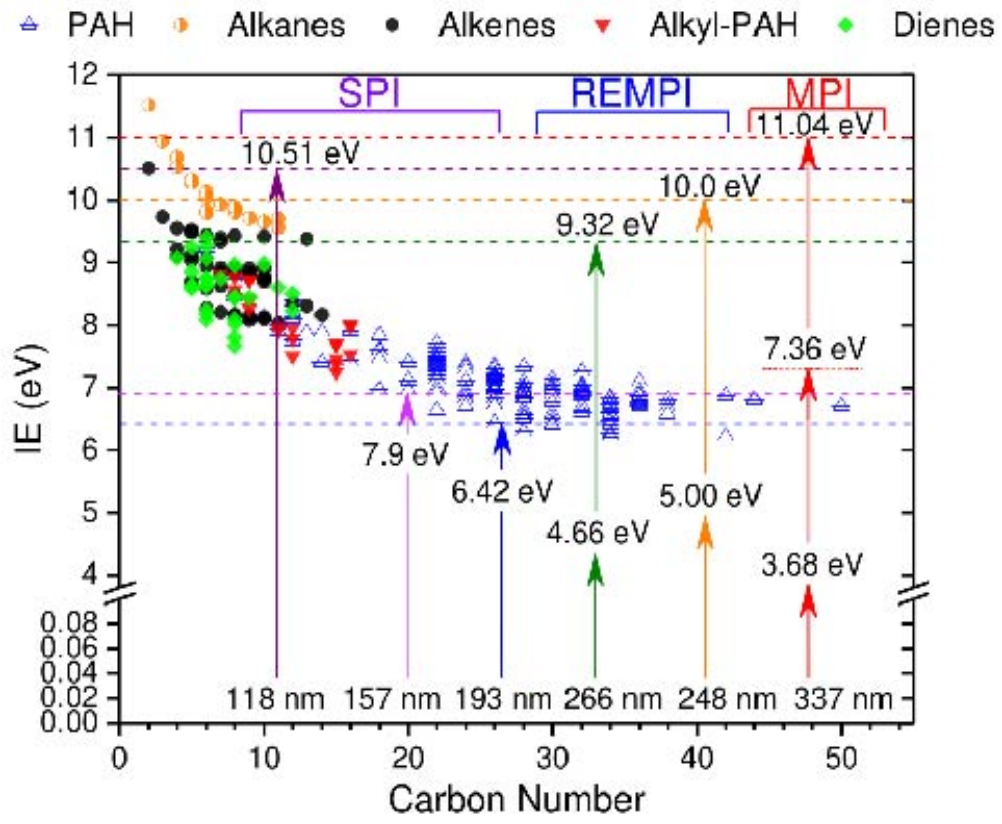

Figure 3.3 Photoionization mechanism, showing the ionization energies for ifferent classes of molecules as a function of their carbon number taken from Desgroux et al..[80]*. At laser wavelengths of 266, 213, and 157 nm, the corresponding photon energies are 4.66, 5.83, and 7.90 eV, respectively.*

Most PAH (polycyclic aromatic hydrocarbon) molecules absorb strongly in the UV spectrum around 266 nm, allowing them to be ionized using Resonance Two-Photon Ionization (R2PI) with the 4th harmonic of a Nd:YAG laser (266 nm).

3.1.1.3 Time of Flight (ToF) Mass Spectrometry

ToF is a mass analyzer that measures the time required for ions to travel a known distance through an electric field to determine their mass to charge ratio. In this section the basic principles and equations employed in ToF are discussed.

The most basic ToF [81] mass analyzer consists of an acceleration region x_A, and field free drift region D (shown in Figure 3.4). Inside ToF tube, ions are accelerated towards the detector through a field free drift region. Ions are separated in this region on the basis of their mass, basically it depends on the time (time-of-flight) taken by ions to reach the detector which depends on the mass of different ions [81], [82], [83], [84].

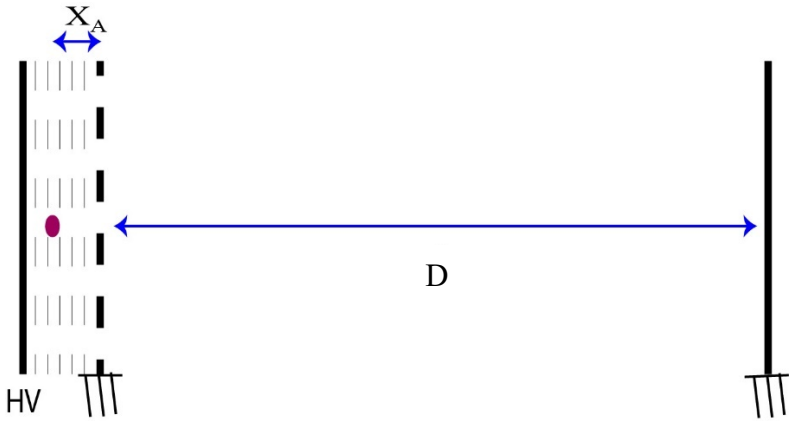

Figure 3.4 Schematic of the basic ToF-mass analyzer with single stage ion source.

As seen in Chapter 2, the quadratic relationship between the time of flight of ions and their mass is governed by Equation *2.2*:

However, in reality there is small time delay (t_0) between the trigger signal and the ionization of the species, Equation *2.2* can be modified as

$$\frac{m}{z} = A(t - t_0)^2 \tag{3.2}$$

Equation *2.2* expresses the time of flight in drift free region, which considers that the ions with identical mass and charge are accelerated at the same point in space with no initial kinetic energy and it is not true in reality. Identical ions may experience different acceleration times (some may accelerate before the other). As a result of these two factors, the identical ions may not reach the detector at the same time, which leads to the broadening of the peaks. To address these effects, two-stage acceleration is used to create a region in the field free drift zone where higher energy ions can overtake lower energy ions, known as "Space Focus" (SF) [83]. Ideally, SF should occur at the detector's surface. The schematic of two-stage acceleration is shown in Figure 3.5. By adjusting the geometrical parameters, namely the lengths x_{A1}, x_{A2}, and the electric fields $\overrightarrow{E_{A1}}$ and $\overrightarrow{E_{A2}}$ in the first and second acceleration region, respectively) it is possible to attain $x_{SF} = D$.
For a single stage time of flight analyzer, the space focus should fulfill a condition where space focus x_{SF} =2x_A, which is called first order space focus, and mentioned earlier ideally SF should occur at the detector surface. Taking into account these conditions, the tube length should be equal to 2x_A (D=2x_A), Equation *2.2* can be written as

$$t = 2x_A\sqrt{\frac{m}{2ezU}} \tag{3.3}$$

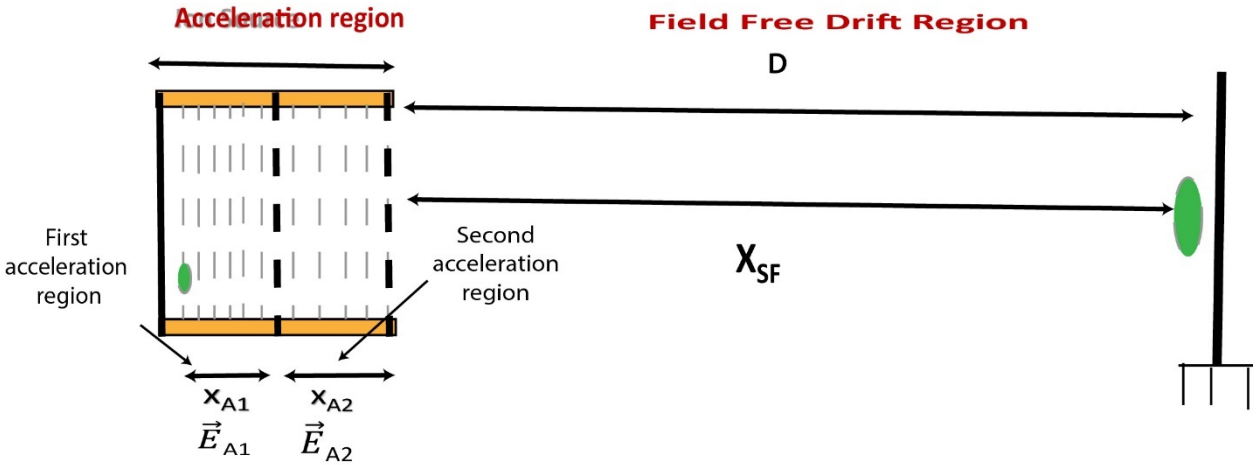

Figure 3.5 Two stage ion source with space focus.

In case of two stage ion source, which consists of two acceleration distances x_{A1} and x_{A2} and two potentials, U_{A1} and U_{A2} (the latter being applied to the intermediate electrode). So, the total time in this case

$$t = t_{A1} + t_{A2} + t_D \tag{3.4}$$

And potential, $U = U_{A1} + U_{A2}$. From equation 3.3, flight time in first acceleration region x_{A1} can be calculated as

$$t_{A1} = 2x_{A1}\sqrt{\frac{m}{2ezU_{A1}}} \tag{3.5}$$

The flight time in the second acceleration region x_{A2} can be described by a flying start situation: ions enter this region with a kinetic energy $\mathrm{qU} - \mathrm{q}U_{A1} = \mathrm{qU_{A2}}$. This flight time is given in the equation below, and for the derivation and more details refer to [83], [85]

$$t_{A2} = \left(\sqrt{U} - \sqrt{U_{A1}}\right)\frac{2x_{A2}}{U_{A2}}\sqrt{\frac{m}{2ze}} \tag{3.6}$$

And drift free flight time is given by,

$$t_D = D\sqrt{\frac{m}{2zeU}} \tag{3.7}$$

These equations (3.5 - 3.7), in the case of two stage ion sources have new features in addition to single stage ones. In this case, despite of fixed geometry, space focus can be adjusted by changing the voltage U_{A1} and U_{A2}.

A ToF-MS equipped with two-stage reflectron can be considered as a combination of two time-of-flight units. Figure 3.6 shows a schematic of the reflectron time-of-flight mass spectrometer. The ion source and the field-free drift region up to SF can be treated as one ToF unit. The ion reflector can be considered as the second ion source with L′ as its field-free drift region. Now the field-free drift region L along with the penetration region within the ion reflector (till the point of no return for the ion) can be considered as the mirror image of the second ToF unit.

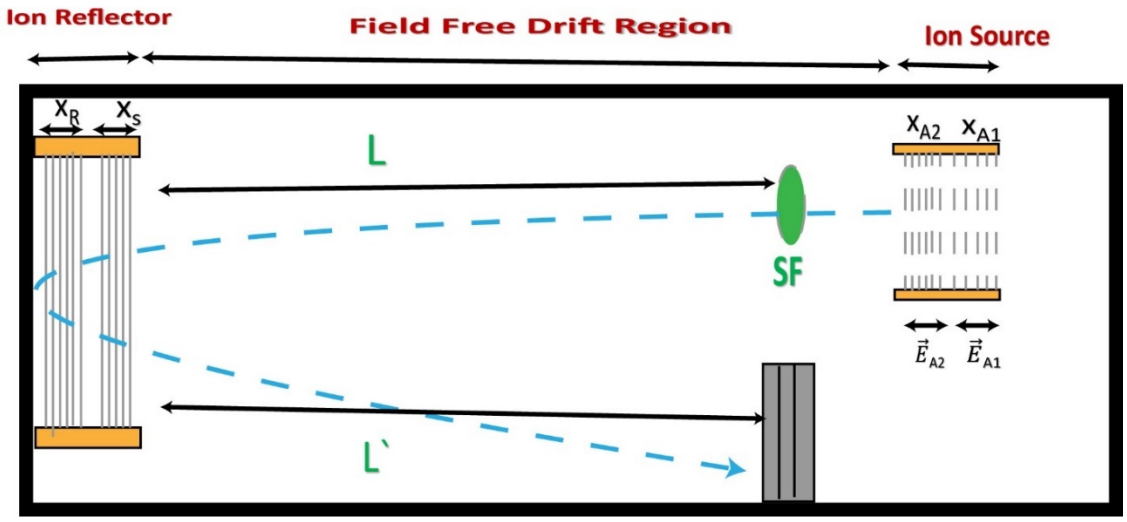

Figure 3.6 Schematic of reflectron ToF-MS, showing ion source, field free drift region and ion reflector.

Thus, combining all the time of flight in case of two stage ion source and after modification for reflectron ToF. In any case, the time-of-flight t and *m/z* can now be expressed as

$$\frac{m}{z} = At^2 + Bt + C \tag{3.8}$$

where A, B and C are constants that depend on geometrical parameters and voltages of the instrument.

3.1.2 Standard Resolution Two Step Laser Mass Spectrometry (SR-L2MS)

In our SR-L2MS instrument, the sample is classically placed on a temperature-controlled holder in the primary (sample introduction) chamber. This primary chamber is connected to the main analysis chamber (residual pressure 10^{-9} mbar) through a gate valve. A liquid nitrogen circulation loop is connected to the sample holder to cool down the sample and prevent the volatile species from sublimating in the vacuum chamber. After the temperature of the sample goes down and the pressure in the primary chamber reaches 10^{-7} mbar, the separation gate valve between primary chamber and analysis chamber is opened and sample is transferred into the analysis zone. Then analysis of the sample is started with starting the desorption step. However, in the work of this thesis, this step of desorption and transferring sample into vacuum is avoided, by developing sampling interface where desorption can be performed at atmospheric pressure instead of vacuum.

In this setup, the solid sample is positioned at atmospheric pressure. A desorption laser is employed to remove material from the sample's surface. The second harmonic (532 nm) or fourth harmonic (266 nm) outputs of a Nd:YAG laser (Continuum Minilite II laser, having a pulse duration of 4 ns and a repetition rate of 10 Hz) were employed for the desorption process. A lens with a 25 cm focal length was used to focus the laser beam. The resulting desorbed analytes are transferred into a spherical vacuum chamber.

Within this chamber, an ionization laser the 4th harmonic of a Nd:YAG laser (266 nm, 4 ns pulse duration, Continuum Powerlite), is used to ionize the analytes. Figure 3.7 illustrates the beam path showing the distance between each mirror, and Figure 3.8 is a picture of the ionization laser and its optical path. To transfer the laser beam from laser source to the ionization region in the vacuum chamber six mirrors and two pinholes were employed. The spot size at the ionization region is 7 mm by 3 mm, and area is 16.5 mm^2, here beam shape was considered elliptical profile as cylindrical lens was used to focus the laser beam and to enhance the molecular beam laser beam overlap. Cylindrical lens transforms the laser beam into a light sheet at its focus, as illustrated in Figure 3.9. This configuration proves advantageous for ionizing gas phase neutrals across a plane rather than at a singular point. Such configuration can enhance the molecular beam and laser beam overlap in the extraction region

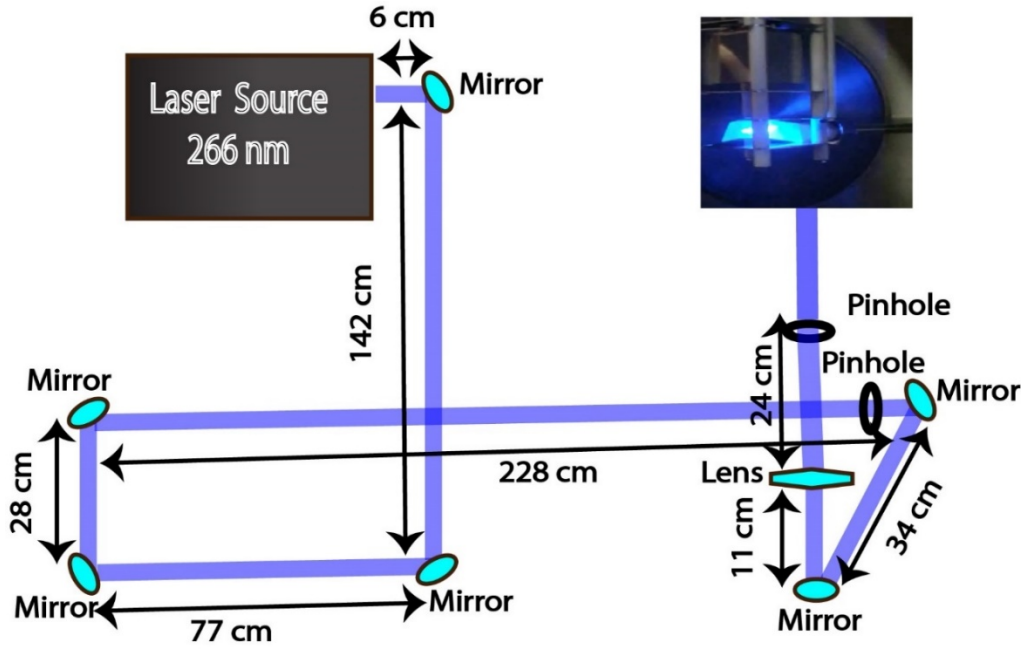

Figure 3.7 Schematic of ionization laser (266 nm) beam path.

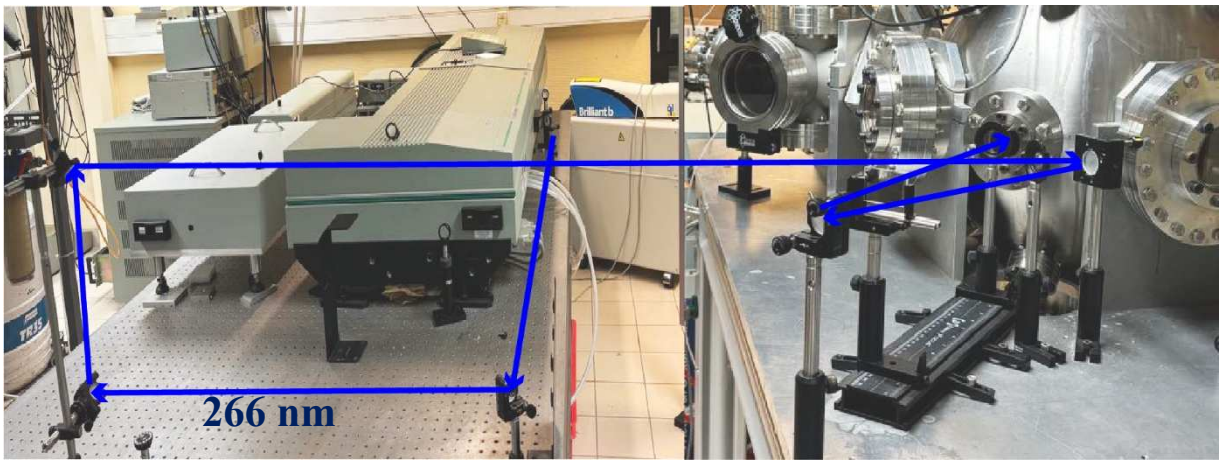

Figure 3.8 Picture of the Nd:YAG laser showing beam path.

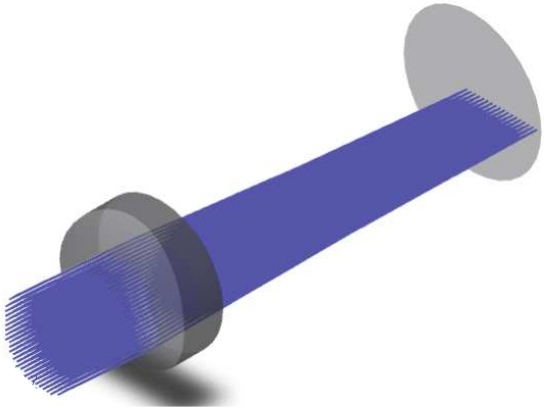

Figure 3.9 Cylindrical lens generates a light sheet at its focus.

The transferred ions are then analyzed via time-of-flight (ToF). In this instrument reflectron Time-of-Flight Mass Spectrometer (Jordan ToF Products, as depicted in Figure 3.10) is used. In this system, the mass-to-charge ratio (*m/z*) of ions is determined based on time measurements. The ions experience acceleration through a static electric field established between two plates defining the ionization region: the repelling plate (V_{A1} = 3125 V) and the extraction grid (V_{A2} = 2496 V). Accelerated towards the extraction grid, the ions traverse V_{A3} (at ground potential), pass through deflection plates (V_{XY} = 396 V), and enter the free-flight (drift) region devoid of an applied electric field.

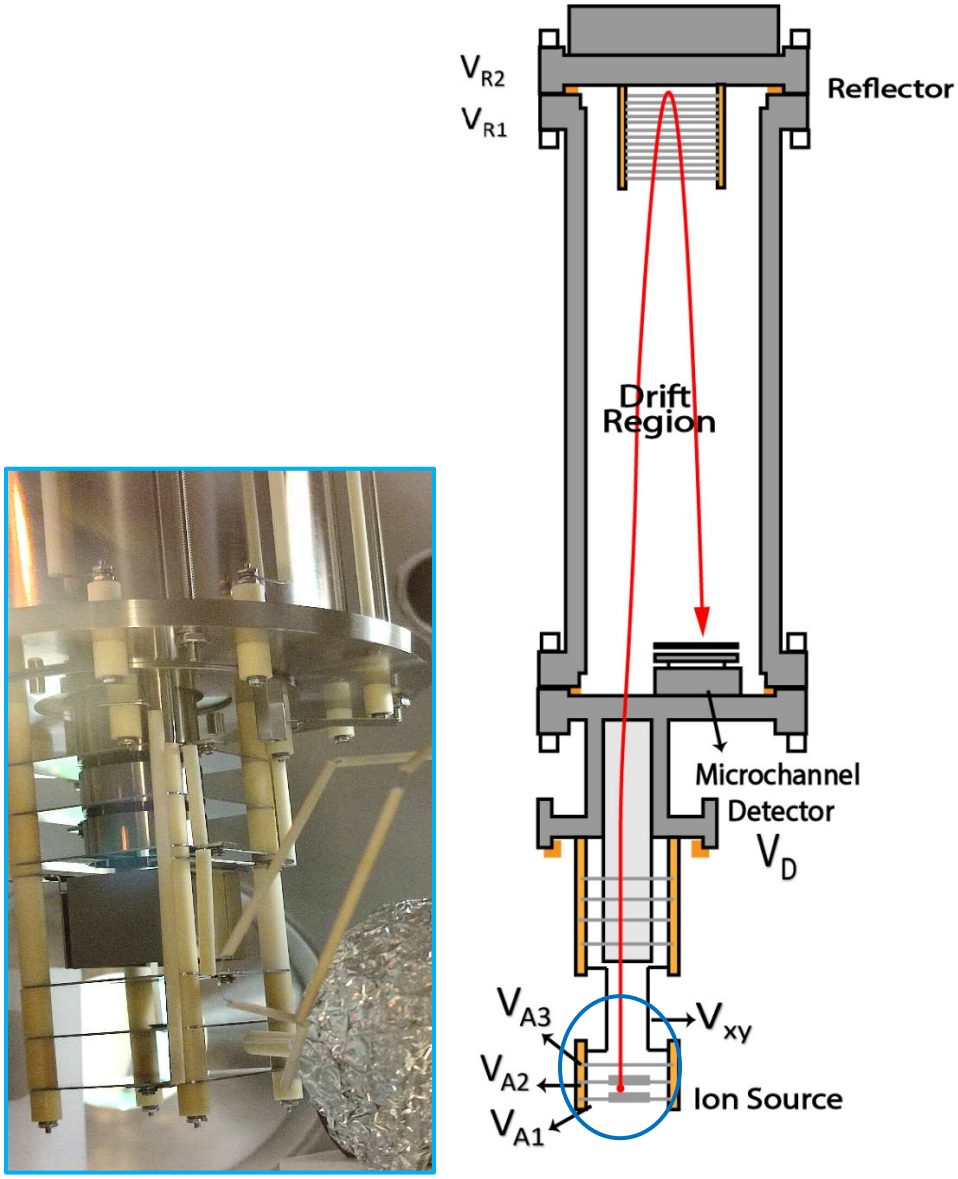

Figure 3.10 Ion path in the Jordan ToF-MS, with a picture of Ion source on left in blue square.

To correct the kinetic energy distribution in the direction of ion flight, a two-stage reflectron (V_{R1} = 1771 V, V_{R2} = 2998 V) is utilized. The reflectron alters the trajectory of ions by initially decelerating and subsequently re-accelerating them towards the detector. This process effectively compresses ion packets of the same mass-to-charge ratio (*m/z*), enhancing mass resolution. Additionally, the reflectron-equipped ToF-MS provides an increased flight distance, approximately double the length of the ToF-MS flight tube, further improving mass resolution.

The velocity of ions depends on their *m/z* ratio, as they receive the same energy from the accelerating electric field. Heavier ions, having a lower final speed, require more time to reach the

detector placed at a known distance. The measured time becomes a proxy for the ion's mass-to-charge ratio. Upon reaching the detector, positioned at the spatial focal plane concerning the extraction from the ion source, ions collide with the MCP assembly (two microchannel plates, chevron mounted, V_D = -2965 V), generating electrons (approximately 10^6 electrons per impacting ion) and producing a measurable current on the anode. This current is then recorded using a digital oscilloscope (LeCroy Waverunner 6200A). Thorlabs DET210 ready to use high speed photo detector was used to trigger the signal from ionization laser for acquisition in the oscilloscope [86]. This signal is then transferred to the computer using LabVIEW software.
The development of sampling interface and the functioning of the setup of atmospheric pressure L2MS will be explained in chapter 4.

3.1.3 High resolution Mass Spectrometer (HR-MS)

This commercial device, designed in close collaboration with Fastmatech company, overcomes the limitations of our in-house device in terms of mass resolution. It has also been designed as a chemical imaging tool at micron scale. Indeed, the instrument is equipped with mechanical systems for precise, accurate and fast maneuvering of the samples during experiment. The sample can be moved in x, y, and z directions using translational stages (ECS3030 and ECS3050, Attocube Systems AG) driven by high-precision piezoelectric displacements. The translation stages velocity is fast enough to change position between each laser shot and it positions itself with high accuracy. Desorption is achieved with the second harmonic of a Quantel Brilliant EaZy Nd:YAG laser (532 nm wavelength, 4 ns pulse duration, and a 10 Hz repetition rate) focused on the sample surface at normal incidence. The desorbed neutral products is then ionized using a second laser beam, specifically the 4th harmonic of a Quantel Q-smart (850 mJ) Nd:YAG laser, with a 266 nm wavelength, 4-5 ns pulse duration, and a 10 Hz repetition rate, positioned perpendicular to the plume. It should be noted that, with minor modifications of the parameters (fluence, beam geometry), the device is also well adapted to the laser desorption/ionization technique (LDI) using the 266 nm laser or the 532 nm laser.

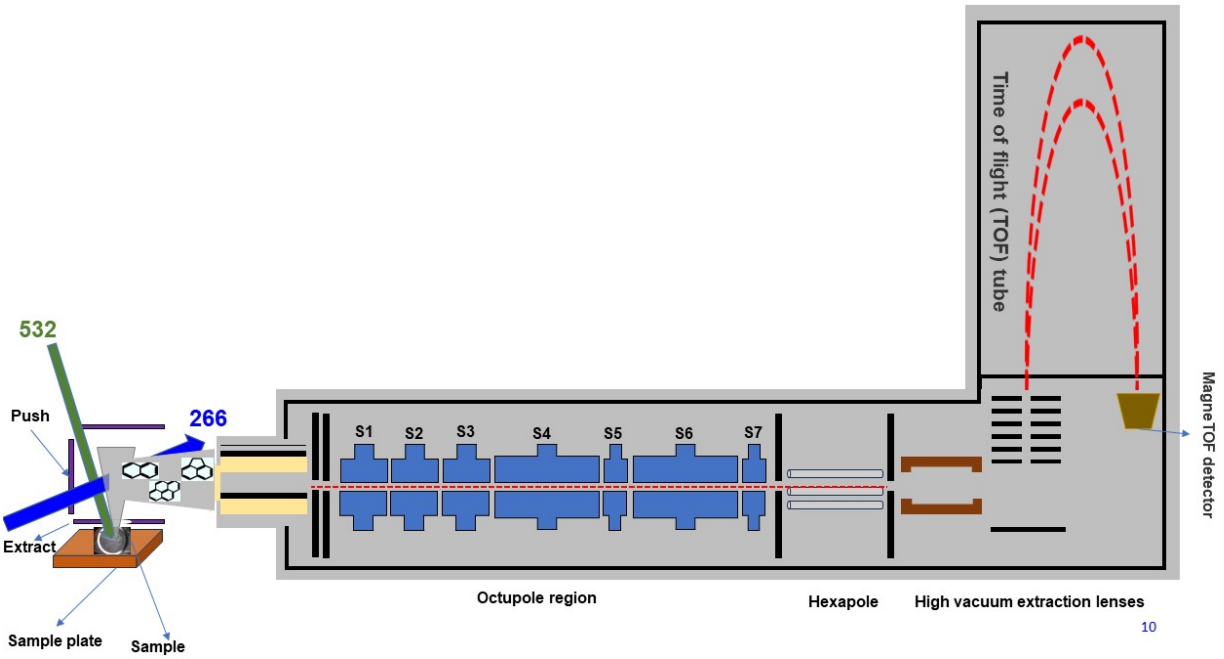

Figure 3.11 HR-MS instrument.

Once the ions are formed, they are guided into the segmented multipole, by set of electrodes (Figure 3.12). The voltage settings for each electrode were optimized for ion transmission efficiency based on ion simulation results (see Table 3.1), specifically for positive ion mode. For negative ion mode, the voltages applied to the electrodes are reversed. Within the side-injection ion source configuration, the produced ions are extracted orthogonally (indicated by the orange dashed line in Figure 3.12 (b)) and directed into the multipole ion trap through the voltages applied to the sample plate, back plate, and electrode 1.

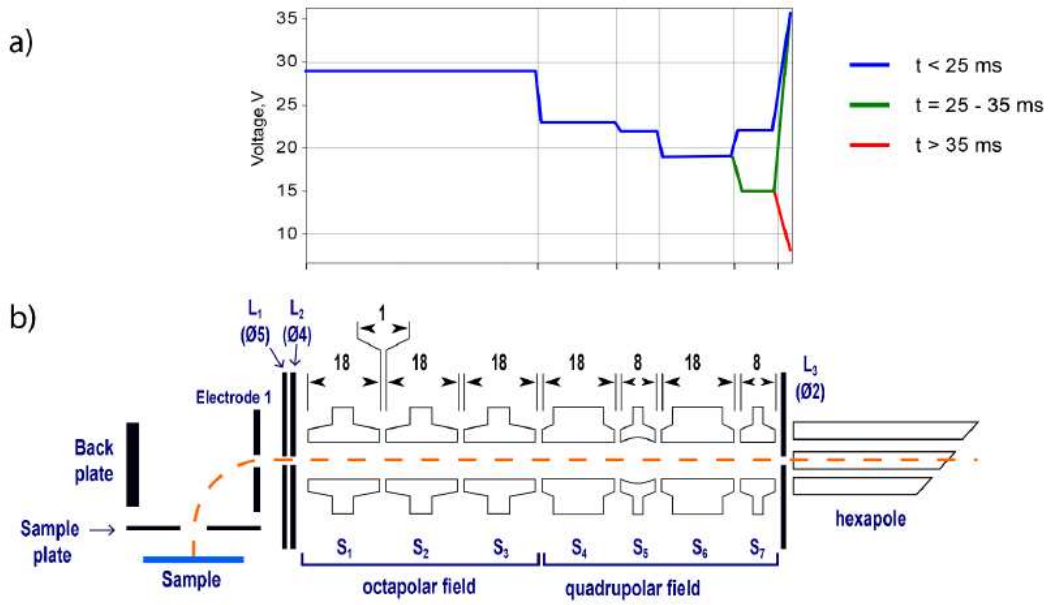

Figure 3.12 Schematic of diagram of the side-injection ion source: DC voltages applied to the ion guide/trap segments (a) sample plate, back plate, electrodes 1 (up and down), lenses L1 and L2, the multipole ion guide/trap, lens L3, and the RF hexapole ion guide, (b) measurements are provided in millimeter, adapted from D. Duca's PhD thesis, 2020.

Table 3.1: The DC voltages applied on various electrodes and multipole segments in positive polarity.

Ion Source		**Octupole**		**Time of Flight**	
Electrode	**Voltage, V**	**Electrode**	**Voltage, V**	**Electrode**	**Voltage, V**
Guide DC	+40	S_{1-3}	+29	Acceleration Low	-1876
Push	+120	S_4	+23	Flight tube	-8320
Lens	+30	S_5	+22	Reflectron Mid	-4810
Pull 2	+29	S_6	+19	Reflectron Back	+728
Sample	+80	S_7	+22, +15	Detector	+2000
Pull 1	-35	Oct Lens L_3	+35, +8		
Extract	+80				

The multipole ion guide/trap consists of a differentially pumped vacuum chamber enclosed and segmented into seven independent parts. Each segment houses a pair of insulating PEEK (polyether ether ketone) rings with radial slots that accommodate eight PCB (printed circuit board) electrodes, which are closely fitted together (as shown in Figure 3.13). These segments are tightly assembled using a PEEK flange at the entry point and a stainless-steel ring at the exit. The flange also serves to accurately place the lens electrodes at the ion guide/trap's entrance. To contain the gas released by a pulsed valve within the trap, PEEK rods are placed between the flanges. Vacuum pumping is facilitated through a space between the lower PCBs, and electrical supply for RF and DC voltages to the segments is connected at the top interface. The ion guide/trap operates on rectangular RF waveforms at 1.8 MHz, with a voltage of 170 V, optimizing ion transmission for *m/z* ratios greater than 40. Adjusting the RF waveform's frequency and voltage can enhance the transmission of ions with *m/z* ratios below 40.

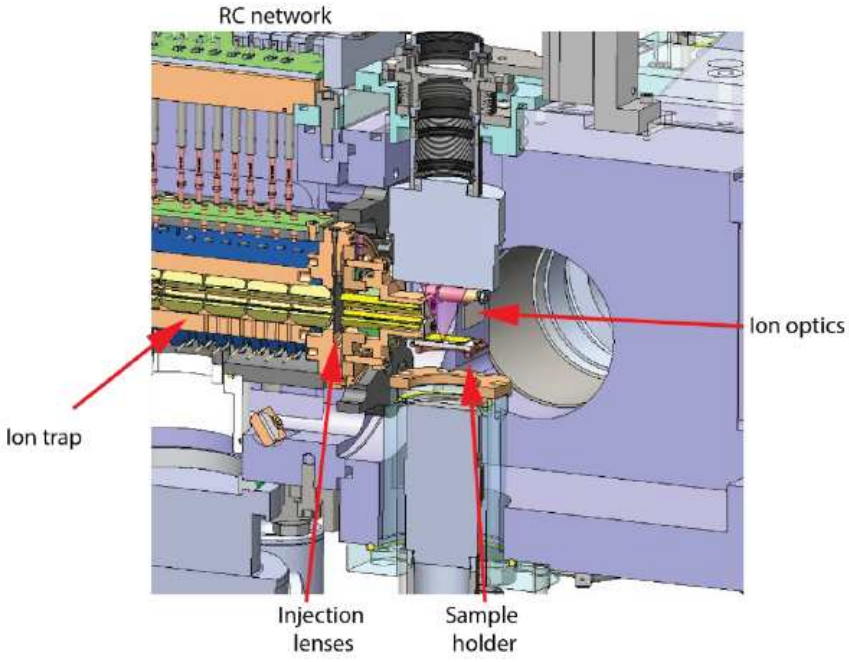

Figure 3.13 3D model of the multipole ion guide/trap (from FASMATECH)

Ions are pulled from the ionization zone and funneled into the ion guide/trap via L1 and L2 lenses. In the initial three segments (S1-S3), ions are kept in place radially by an RF octupolar field. To prevent collision-induced dissociation (CID) and subsequent fragmentation, it's crucial to reduce

the ions' axial energy before they enter the ion trap, where they interact with inert gas molecules, specifically Helium (He), in segment S6, facilitating ion thermalization.

Transitioning from the octupolar to the quadrupolar RF field from segment S4 to S7, this hybrid setup ensures efficient ion transmission across a broad mass spectrum. Initially, the octupolar field captures ions emanating from a diffusive jet flow; subsequently, the quadrupolar field radially compresses the ion packets for enhanced transmission through the narrow L3 aperture to the ToF-MS.

Gas injection and laser pulses must be synchronized for optimal performance. Helium gas is released into the segments for 240 µs, followed by the desorption/ablation laser pulse striking the sample surface after 4 ms, creating a plume. This is then exposed to a second ionization laser pulse 9 µs later. Ion thermalization begins in the early segments, continuing until segment S6 over 25 ms. By adjusting the voltage, ions move to S7, where axial compression of the ion packet occurs. After a 10 ms trapping period in S7, ions are moved to the RF hexapole ion guide, and finally directed through high vacuum DC lenses to the ReToF mass analyzer's extraction region. These time delays are shown in Figure 3.14.

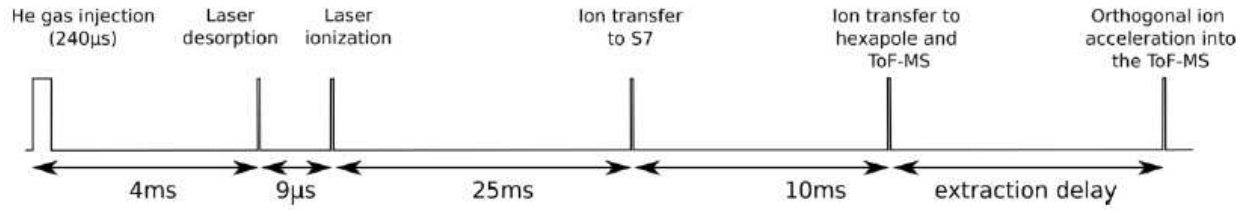

Figure 3.14 Synchronization between the different steps of the analysis, from He gas injection to the orthogonal ion acceleration into the ToF-MS.

The thermalized ions are separated and analyzed according to their *m/z* ratio in reflectron time-of-flight (ReToF) mass spectrometer. The signal is transferred to the PC for further analysis.

3.2 Raman Spectroscopy

Raman spectroscopy is an analytical technique that provides detailed chemical information by identifying the unique vibrational signatures of molecular systems. It is particularly effective for analyzing both biochemical and chemical samples, allowing for the characterization of materials, identification of molecular structures, and investigation of molecular interactions. Raman

spectroscopy is based on the inelastic scattering of light when it interacts with a sample [87]. This interaction excites the molecules to a virtual state, and as they return to a lower energy state, they scatter light. If the energy state after scattering differs from the initial state, there is a change in the light's wavelength, known as a wavelength shift. This shift may result in longer wavelengths (Stokes shift) or shorter wavelengths (anti-Stokes shift), directly indicating the energy difference between the molecular states. By integrating Raman spectroscopy with absorption and photoluminescence techniques, a comprehensive overview of a sample's spectroscopic characteristics can be achieved. Furthermore, monitoring the intensity of specific Raman bands enables the observation of dynamic changes within the sample.

3.2.1 Basics of Raman Spectroscopy

When light interacts with a molecule, it can be absorbed, transmitted, reflected, or scattered. Raman spectroscopy is concerned with scattering, known as Raman scattering. In this process photons are scattered by the molecules with a change in energy corresponding to the vibrational modes of the molecule.

In solid, under the influence of an electric field (E), the polarization (P) of a solid is expressed as the product of electric field and polarizability tensor (α), of atoms in the solid.

$$\mathrm{P} = \alpha \mathrm{E} \tag{3.9}$$

The polarizability tensor (α) represents the movement of the electron cloud and the atomic nucleus within the atoms when and electric field is applied. The tensor can be represented as:

$$\alpha = \begin{bmatrix} \alpha_{xx} & \alpha_{xy} & \alpha_{xz} \\ \alpha_{yx} & \alpha_{yy} & \alpha_{yz} \\ \alpha_{zx} & \alpha_{zy} & \alpha_{zz} \end{bmatrix} \tag{3.10}$$

When a solid is irradiated with the laser light of frequency ν_{exc} , the electric field oscillates as:

$$\mathrm{E} = \mathrm{E}_0 \sin(2\pi\nu_{\mathrm{exc}}\mathrm{t}) \tag{3.11}$$

Here, E_0 is the amplitude of the electric field. The irradiation leads to lattice vibrations which modify the polarizability tensor. This change can be defined as:

$$\alpha = \alpha_0 + \alpha_1 \sin(2\pi\nu_{\mathrm{vib}}\mathrm{t}) \tag{3.12}$$

Where α_0 is the polarizability of the atom in the solid at equilibrium and the term $2\pi\nu_{\mathrm{vib}}\mathrm{t}$ is the rate of change of polarizability with the vibration at equilibrium.

Therefore, the induced polarization is:

$$P_{ind} = \alpha E = [\alpha_0 + \alpha_1 \sin(2\pi\nu_{vib}t)] \times E_0 \sin(2\pi\nu_{exc}t) \quad (3.13)$$

The induced polarization (equation 3.13) can be expressed as:

$$P_{ind} = \alpha_0 E_0 \sin(2\pi\nu_{exc}t) + \frac{\alpha_1 E_0}{2}\cos(2\pi(\nu_{exc} - \nu_{vib})t) + \frac{\alpha_1 E_0}{2}\cos(2\pi(\nu_{exc} + \nu_{vib})t) \quad (3.14)$$

This equation 3.14 describes three main components:

1. ν_{exc}: Rayleigh Scattering, where the scattered light has the same frequency as the incident light due to the constant term in polarizability.
2. $\nu_{exc} - \nu_{vib}$: Stokes Scattering, where the scattered light has a lower frequency than the incident light, representing energy transfer from light to molecular vibrations.
3. $\nu_{exc} + \nu_{vib}$**:** Anti-Stokes Scattering, where the scattered light has a higher frequency, representing energy transfer from molecular vibrations to the light.

This formulation clearly shows that both Stokes and Anti-Stokes scattering, indicative of the Raman effect, depend on a change in polarizability. Without such changes, only the Rayleigh scattering component would be observed in the spectrum.

3.2.2 Principle of Raman Scattering

When photons from a laser beam hit atoms or molecules, they temporarily excite these particles to what are known as virtual energy levels—temporary states that don't correspond to the actual energy levels of the atoms or molecules. This interaction creates an oscillating polarization within the molecule, which can potentially interact with other types of molecular movements, such as vibrations.

In Rayleigh scattering, this oscillating polarization does not lead to any permanent change in the molecule's vibrational state. The molecule is excited but eventually returns to its original state, and the scattered light retains the same frequency as the incoming laser light as shown in Figure 3.15 (a). This type of scattering is termed "elastic" because there is no net energy change transferred to the molecule.

Raman scattering, on the other hand, involves a change in energy between the photons and the molecule. When the photon excites the molecule, it either gains or loses energy, moving to a different vibrational state than where it started. This results in the frequency of the scattered light

being different from that of the incoming photons as shown in Figure 3.15 (b) & (c). Specifically, in Stokes scattering, the molecule absorbs part of the photon's energy, decreasing the energy of the scattered light, shown by the frequency difference $\nu_{exc} - \nu_{vib}$. Conversely, in anti-Stokes scattering, the molecule starts in a higher energy state and releases energy to the photon, which increases the energy of the scattered light, resulting in a frequency increase $\nu_{exc} + \nu_{vib}$.

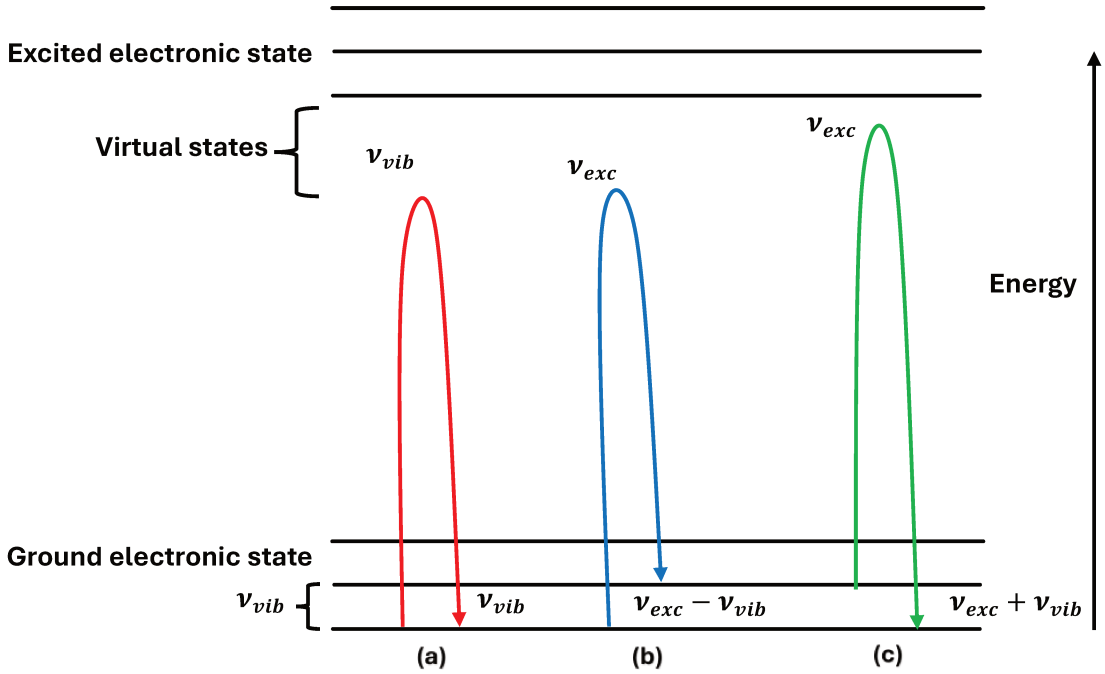

Figure 3.15 Elastic and non-elastic photons scattering behavior: (a) Rayleigh scattering (b) Stokes scattering (c) anti-Stokes.

3.2.3 Raman microscope instruments

The study of present and removal of Brominated Flame Retardants (BFR) from plastic films were conducted using two Raman microscopes: a LabRAM Soleil Microscope Confocal Multimodal (Figure 3.16) Raman available in HORIBA and a Renishaw InVia Reflex coupled with a confocal BFXM Olympus microscope (Figure 3.17) available at PhLAM laboratory. The spectra were obtained with laser excitation at 514.5 nm, 532 nm, and 785 nm over the spectral range between 100 and 4000 cm^{-1}. All the available excitation wavelengths were tried, and we selected the wavelength which helps to reduce fluorescence in Raman spectra. The spectrometer's aperture was set to a size of 100 and 200 micrometers. For measurement, 50x and 100x objective was employed, along with a grating specified at 600 lines per millimeter for a central wavelength of 500 nm with

the resolution of 4.8 cm^{-1} at 532 nm wavelength and 2.5 cm^{-1} at 785 nm. The spectrometer was calibrated using the Stoke Raman signal of pure Si (520 cm^{-1}).

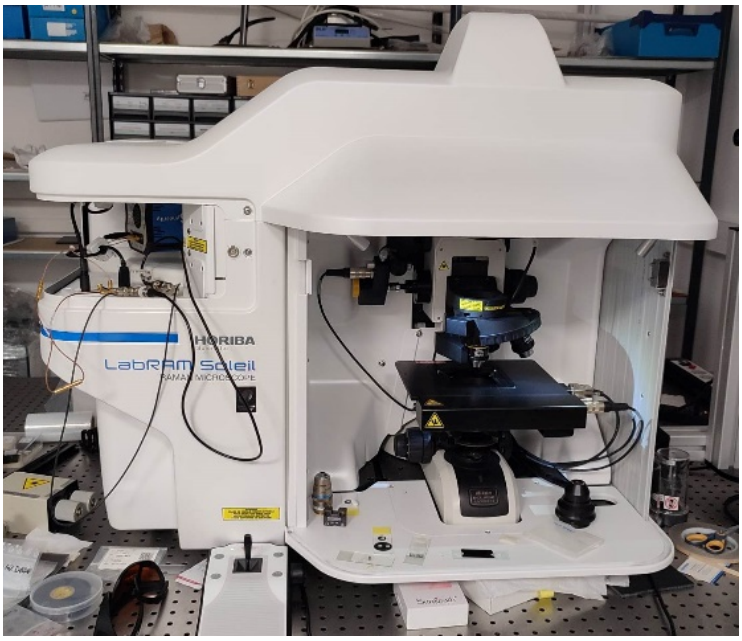

Figure 3.16 LabRAM Soleil Microscope Confocal Multimodal Raman available at HORIBA.

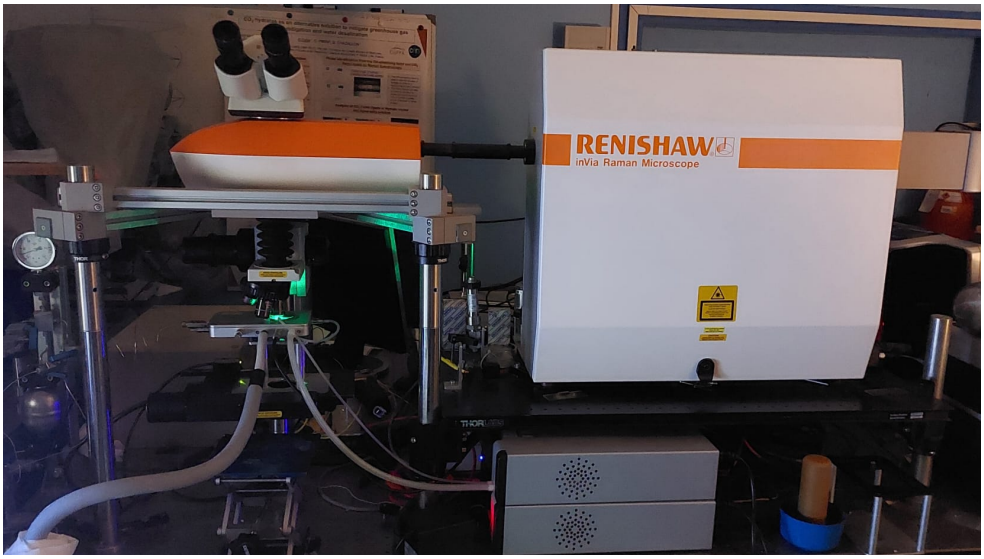

Figure 3.17 Renishaw InVia Reflex coupled with a confocal BFXM Olympus microscope available at PhLAM

3.3 Fourier Transform Infrared Spectroscopy (FTIR)

Fourier Transform Infrared (FTIR) Spectroscopy is a powerful analytical technique used to identify organic, polymeric, and, in some cases, inorganic materials. It provides qualitative and quantitative information about the molecular composition and structure of samples by measuring the absorption of infrared radiation.

3.3.1 Basics of FTIR Spectroscopy

Infrared absorption spectroscopy is a technique utilized by scientists to determine molecular structures based on the characteristic absorption of infrared radiation by the molecules. The resulting infrared spectrum represents the molecular vibrational spectrum. When a sample is exposed to infrared radiation, its molecules selectively absorb specific wavelengths, leading to a change in the dipole moment of the sample molecules. This absorption causes the vibrational energy levels of the molecules to transition from the ground state to an excited state. The frequency of an absorption peak corresponds to the vibrational energy gap, while the number of peaks is related to the molecule's vibrational degrees of freedom. The intensity of these peaks depends on the change in dipole moment and the likelihood of energy level transitions. By analyzing the infrared spectrum, one can obtain detailed structural information about a molecule. Most molecules exhibit infrared activity; however, homonuclear diatomic molecules like O_2, N_2, and Cl_2 do not, due to their lack of dipole moment change during vibration and rotation.

3.3.2 Principle of FTIR

Fourier Transform Infrared (FTIR) spectroscopy operates on the principle of measuring how different wavelengths of infrared light are absorbed by a sample. When infrared radiation interacts with a molecule, it can cause the molecule to vibrate at specific frequencies, which correspond to the energy differences between the ground and excited vibrational states. An FTIR spectrometer simultaneously collects spectral data over a wide range of wavelengths, and then applies a mathematical Fourier Transform to convert the raw data into an interpretable spectrum. This spectrum displays the unique absorption characteristics of the sample, reflecting the molecular vibrations and providing insights into the molecular structure and composition. The resulting

absorption peaks are indicative of specific molecular bonds and functional groups, allowing for detailed analysis of the sample's chemical properties.

3.3.3 FTIR experiment

The FTIR analysis of debromination of HIPS was performed using a Bruker VERTEX 70 spectrometer to analyze changes in molecular structure. Polymer samples (film) were deposited on a gold mirror (no infrared signal from gold) and analyzes through the absorption-reflection microscope within a range of 398.1-5001 cm^{-1}. The number of accumulated scans was 32, with the resolution of 1 cm^{-1}. The collected spectra were corrected for baseline and normalized. Figure 3.18 shows the picture of FTIR used in this experiment.

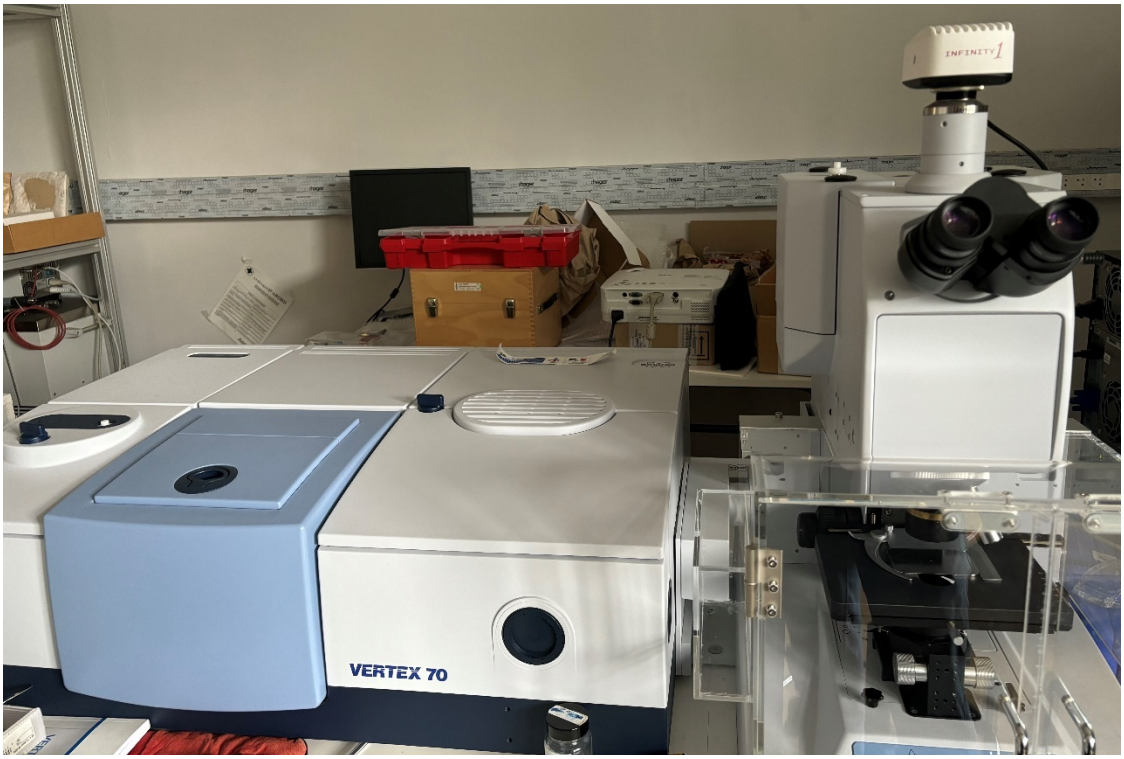

Figure 3.18 Picture of FTIR used during the HIPS (plastic sample) analysis available in PhLAM laboratory.

Chapter 4 Development of the atmospheric-pressure interface for mass spectrometry analysis

This chapter details the development of an interface designed to transfer analytes originating from liquid or solid samples from atmospheric pressure to a vacuum for mass spectrometry analysis. Various configurations using solenoid pulsed valves and tubing were tested, and their advantages and disadvantages are discussed comprehensively. A broad range of chemical samples were employed to evaluate the transfer capabilities of these configurations, providing a vast data set.

The first section provides a technical description of the various components required to build the lines. Then, for each configuration tested, the associated sections first describe the technical scheme used and then present the results obtained. For liquid samples (section 4.2), two configurations were employed, both utilizing a single valve but differing in its location, either connected to a CF port of the chamber ("Valve 1", 20 V) or placed as close as possible to the ionization/extraction zone of the spectrometer ("Valve 2", 28 V). For solid samples, six configurations were tested. In the first cases (section 4.3), the valve was positioned at either one or the other position. Additionally, configurations with valves in both positions (section 4.4), thus forming an airlock, were tested. These latter configurations are proposed as solutions to some of the problems encountered in single-valve configurations, and represent the current solutions and future prospects of this work.

4.1 Material and preliminary experiments

4.1.1 Vacuum chamber – Volume estimation

Together with pumping speeds, the internal free volume has a direct influence on the species density over time in the spectrometer after the opening of a pulsed valve. It thus determines the possible opening durations of the valve in order to remain within the pressure operating limits of the instrument. Knowledge of this volume is therefore vital, especially if the transfer line is to be coupled to a different instrument.

The mass spectrometer on which the development is being carried out comprises two vacuum chambers: a spherical one containing the ion extraction and acceleration zones, and a cylindrical

tube 1 m long and 20 cm in diameter containing the free-flight zone, the reflectron and the MCP detector. The stainless-steel spherical vacuum chamber (SP1800S, Kurt J. Lesker company) is shown in Figure 4.1. It has an 18" outer diameter (OD) and includes 19 ports to connect different devices, like the ToF tube, turbomolecular pumps, pressure gauges, a sample transfer arm, a cryostage to cool down samples, and windows for laser entrances. It has 6 DN160CF ports (8.00-inch OD), 1 DN100CF port (6.00-inch OD), 4 DN63CF ports (4.50-inch OD), 8 DN35CF-DN40CF ports (2.75-inch OD).

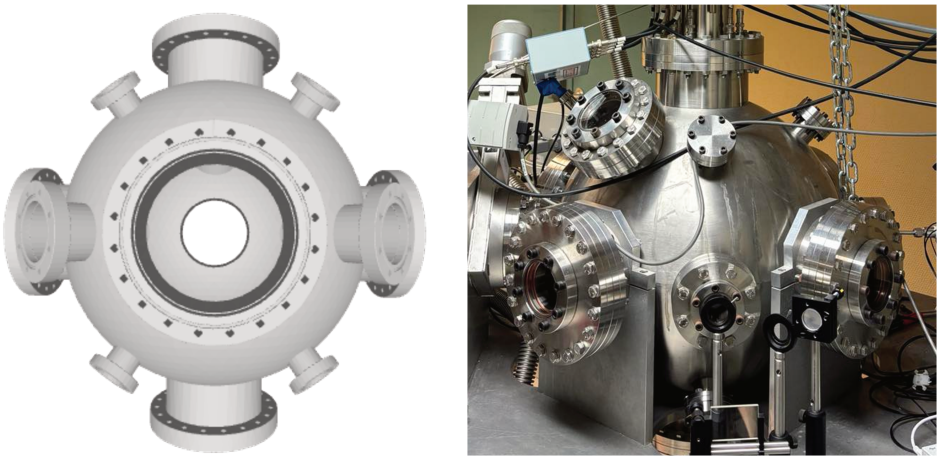

Figure 4.1 Spherical vacuum chamber from Kurt J. Lesker company, to which the transfer line developed in this thesis is coupled.

To generate the vacuum inside this spherical chamber and the ToF tube connected to it, two turbomolecular pumps are used: a TwissTorr 704 FS (Agilent Technologies) with pumping speed of 700 L/s connected to the spherical chamber with a DN 160 CF port, a HiPACE 300 TC 400 (Pfeiffer Vacuum) with pumping speed of 260 L/s connected with DN 100 CF port for the time-of-flight tube. These two turbomolecular pumps are connected to a dry scroll primary pump (IDP-15 Agilent Technologies) which is oil-free and achieves a base pressure of 1.3×10^{-2} mbar, with a pumping speed of 214 L/min (12.8 m^3/h). To monitor the pressure inside the chamber and ToF tube, two combined Bayard Alpert hot cathode and Pirani pressure gauges (Compact Full Range BA gauges PBR 260, Pfeiffer Vacuum) are used which can measure the pressure in the range of 5×10^{-10} to 1000 mbar. After running the pumps overnight, pressure in the system is around 10^{-8} mbar.

Evaluation of the internal free volume of the spectrometer

The total free volume of the spectrometer can be roughly estimated using the geometrical dimensions of its two main elements (spherical chamber and ToF tube). Using the dimensions given above, we find a volume of 81 l and up to 85 l if we estimate the additional volume of the ports. However, since some vacuum devices are also connected to the chambers, and the inside space is not completely empty, we also tried to evaluate the free volume using filling experiments at a constant flow from secondary vacuum to atmospheric pressure. The spectrometer is isolated from the pumps by closing the corresponding valves. A mass flow controller (EL-FLOW Select F-201CV, 10 slm N_2, Bronkhorst) is used to monitor the flow of nitrogen as a function of time, when set to 3 l/min. In Figure 4.2, the measured flow rate is displayed against time. Its value is effectively constant except during the transient regimes corresponding to flowmeter start-up and the approach of atmospheric pressure, since the flowmeter opening is limited, and the pressure drop is greater. The volume sought corresponds to the integral of the signal, i.e. 83.9 L.

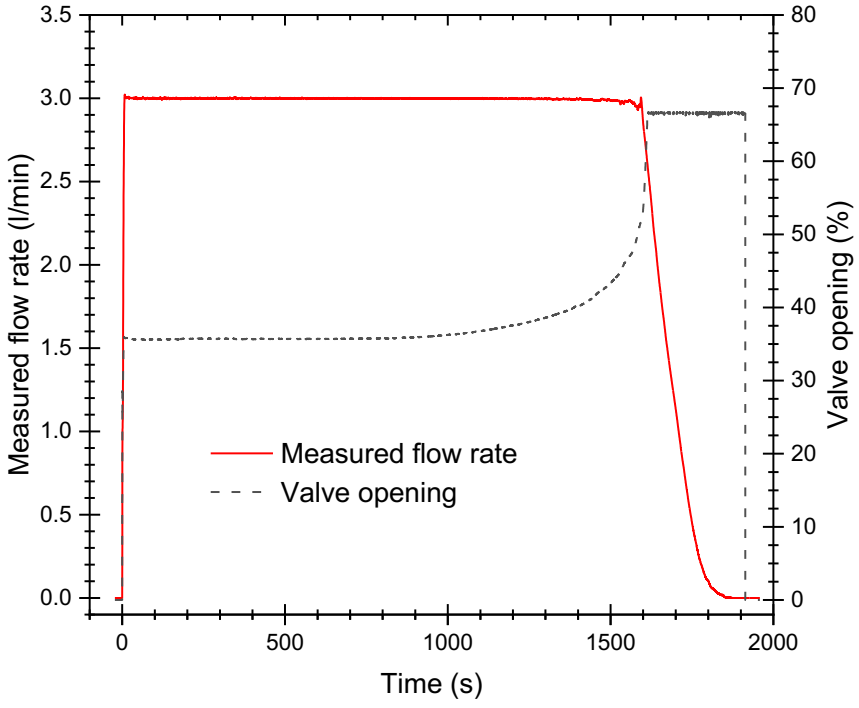

Figure 4.2 Variations of the measured flow rate and valve opening with time, when filling the spectrometer at a 3 l/min flow rate setpoint.

4.1.2 Pulse valves

Pulse solenoid valves are high speed valves, with ultra-low leak rate, high flow, and high temperature capability. Pulse valves coils are rated for continuous duty and are potted to exclude the environment. Pulse valves used in this work are Parker VAC-1250 PSIG, with orifice size 0.79 mm. The pulse valve consists of small cavity which is connected to ¼" A-Lok tube fittings. Another end of the cavity is connected to a small orifice of diameter 0.79 mm, which opens outside the valve. The orifice and the cavity are isolated by PTFE poppet (white in color) or Vespel poppet (brown in color), in which Vespel is better for temperature resistance. This poppet is spring loaded, and it is closed when not in use, and is opened by solenoid. There is a small space close to the poppet which makes the exit cone while valve is ON, and no exit cone while it is OFF. This valve can reach pressure up to 1250 PSI (86.2 bar). There are two kinds of Parker solenoid pulse valves available in the market. Picture of two solenoid valves is shown in Figure 4.3, where one of the valves is connected to a flange. These valves have different electrical properties (see Table 4.1).

Table 4.1 Electrical properties of both valve types

Type	I	II
Voltage (VDC)	20	28
Power (W)	12.1	11.2
Current (mA)	606	400
Resistance (Ω)	33	70

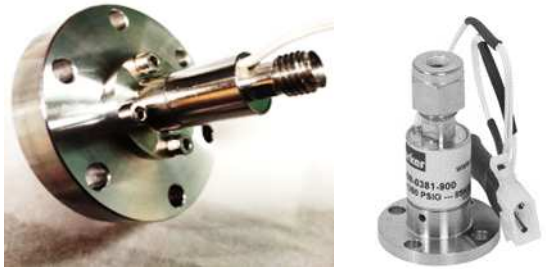

Figure 4.3 Pictures of valves: (a) type I (20V) valve connected to a flange, (b) type II (28V) valve.

These valves are driven by the Hit and Hold method, which reduces the power consumption and heat generation. The valve is "hit" with the rated voltage for time period of 25 ms and then "held" open with the hold voltage (reduced voltage) for the remaining desired ontime. Table 4.2 and voltage graph in Figure 4.4 will show the rated voltage and the holding voltage, with the time. In the graph T0 to T1 is the hit timing and T1 to T2 is the holding time.

Table 4.2 Hold voltage and power for two different valves with different rated voltage

Rated Voltage (V)	Hold Voltage (V)	Hold Power (W)
28	6	0.51
20	5	0.76

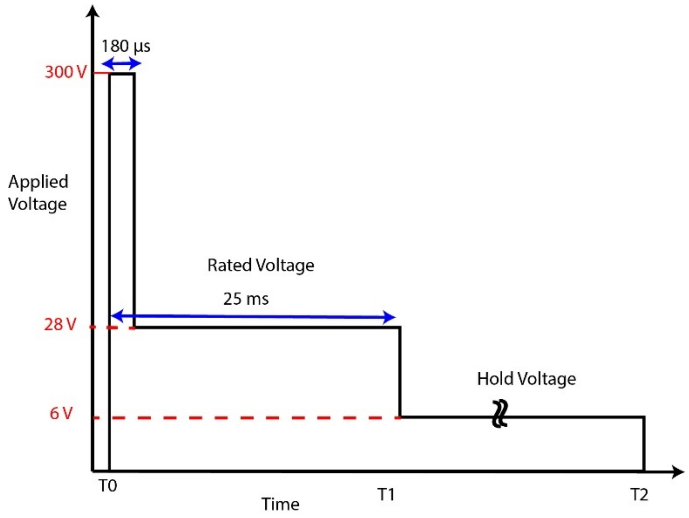

Figure 4.4 Voltage graph for a type II valve. IOTA ONE hits the valve with high voltage of 300 V for 180 µs for fast opening, then the pulse decreases to rated voltage of 28 V for 25 ms, and decreases to hold voltage of 6 V.

To drive the valve, it is required to generate the pulse shown in the hold voltage graph in Figure 4.4. Parker IOTA ONE pulse driver is used to drive these valves which is described in next section.

4.1.3 IOTA ONE pulse driver

IOTA ONE pulse drivers generate a pulse of high voltage between 280 V to 300 V, which opens the valve very fast. The pulse then decreases in voltage over the course of 180 µs to its rated value

of 20/28 V and is followed by a pulse of hold voltage of 5/6 V. During this thesis, with the help of the electronic workshop at PhLAM laboratory, a replica of IOTA ONE pulse driver was developed. For the development of this pulse driver, the pulse shape, voltage, and current characteristics of the IOTA ONE (60-1-900, General Valve corporation) were investigated (see Figure 4.8). These characteristics are discussed below. To capture the voltage signal pulse shown in Figure 4.5, the output from the IOTA ONE (not loaded with the valve) was directly linked to an oscilloscope via a 10X voltage probe. This probe attenuates the output voltage by a factor of 10 before it reaches the oscilloscope, ensuring the signal level is within a safe range for the oscilloscope to process.

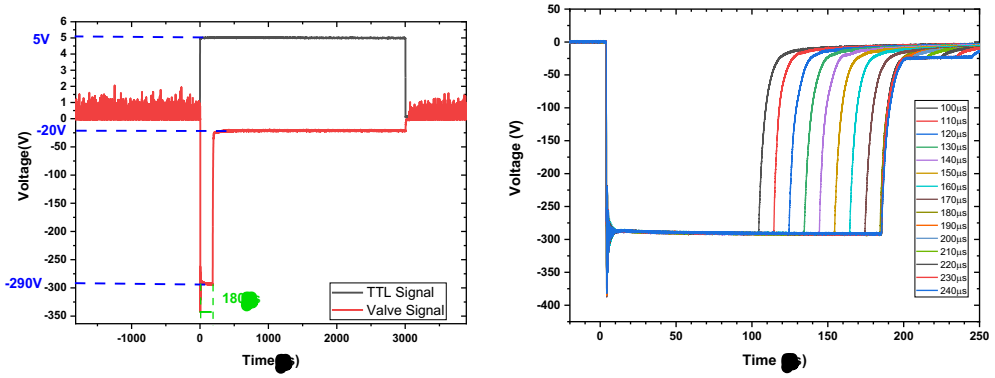

Figure 4.5 (Left): Output "VALVE" signal generated by the IOTA ONE for a 3 ms ontime setpoint (type I valve) and recorded on an oscilloscope using a 10X probe (red signal) and corresponding "TTL OUTPUT" signal (black curve), (Right): Close-up on the output "VALVE" signal for various ontime setpoints. The -290 V high voltage duration is limited to 180 µs and followed by -20 V rated voltage if the setpoint is longer.

Figure 4.5 on the left illustrates that the IOTA ONE produces a high voltage pulse of -290 V for a maximum of 180 µs, which enables the fast opening of the valve. This rapid activation is followed by a holding voltage of -20 V until the end of the 3 ms setpoint time programmed in our example on IOTA ONE. In this work, an IOTA ONE with a 20 V specification is utilized; however, if a 28 V version of the IOTA ONE were used, the holding voltage would be -28 V instead. The left part of Figure 4.5 shows the voltage signal captured over a broad time scale to reveal the shape of the pulse generated. Conversely, the right part of Figure 4.5 presents these signals captured at various opening durations to verify the pulse voltage produced during the valve's brief opening period. This effectively demonstrates that a -290 V voltage is generated for 180 µs to facilitate rapid opening, followed by the pulse voltage stabilizing at -20 V to keep the valve open.

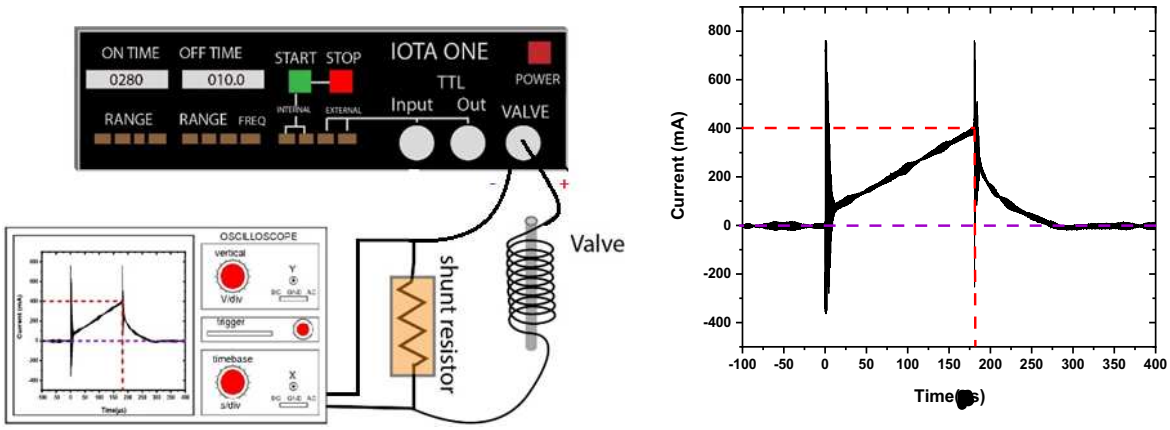

Figure 4.6 (Left): Circuit to measure the current in the solenoid valve during operation, (Right): Current signal in the valve deduced from the voltage across the shunt resistor on an oscilloscope using the left circuit.

When voltage pulse shape is known, to develop this device current needs to be measured and pulse shape needs to be recorded. To measure the current, circuit shown on left of the Figure 4.6 is used, in which shunt resistor of 1 Ω (ohm), IOTA ONE pulse driver, and valve are connected in series, and to plot the trace oscilloscope is connected in parallel to the shunt resistor. Utilizing the Ohm's law, the maximum current is determined to be 400 mA. This current swiftly rises to 400 mA within 180 µs (microsecond) and, upon reaching its peak, quickly falls back to 0 mA.

Using the voltage and current specifications of the IOTA ONE to operate the 20 V valve, the replica of IOTA ONE (depicted on the right side of Figure 4.8) was developed. This was achieved by employing the electronic circuit shown in Figure 4.7.

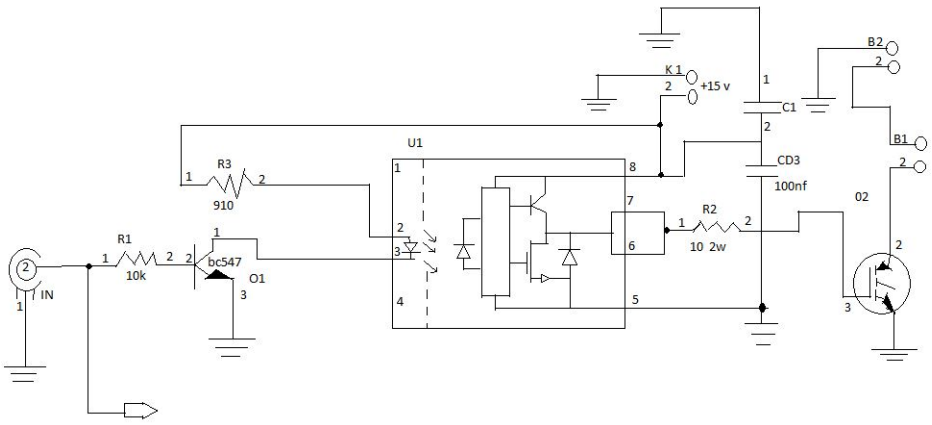

Figure 4.7 Electronic circuit of the pulse driver developed at PhLAM laboratory.

Figure 4.8 Left) Picture of IOTA ONE pulse driver, right) Picture of replica of IOTA ONE pulse driver (in red square) developed in PhLAM laboratory, connected with pulse generator, 300 V power supply, 15 V power supply.

4.1.4 Determination of the possible valve's operating range

In order to work under optimum conditions and avoid damaging the MCPs, it is advisable not to work at pressures higher than 10^{-6} mbar. Figure 4.9 shows the evolution of the pressure in the extraction chamber as a function of the 20 V valve ontime and at a 10 Hz repetition rate. First, the valve can be operated for ontimes as short as 110 µs. In addition, for the mass spectrometer used, the valve is operable at the 10 Hz frequency of our Nd-YAG lasers for ontime lower than 130 µs in order to comply with the required working pressure. Extrapolation to other mass spectrometers also requires taking into account the volume of the extraction chamber as well as the pumping speed as discussed earlier.

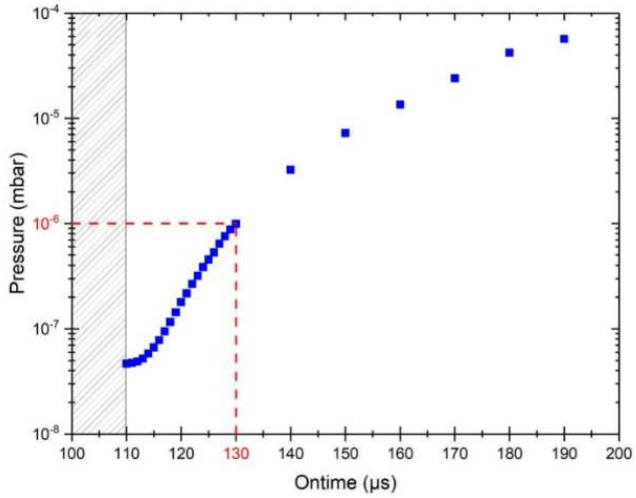

Figure 4.9 Variation of the pressure inside the extraction chamber of the mass spectrometer as a function of the valve ontime at a 10 Hz repetition rate.

Several absolute pressures upstream of the valve were also tested from 1 to 2.6 bars, and the pressure in the chamber is always higher than the pressure recorded at 1 bar as shown in Figure 4.10. This pressure evolution is recorded using a 20 V valve.

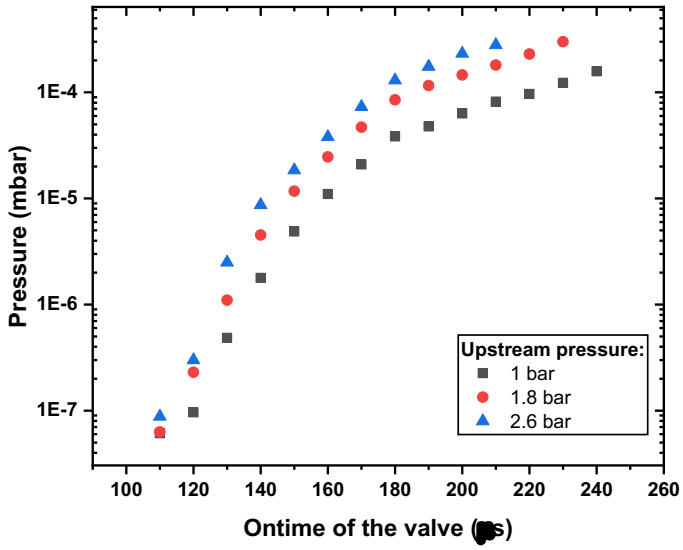

Figure 4.10 Variation of the pressure inside the extraction chamber of the mass spectrometer as a function of the 20 V valve ontime at different upstream pressures and a 10 Hz repetition rate.

In Figure 4.11, the red and black curves show the pressure variations in the extraction chamber using a 20 V and 28 V valve. From this plot we deduce that the 28 V valve offers easier control of the pressure inside the chamber.

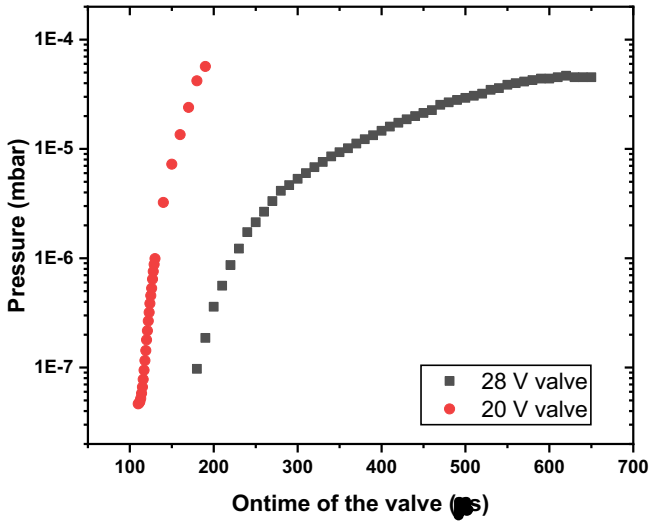

Figure 4.11 Variation of the pressure inside the extraction chamber of the mass spectrometer with the valve ontime at a 10 Hz repetition rate. 28 V valve (black curve), 20V valve (red curve).

In the following sections, the 20 V valve ("Valve 1") will always be connected to a flange of the vacuum chamber and the 28 V valve ("Valve 2") will be placed close to the extraction region of the spectrometer.

4.1.5 Evaluation of the standard volume injected during a single valve opening

Theoretical determination

To estimate theoretically the standard volume injected during the valve ontime, we can use the orifice equation giving the flow rate Q [88]:

$$Q = C_d \times A \times \sqrt{\frac{2\Delta P}{\rho}} \tag{4.3}$$

with A the area of the orifice, ΔP the differential pressure, and ρ the gas density. A valve with an orifice diameter of 0.79 mm is used, the area of the orifice is $4.9 \times 10^{-7}\mathrm{m}^2$. The pressure drops from 1 bar at the inlet to the range of 10^{-8} mbar in the vacuum chamber, $\Delta P = 1\mathrm{bar} - 10^{-8}\mathrm{mbar} = 1\ \mathrm{bar} = 10^5$ Pa. The discharge coefficient (C_d) can be assumed to be 0.61 from

Torricelli's law (also known as Torricelli's theorem for small orifices). Nitrogen density ρ has a standard value of 1.25 kg/m^3. Using these values, the calculated flowrate is:

$$Q = 0.61 \times 4.9 \times 10^{-7} \sqrt{\frac{2 \times 10^5}{1.25}} = 1.2 \times 10^{-4}\ \mathrm{m^3/s} \tag{4.4}$$

For a valve ontime of 200 µs, the injected volume V per valve opening is:

$$V = 2.4 \times 10^{-8}\ \mathrm{m^3} = 24\ \mu\mathrm{l} \tag{4.8}$$

Experimental determination of the standard injected volume

The flowmeter used is a Bronkhorst F-201CV [89], and the measurement was conducted using the Flowsuite software. Figure 4.12 illustrates the connection of the flowmeter to the valve and transfer line.

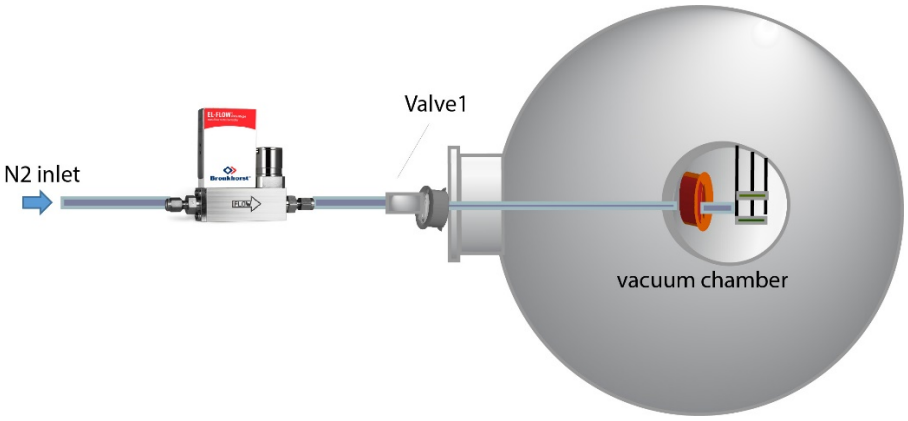

Figure 4.12 Schematic of connection of the flowmeter to the nitrogen gas inlet and to the valve.

The average flow rate is recorded for different ontimes of the valve for a 10 Hz repetition rate. The increase of the valve average flow rate with ontime is reported in Figure 4.13 for two upstream pressures of nitrogen. At 200 µs ontime and a 10 Hz repetition rate, the average flow rate is 2 ml/min, which corresponds to 3.3 µl per valve opening. This value is almost one order of magnitude lower than the theoretical one. It outlines that the ontime setpoint of the valve does not reflect the real opening duration and that the gas flow is probably not constant during the valve ontime.

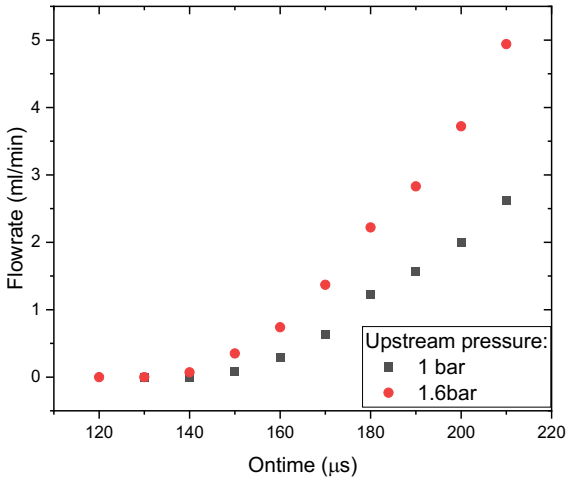

Figure 4.13 Flowrate comparison for two upstream pressures of nitrogen using a 20V valve at 10 Hz repetition rate.

4.1.6 Synchronization of valves and lasers

Achieving optimal spectra and effectively developing the instrument hinges on precise knowledge of the species travel time between points, including the optimal moments for opening the valve (where ontime of valve is controlled by IOTA ONE) and firing the lasers. This interval is referred to as the "delay". To ensure seamless synchronization of all components, it is essential to approach the process methodically, progressing step by step. This gradual approach allows for the precise timings between the desorption, valve operation, and ionization stages, which is crucial for efficient mass spectrometry analysis.

Two four channel digital delay/pulse generators (STANFORD RESEARCH SYSTEM, INC. DG 535) [90] were employed to synchronize (see Figure 4.14).

The DG535 Digital Delay and Pulse Generator offers four precisely timed logic transitions or two independent pulse outputs. The delay resolution on all channels is 5 ps, and the channel-to-channel jitter is typically 50 ps. Front-panel BNC outputs deliver TTL, ECL, NIM or variable level (-3 to +4 V) pulses into 50 Ω or high impedance loads. With its high accuracy, low jitter, and broad delay range, the DG535 is well-suited for applications such as laser timing systems, automated testing, and precision pulse generation.

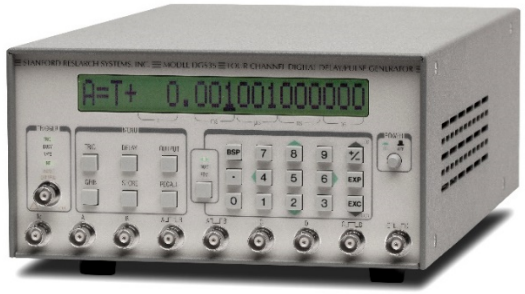

Figure 4.14 Picture of the DG 535 four channel delay/pulse generator (STANFORD RESEARCH SYSTEM, INC.).

There are four delay output channels: A, B, C and D. The logic transitions of these outputs can be delayed from an internal or external trigger by up to 1000 seconds in 5 ps increments. The T0 pulse, which marks the beginning of a timing cycle, is generated by the trigger signal. In addition to the four delay outputs, there are four pulse output channels: AB, -AB, CD and -CD. The leading edge of the AB pulse coincides with the leading edge of the earlier of A or B, and the trailing edge of AB coincides with the leading edge of the later of B or A.

Two DG535 pulse generators were available to synchronize the valves and lasers. Additionally, a home-made pulse shaping device allowing us to transform Heaviside's outputs A, B, C, or D of the generators into 15 µs wide pulses with the required impedance was used to trigger the lasers' flashlamp and Q-switch.

4.2 Transfer of vapor sample

Section 4.1 of the manuscript concentrated on analyzing pressure variations and flow rates to determine the possible working points of the valve for adequate Time-of-Flight Mass Spectrometry analysis. Achieving a controlled pressure within the chamber is essential for effective ToF analysis, requiring a balance between a high vacuum preventing losses of species by collision and high density of analytes to get the highest possible signal. The length and position of the tube, as well as the timing of the valve's operation, are critical in transferring molecules efficiently.

The instrument development is a step-by-step process where each version of the setup undergoes testing before moving to the next stage. This process typically includes experimenting with various designs to find the most efficient one. The next sections discuss the different configurations tried in this thesis, showcasing the iterative nature of the development processes. It is crucial to test multiple setups to identify the most effective solution.

In developing an atmospheric pressure sampling interface for L2MS, the initial focus is on assessing the ability to desorb species from a solid sample, transfer molecules into vacuum, and ionize them. In a first step, we focus on the transfer of vapor samples that eliminates the need of desorption.

4.2.1 Synchronization scheme

Figure 4.15 shows the electronic scheme used to trigger the solenoid valve and the Nd:YAG laser performing the ionization of the species. Two delay generators are used for practical purposes with the synchronization schemes of the next configurations. Delay generator D1 is internally triggered at 10 Hz. It triggers the IOTA ONE controller using its AB output channel and acts as the master of delay generator D2 through its T0 output channel. Delay generator D2 controls the trigger of ionization laser, for both the flash lamps and Q-Switch. The delay values of channels C and D are set as follows: $C = D - 275$ µs and $D = T + z$ µs. These outputs are connected to a home-made pulse shaping instrument to transform the Heaviside's C and D outputs into 15 µs wide pulses with high impedance. 275 µs is the delay between outputs C and D. It corresponds to the delay between flashlamp and Q-switch of the ionization laser and allows us to modify the laser output energy. The z value of channel D is used to tune the delay between valve opening and ionization laser Q-switch.

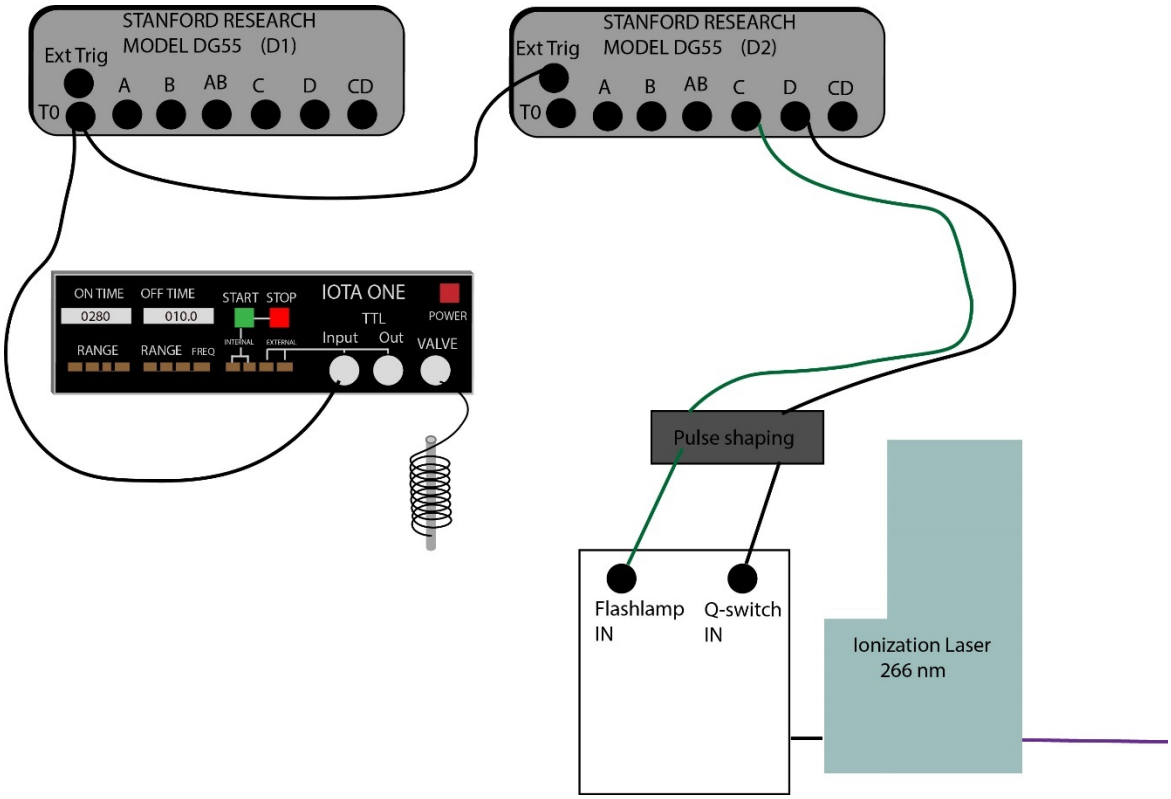

Figure 4.15 Synchronization scheme of the valve and the ionization laser. Delay generator D1 is internally triggered at 10 Hz.

Due to the electronics in the valve controller (IOTA ONE), there is an inherent delay between the trigger input and the valve opening. In our lab, we have two valve controllers, one operating at 20 V and the other at 28 V. Figure 4.16 illustrates the recorded time sequences for trigger input and valve opening for these two different controllers. For the 20 V controller, a delay of 600 ns was observed between the trigger in and the valve signal that we associate with the valve opening. In contrast, the 28 V controller exhibited a significantly longer delay of 80 µs.

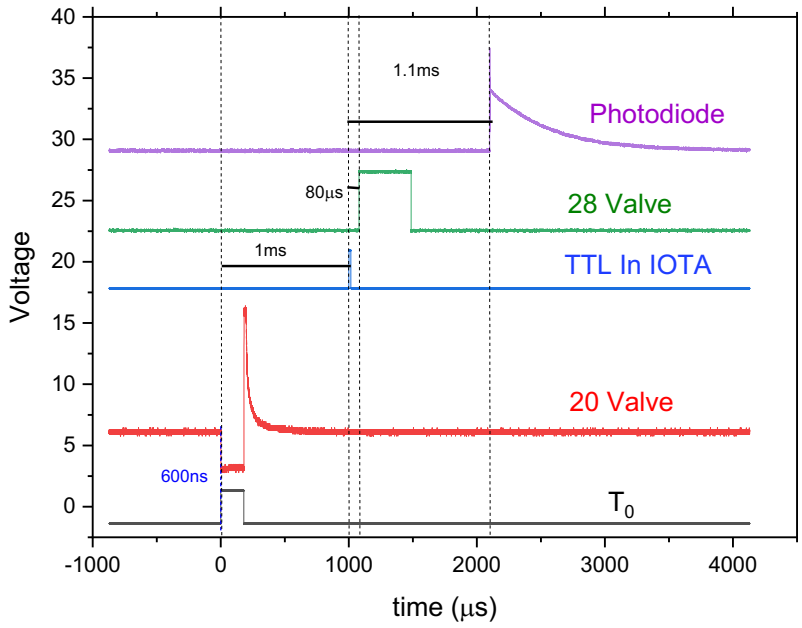

Figure 4.16 Time sequence for electronic jitter in IOTA ONE for two different valve, with the time sequence of photodiode which is ionization Q-switch.

4.2.2 Configuration 1: Single valve on a spectrometer port

Schematic

The initial setup tested for analyzing vapor samples is displayed in Figure 4.17. In this configuration, the vapor is sourced from a flask. A stream of nitrogen, coupled with the activation of a valve, facilitated the introduction of the vapor into the vacuum chamber. The vapor was then directed towards the mass spectrometer's extraction plates through a 1/8" Teflon tube of 90 cm connected to the valve. Following this, the species underwent photo-ionization by a nanosecond pulsed laser (second harmonic of an Nd:YAG laser, with a wavelength of 266 nm and a repetition rate of 10 Hz). The laser's optical path was positioned between the extraction plates, and its operation was synchronized with the valve's opening sequence.

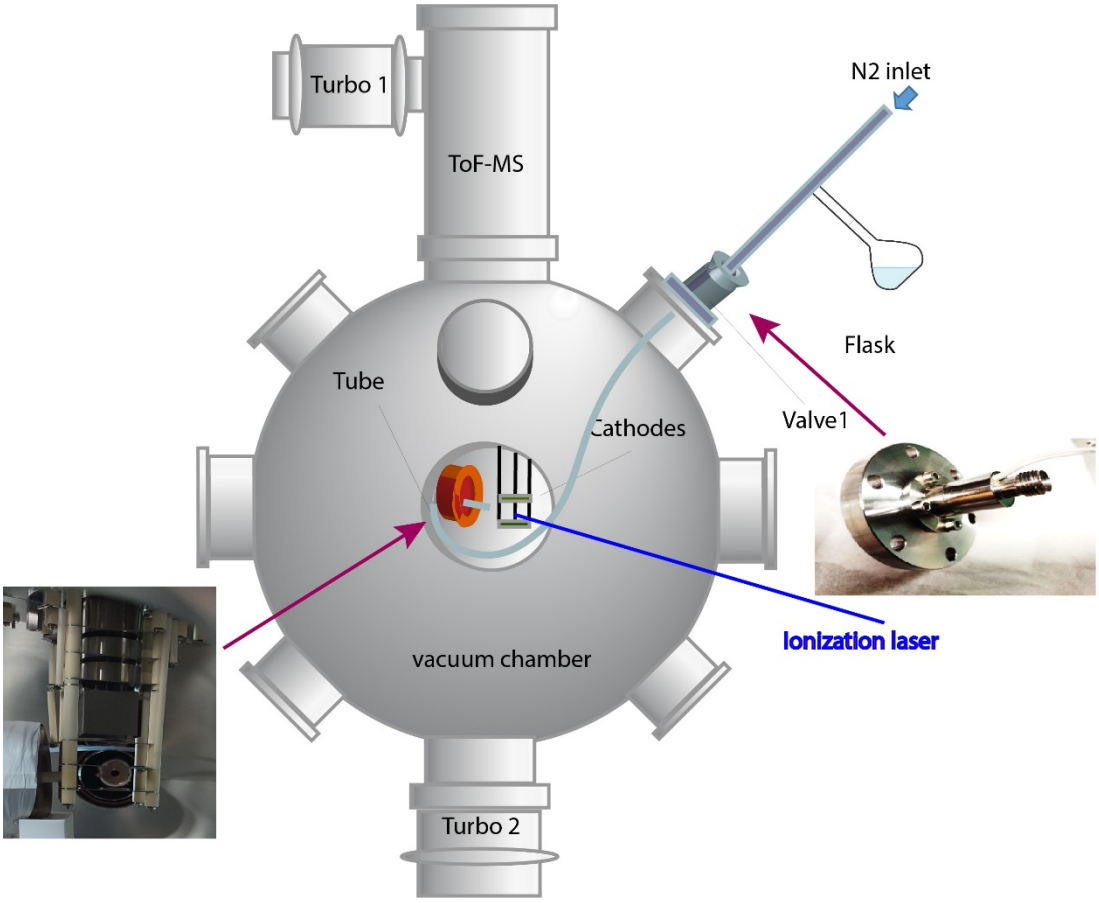

Figure 4.17 Schematic of the experimental device developed to carry out the first transfer tests of chemical species from the atmosphere to the vacuum enclosure.

Results

In the conducted experiment on vapor sample, kerosene was chosen as test sample. Kerosene's volatile properties made it a suitable candidate for testing the system's efficiency in transferring molecules to the extraction region and in assessing the alignment of the ionization laser.

A spectrum of kerosene was recorded at an ionization energy of 3.25 mJ, and with an elongated 16.5 mm^2 laser spot. The valve ontime was 180 μs and the delay between valve opening and ionization was set arbitrary to 90 μs. This latter value has been tuned in the 0-100 ms range corresponding to the delay between two consecutive laser pulses at 10 Hz, but no optimum for the MS signal could be found. This suggests that the puff of chemical species introduced when the

valve is opened is very strongly spread over time during transfer through the Teflon tube, and that the spectrum measured is the result of the accumulation of species over several laser shots.

A total of 1000 spectra is averaged in Figure 4.18. The spectrum is characterized by volatile species such as alkylbenzenes and semi-volatile species such as naphthalene, as well as their photofragments. It should be noted that with ionization at 266 nm, only aromatic species can be ionized by two-photon resonant ionization. The aliphatic species that make up the majority of kerosene are therefore not observed.

These aspects were crucial in evaluating the molecule transfer and ionization process. However, it's important to note that while the results gave some indication of the system's performance for transfer of vapor phase analytes, they also underscored the necessity for further adjustments, particularly in the laser alignment and handling of volatile substances.

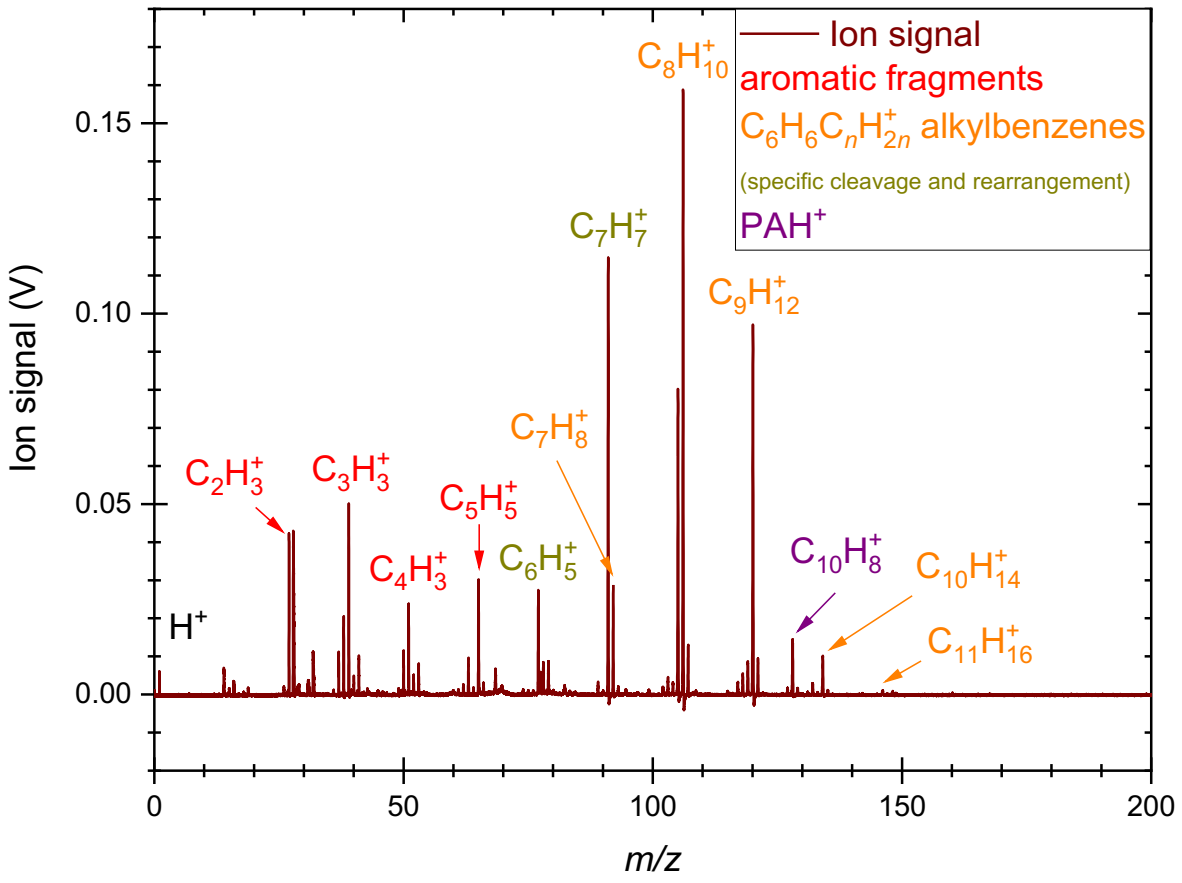

Figure 4.18 Kerosene spectrum recorded at ionization energy of 3.25 mJ, and 180 µs valve ontime. It exhibits high fragmentation due to the high ionization energy..

When the pulsed valve is switched on at 10 Hz, the pressure rises from the residual pressure (valve off) to settle at a working pressure that has been measured and presented in Figure 4.9. This working pressure varies with the duration of the pulsed valve opening, and its value depends mainly on the average gas inlet flow into the chamber through the valve, the pumping speed of the two turbomolecular pumps and the complex geometry inside the chamber. During operation, the response time of the hot cathode gauges (Pfeiffer Compact FullRange™ BA Gauge PBR 260) and the refresh time of the display (Pfeiffer VACUUM MaxiGauge^{TM} TPG 256 A) of the order of magnitude of a second make it impossible to follow directly the pressure variations linked to the opening and closing of the valve, and therefore to have information on the density of species in the chamber or even less close to the spectrometer's ionization zone. To get insight into the characteristic variation times of the average density of ionizable chemical species in the spectrometer's extraction zone, mass spectra were recorded at the ionization laser's operating rate (10 Hz) using a LeCroy WaveSurfer 64MXs-B 600 MHz oscilloscope, with traces written to binary files.

The evolution of the ion signal after opening or closing the valve was studied in detail. To do this, the peaks present in the mass spectra of a kerosene vapor were summed for each laser shot, so that a point corresponds to the total integrated ion signal of a mass spectrum. Variations in the total ion signal are shown in Figure 4.19. Transient regimes after valve start-up or shutdown are empirically adjusted by decreasing exponential functions. The characteristic times τ for establishment of working pressure and return to residual pressure are 0.33 s and 0.91 s respectively. The latter time, essentially related to pump efficiency and system geometry, gives the minimum time required to record a new spectrum without risk of contamination by residual pressure in the spectrometer in the case of rapid time variations, such as for chemical mapping using mass spectrometry.

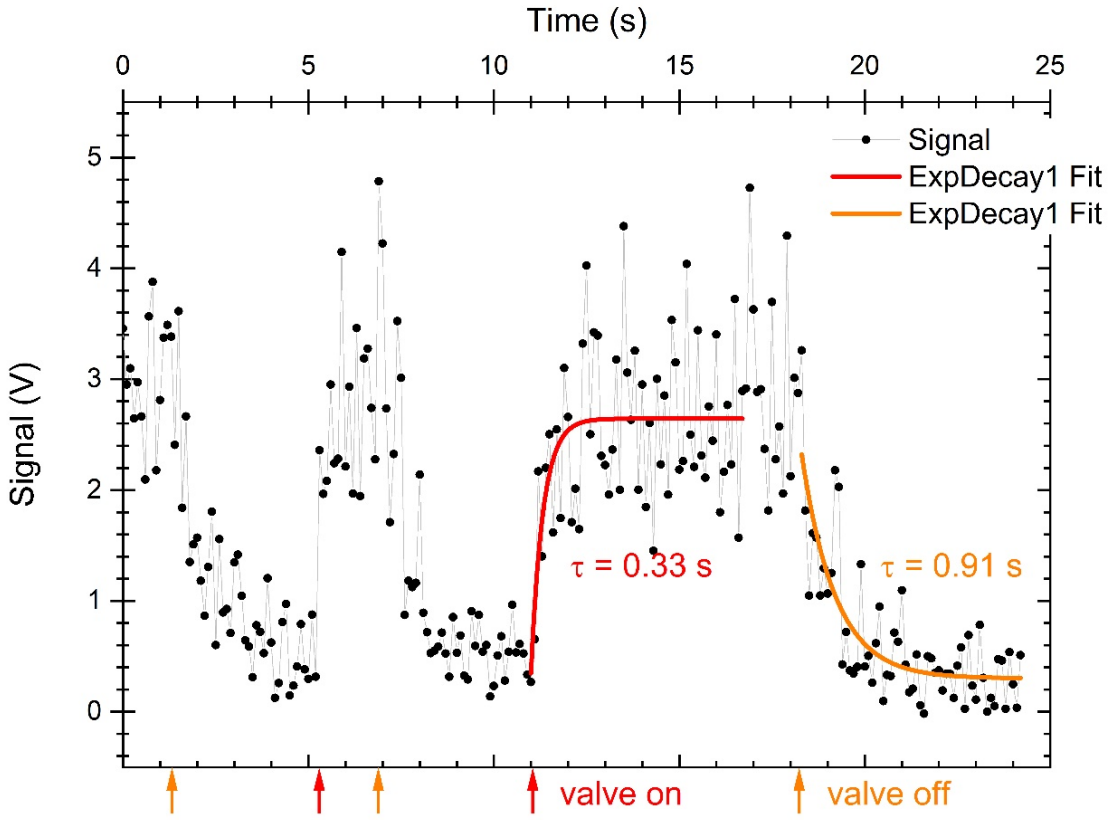

Figure 4.19 Pulse to pulse ion signal variation recorded to evaluate the characteristic times for the establishment of a maximum ion signal in the spectrometer and its return to the background signal after the valve is switched on and off respectively at 180 µs ontime of the valve.

4.2.3 Configuration 2: Single valve close to the extraction zone

Schematic

To increase the analyte density in the ionization zone and potentially shorten the time to return to residual pressure in the chamber, the valve has been placed within the chamber, in proximity to the mass spectrometer's extraction plates. A sampling interface tube, designed to transport chemical species from the external atmosphere to the extraction area, is attached to another port that is closer to the extraction zone. This tube, made of Teflon, has a outer diameter of 1/8 inches and a length of 50 cm, and is bent to accommodate the limited space inside the chamber.

In addition, a flask filled with kerosene is connected to the outside of the chamber, forming part of the streamlined single-valve configuration (Figure 4.20).

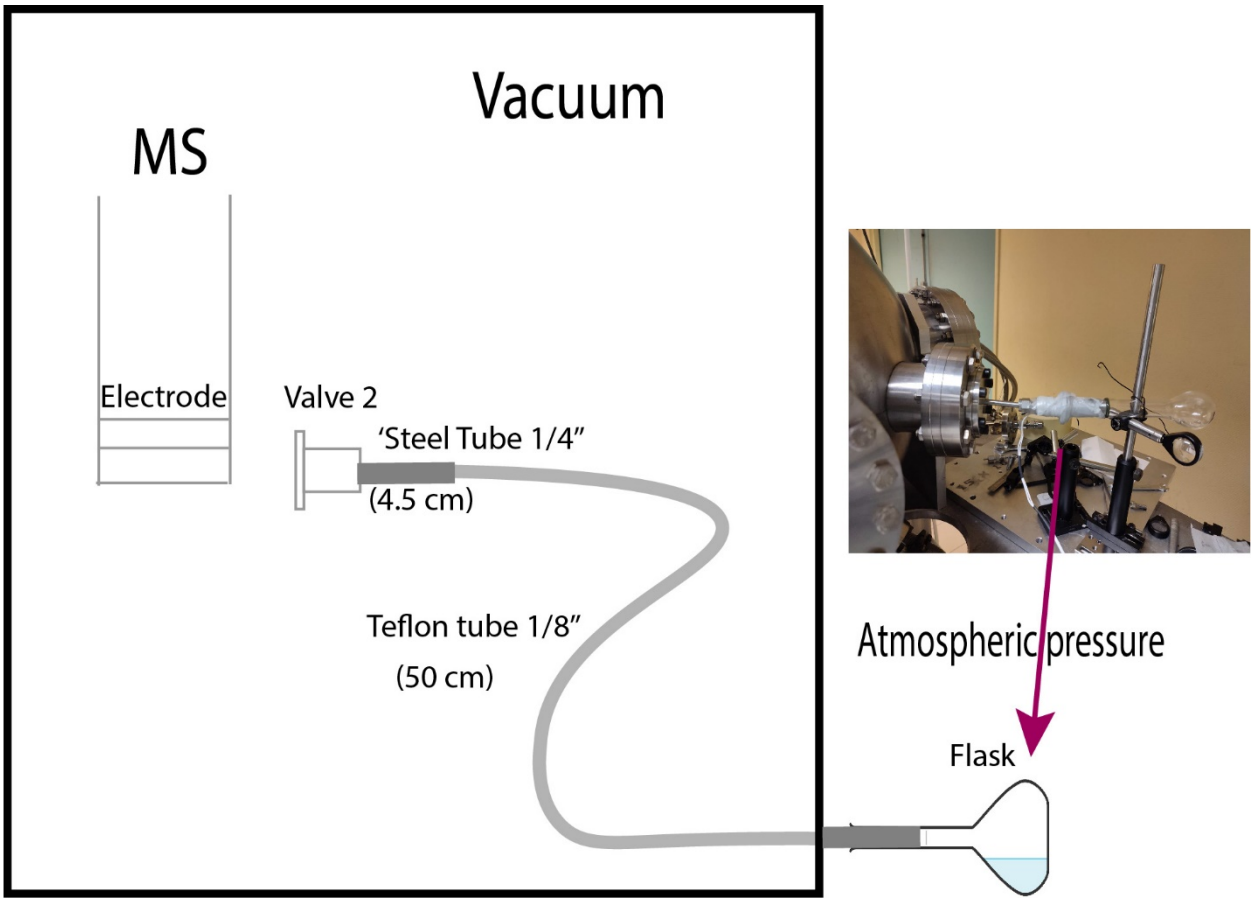

Figure 4.20 Single valve system with the valve close to the ionization region.

Results

This modification necessitated testing to verify if the new position and the configuration of the valve and tube system could effectively transfer molecules from the atmosphere to the ionization region within the vacuum chamber. Additionally, the alignment of the ionization laser needed to be confirmed.

For this purpose, a liquid sample, specifically kerosene, was used for testing. The kerosene spectrum was recorded using a single valve system with the valve ontime of 180 µs. The ionization energy was adjusted to 5.6 mJ, and the spot size was 16.5 mm², resulting in a fluence of 34.1 mJ/cm². A critical parameter in this setup was the delay between the valve opening (at the extraction zone) and ionization, set at 6.7 ms. This setup aimed to balance the operational parameters to ensure efficient molecule transfer and accurate laser alignment. The average of 1000 spectra obtained is displayed in Figure 4.21. Even if the different set of parameters makes rigorous

comparison difficult, it proves a slightly better transfer efficiency for the semi-volatile species (m/z> 125) than for configuration 1. Additionally, the signal to noise ratio is improved. For instance, the $C_9H_{12}^+$ signal is at least one order of magnitude higher, revealing the greater density of species in the ionization region in configuration 2.

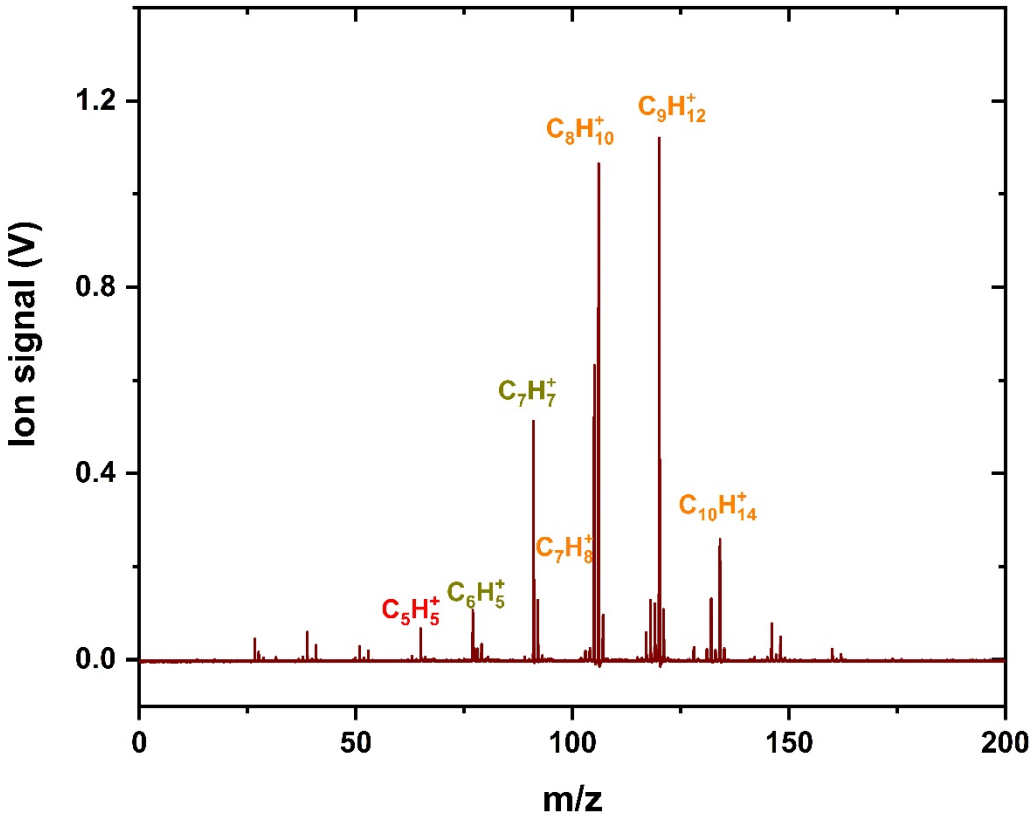

Figure 4.21 Kerosene spectrum recorded using a valve inside vacuum chamber and close to the extraction zone to test the transfer of vapor-phase analytes.

One the other hand, no significant change in the characteristic times for the establishment of a maximum ion signal in the spectrometer and its return to the background signal after the valve is switched on is observed.

4.3 Transfer of laser-desorbed analytes using a single-valve system

In the realm of two-step laser mass spectrometry, the analysis of solid samples presents unique challenges, particularly when transitioning from atmospheric pressure to a high vacuum

environment. This section explores various configurations of the sampling interface that have been tested to optimize the chemical analysis of solid samples.

In order to optimize the transfer of chemical species from the desorption zone at atmospheric pressure to the vacuum ionization zone, two challenges must be met in the light of the results obtained in the case of species already present in the gas phase as studied in previous section 4.2:

- On the one hand (condition (a)), the transfer of species from the desorption zone to the inlet of the pulsed valve must be optimized.
- On the other hand (condition (b)), we need to maximize the density of species in the extraction zone following valve opening.

In both cases, transfer line lengths are limitations that can induce losses, mainly due to adsorption of semi-volatile or non-volatile species on the walls. In section 4.2.3 with configuration 2, it seems that a valve close to the extraction region of the spectrometer enables a higher density of chemical species to be obtained in the ionization zone. In initial desorption tests on solid samples with the valve close to the spectrometer wall, signal settling time was several minutes, which does not meet our objectives of observing temporal variations at the rate of our 10 Hz Nd:YAG lasers. Pulsed valves can be mounted either on a port of the vacuum chamber, as in configuration 1, or inside the chamber, as in configuration 2. For the mass spectrometer under development, as for other mass spectrometers, the distance between the ionization zone and the outside of the enclosure is a few tens of centimeters, here around 50 cm. An interesting solution might be to use two valves at the above-mentioned positions, to define an entry lock. In the following sections, we propose to optimize conditions (a) and (b) separately with configurations similar to 1 or 2, and then to deal with the delay between opening the two valves.

Various line configurations have been designed to optimize the transfers.

In configuration 3, we begin by looking for optimal delays to satisfy condition (b) for a single valve as close as possible to the chemical species extraction zone, then we seek to optimize the transfer of species from the desorption zone with a single valve (on the chamber enclosure) close to the desorption zone. Different systems have been tested (configurations 4, 5 and 6). The current step is to optimize the delay between the two valves.

4.3.1 Synchronization scheme

Figure 4.22 is a modified version of the one used in 4.2 and presented in Figure 4.15. It shows the electronic connection to synchronize the desorption laser, the valve, and the ionization laser. In this scheme, the desorption laser is internally triggered at 10 Hz, and the Q-switch output is connected to the delay generator D1 for external trigger. D1 triggers the valve controller and delay generator D2 independently. The delay set in D1, $A = T + x$ µs, where x is the delay between desorption pulse (Q-switch) and valve opening to be able to suck all the ablated plume generated during desorption and cover the distance between the sample and valve inlet. $B = A + y$ µs, where y gives the opening pulse duration for the valve, which can be fixed to short duration of 15 µs and can be operated by valve controller (IOTA ONE). Channel A also triggers the delay generator D2, where channel values C and D are set to be $C = D - 275$ µs and $D = T + z$ µs, where C and D are connected to pulse generator to transform Heaviside's output into 15 µs wide pulse. In D2, 275 µs is the delay between output C and D, which is the delay between Flashlamp and Q-switch of the ionization laser. z is the delay between valve opening and ionization pulse.

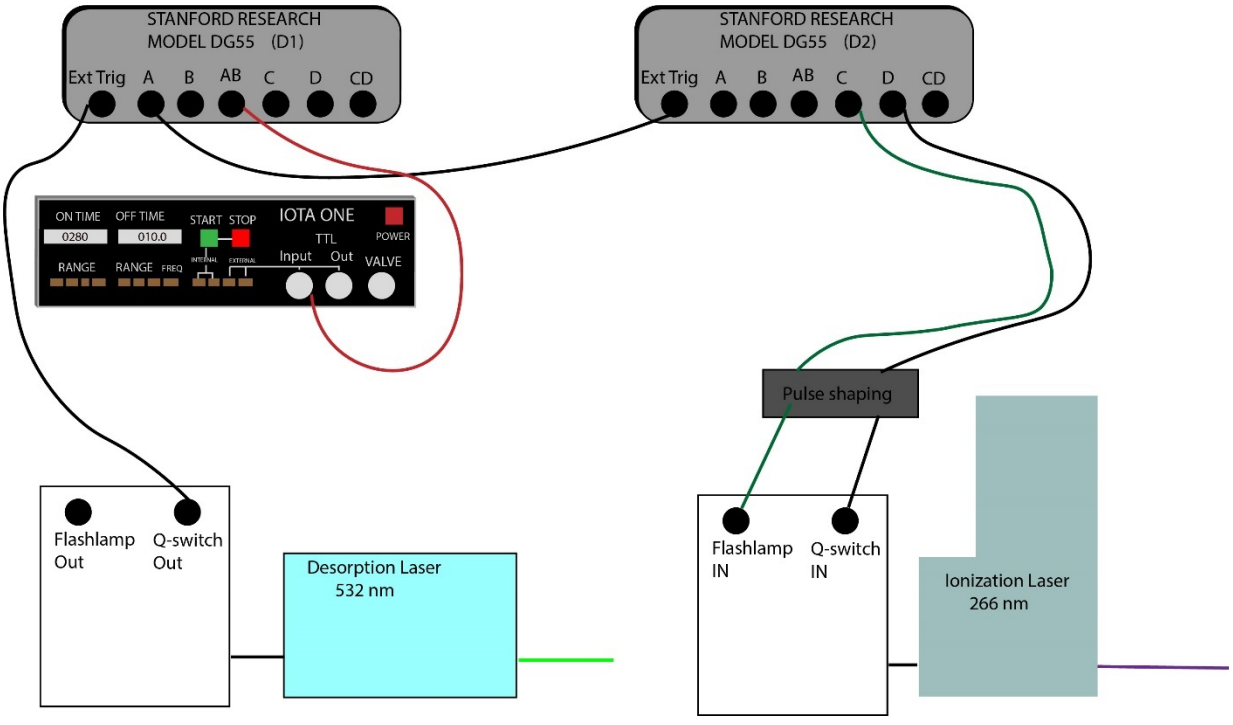

Figure 4.22 Synchronization scheme of the desorption laser, the valve and the ionization laser. Desorption laser is internally triggered at 10 Hz.

4.3.2 Configuration 3: Valve close to the ionization zone

Schematic

In the third configuration depicted in Figure 4.23, a single-valve system is employed, where the valve is positioned in close proximity to the ionization region inside the vacuum chamber. A 21 cm stainless steel tube with a 1/4-inch diameter is utilized inside the vacuum chamber. This setup minimizes the distance between the sample and the ionization point, thereby reducing the travel time of the analytes and potentially decreasing condensation. The sample inlet tube is tilted and aligned perpendicularly to the sample surface to efficiently sample the ablated analytes. Externally, this sampling inlet tube measures 13 cm in length and has a 1/8-inch diameter. Additionally, a secondary tube is attached to the top of the inlet tube, which connects to a primary pump to facilitate the transfer of analytes. The gap between the valve nozzle and the center of the extraction region is 4 cm. The valve's on-time is set to 250 µs, operating at a frequency of 10 Hz. This configuration aims to optimize the transfer and ionization of analytes by ensuring minimal travel distance and efficient sampling.

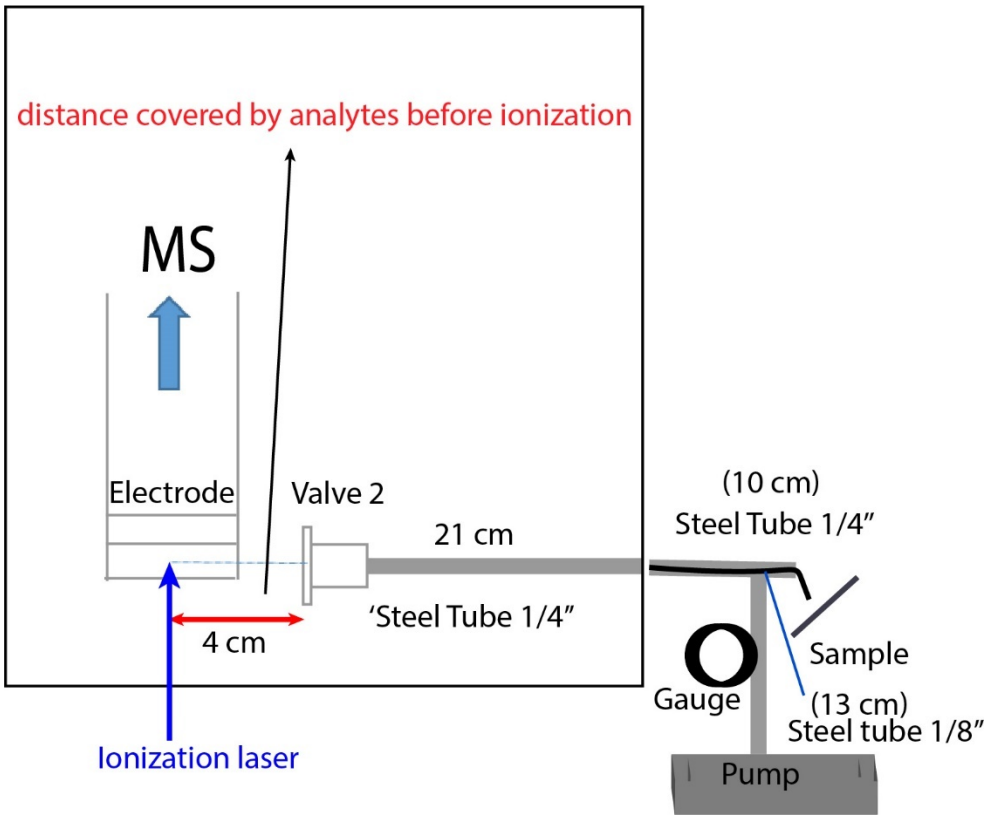

Figure 4.23 Schematic of the single valve configuration used to optimize the delay between the valve opening and the ionization laser pulse. The distance between the valve nozzle and the center of the extraction electrodes is 4 cm.

Results

Figure 4.24 shows the average of 1000 spectra recorded for a delay between the valve opening and the ionization laser pulse of 700 μs. Although the S/N ratio is satisfactory, a comparison of the naphthalene (desorbed) and nitrogen (aspirated) peaks demonstrates the poor transfer efficiency of this configuration. This is all the more remarkable as the ionization yield is a priori much better for naphthalene than for nitrogen.

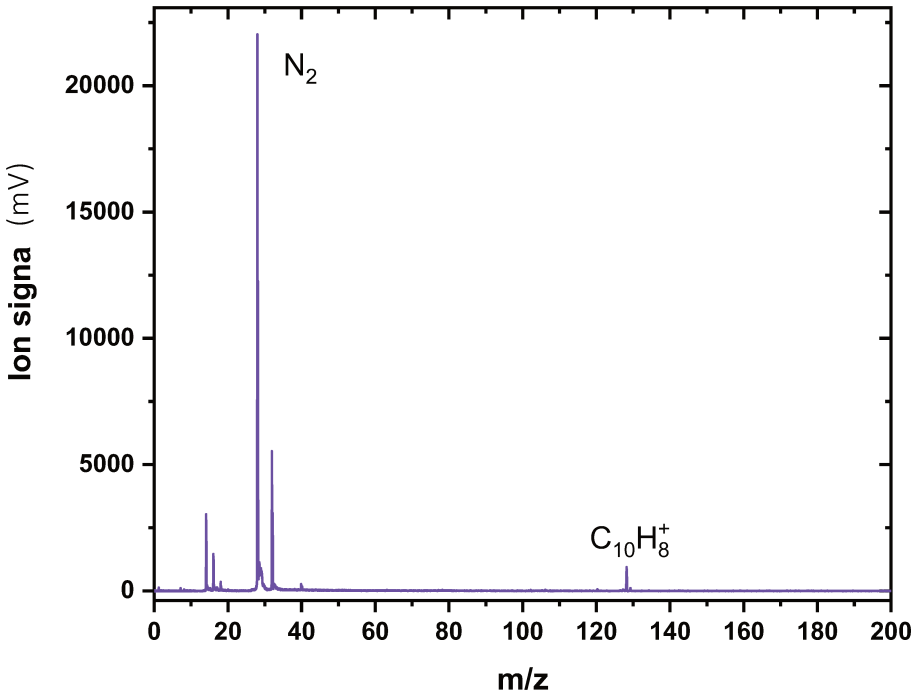

Figure 4.24 Mass spectrum of naphthalene at 700 µs delay between valve opening and ionization.

The velocity distribution was recorded for naphthalene (and other various molecules) by varying the delay between the opening of the valve in front of the ionization region and the ionization laser pulse. The signal intensity normalized to 1 is depicted in Figure 4.25 for molecular nitrogen (N_2, *m/z* 28) and naphthalene ($C_{10}H_8$, *m/z* 128). In both cases, the profiles show a similar normal Maxwell-Boltzman distribution, characterized by a sharp tail for the shorter delays and a smoother tail at longer delays. The optimum delay found is about 600 µs. corresponds to a most likely speed of about 70 m/s This value corresponds to a subsonic jet. It is given as an indication only, as it is highly dependent on several parameters (in particular: pressures before and after the valve, opening time and valve diameter).

On the other hand, the width of the distributions (around 500 µs, of the same order of magnitude as the valve opening time) is encouraging in that it guarantees the absence of pollution in the chamber after each opening.

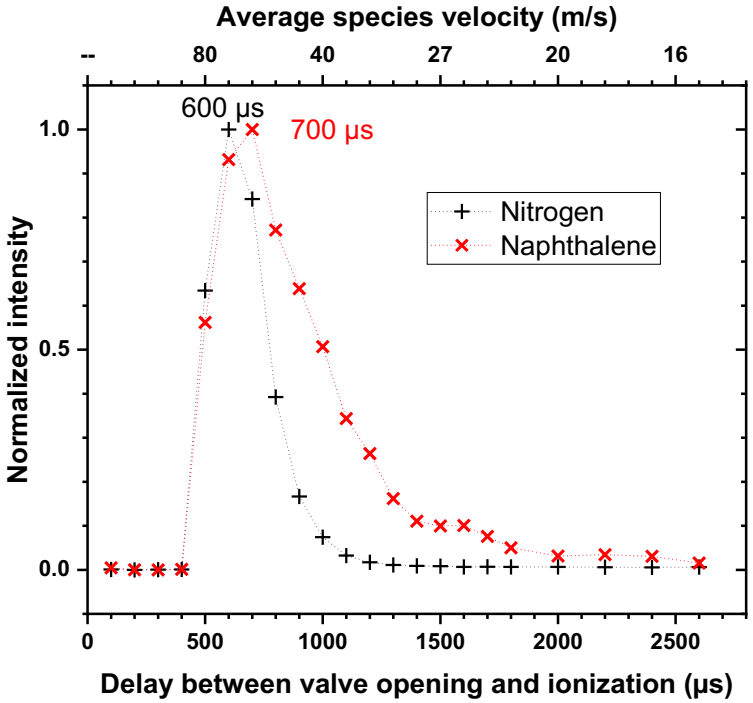

Figure 4.25 Evolution of the naphthalene and molecular nitrogen signals in the mass spectra as a function of the delay between the opening of the pulsed valve in the analysis chamber and the ionization laser trigger. The times required to obtain the optimal ion signal are indicated.

4.3.3 Configuration 4: Valve on a spectrometer port – Sample in a dedicated chamber

Schematic

The first configuration for analyzing solid samples in this study involved the design of a dedicated sample chamber at atmospheric pressure. This chamber was intricately linked to the vacuum chamber through a Teflon tube, accompanied by a solenoid valve, ensuring a controlled pathway for the molecules. To aid in the transfer of ablated molecules from the sample chamber to the vacuum chamber, a nitrogen inlet was positioned on one side of the sample chamber. This setup facilitated the efficient movement of molecules through the Teflon tube.

Once inside the vacuum chamber, the setup featured another segment of Teflon tubing, extending from the valve to the extraction plates. It is in this carefully controlled vacuum environment that a Nd:YAG laser with a wavelength of 266 nm was employed. This laser played a crucial role in the ionization process, effectively ionizing the desorbed molecules from the solid samples.

The schematic on the right of Figure 4.26 illustrates the configuration and orientation of the sample, desorption laser, nitrogen inlet, and plume extraction system. This diagram indicates that the desorption laser is positioned perpendicularly to the sample surface. Adjacent to the sample, the nitrogen inlet is situated in close proximity and aligned parallel to the sample's surface. Additionally, another tube, measuring 1/4-inch in diameter, is placed parallel and in close proximity to the sample. This tube serves as a conduit, linking the sample area to the vacuum chamber, facilitating the transfer of molecules.

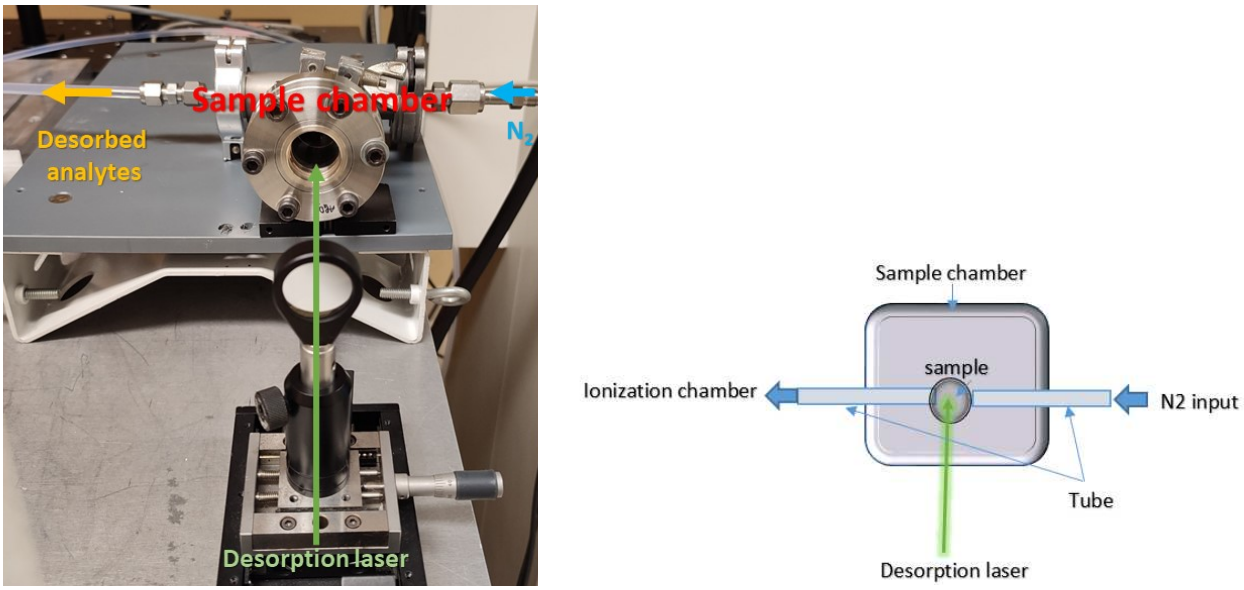

Figure 4.26 Left: Picture of the first sample chamber tested for the desorption from solid sample with the introduction of nitrogen gas. Right: Schematic showing the sample chamber at atmospheric pressure and the nitrogen inlet tube connected close to the sample to facilitate the transfer of ablated species towards the vacuum chamber.

Results

An initial test was conducted using a pyrene pellet in the sample chamber, following the configuration described above. For this experiment, pyrene was selected due to its ease of ablation, achieved by heating with a Nd:YAG 532 nm laser (desorption energy of 64 µJ) and a Nd:YAG 266 nm laser for ionization (ionization energy of 3.27 mJ).

In the resulting spectrum, shown in Figure 4.27, a pyrene peak (202 *m/z*) was successfully recorded. However, the peak intensity was relatively weak, and there were also signals of kerosene,

indicating the presence of kerosene molecules condensed within the tube and valve, which acted as contaminants during the experiment with pyrene. This occurrence highlighted a dual aspect of the results: on one side, the presence of the pyrene peak confirmed that transfer of molecules from a solid sample into vacuum was feasible, but on the other side, it also pointed to the inadequacy of the current configuration and the need for significant improvements. The presence of unintended kerosene signals suggests that the system, while capable in certain aspects, requires further refinement to prevent contamination and enhance overall efficiency.

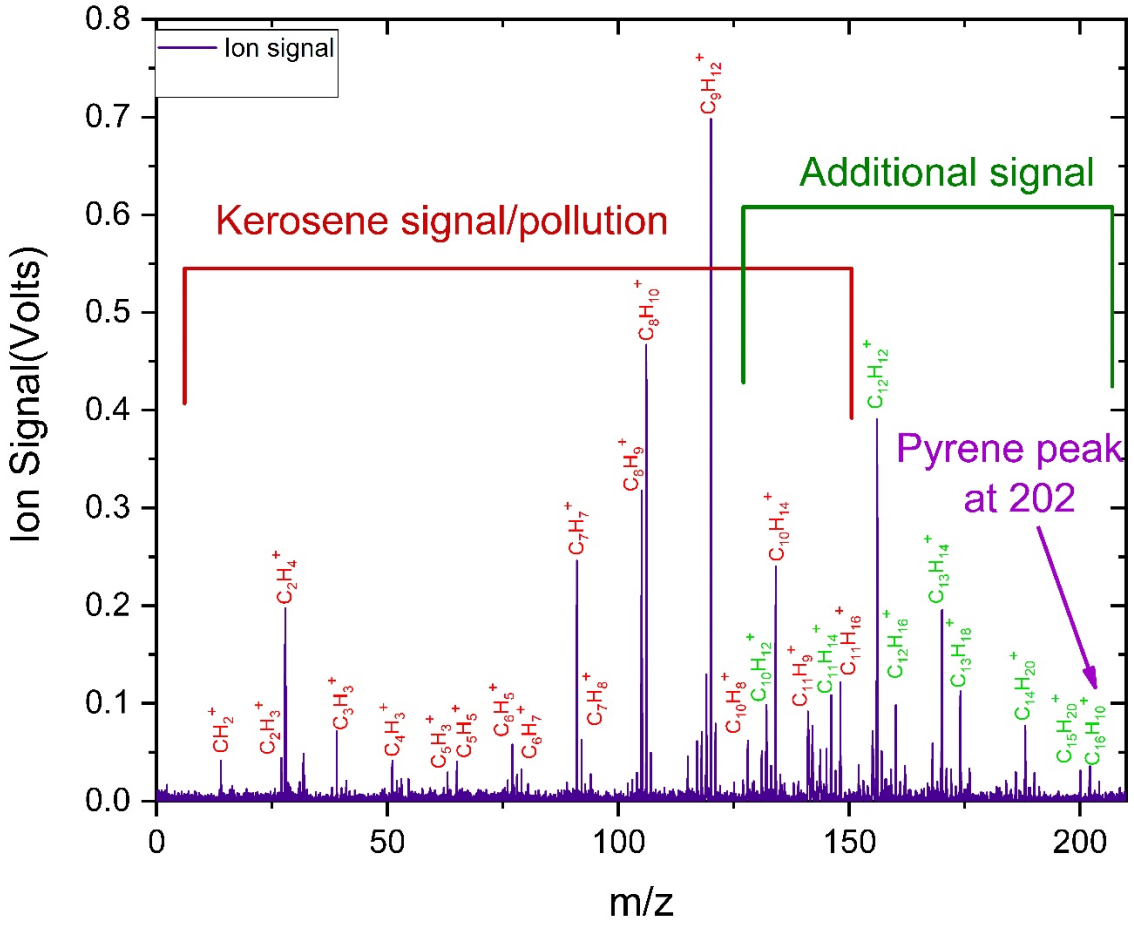

Figure 4.27 Preliminary test for solid sample using pyrene palette inside sample chamber at atmospheric pressure, confirming the transfer of pyrene, average of 1000 acquisitions.

4.3.4 Configuration 5: Valve on a spectrometer port - Plume-to-valve drive system.

Schematic

In this modified setup, one valve is connected outside the vacuum chamber (valve 1, which links to one of the vacuum chamber's external ports). In this configuration a Teflon tube of 47.3 cm of 1/8 inch diameter is connected from valve to the extraction zone (which is under vacuum). A 1/8-inch steel tube is bent and is connected to the valve at atmospheric pressure, which inlets the analytes from the sample to the valve. Additionally, a primary pump is installed between the valve and sample. A 1/4-inch steel tube is connected on top of the 1/8-inch steel tube, with the purpose of decreasing the pressure inside the tube. In this configuration the inlet tube is bent, which makes the inlet perpendicular to the sample surface. This change aligns with the direction of the ablated plume, which is typically normal to the sample surface. This facilitates the ablation of molecules directly beneath the aspiration inlet, achieved by performing the desorption process right under the inlet. The schematic of this configuration is shown in Figure 4.28.

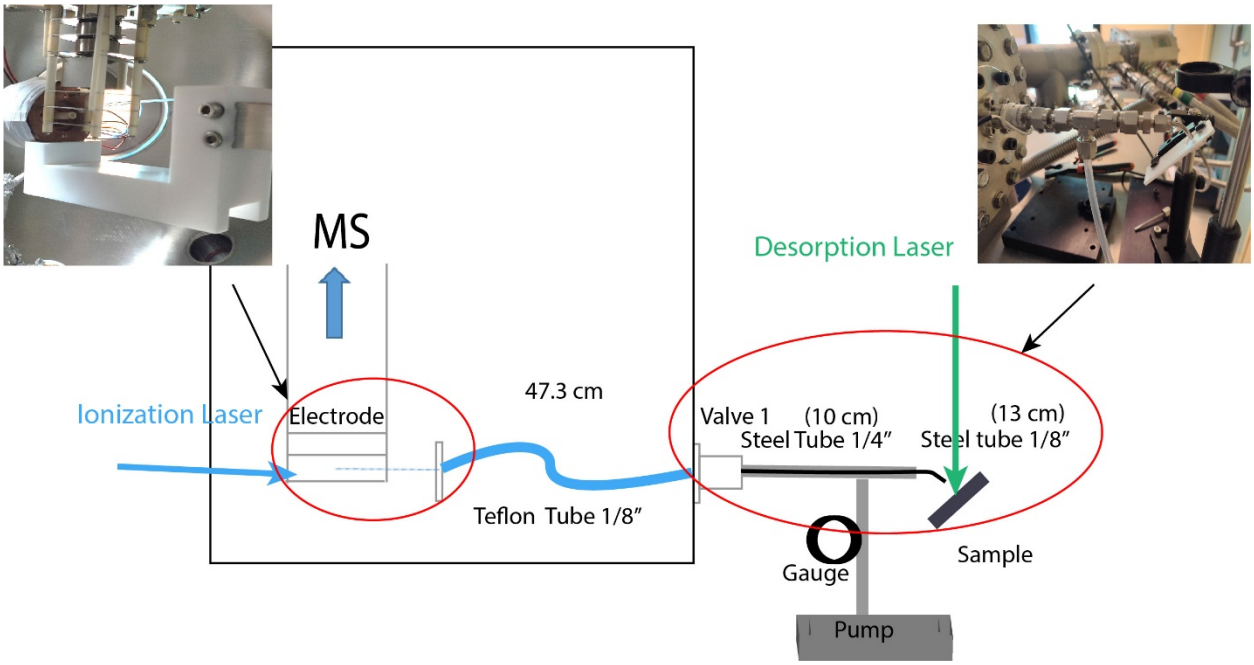

Figure 4.28 Schematic of one valve system (valve 1, outside the vacuum chamber) and tilted capillary which is normal to the sample surface, with picture of extraction plates and the sampling interface outside the chamber.

Results

This adjustment of tilting the capillary normal to the sample surface enhanced the signal, as evidenced by the results obtained from a naphthalene pellet, detailed Figure 4.29. Key parameters for this setup included synchronizing the ionization laser with a 16 ms delay following valve 1 activation. The valve's ontime was set at 200 µs, and the ionization energy was adjusted to 4.6 mJ. This configuration proved effective in improving signal clarity and strength for naphthalene analysis. However, the signal decreases few seconds after the laser shots, suggesting again important condensation inside the tube and valve.

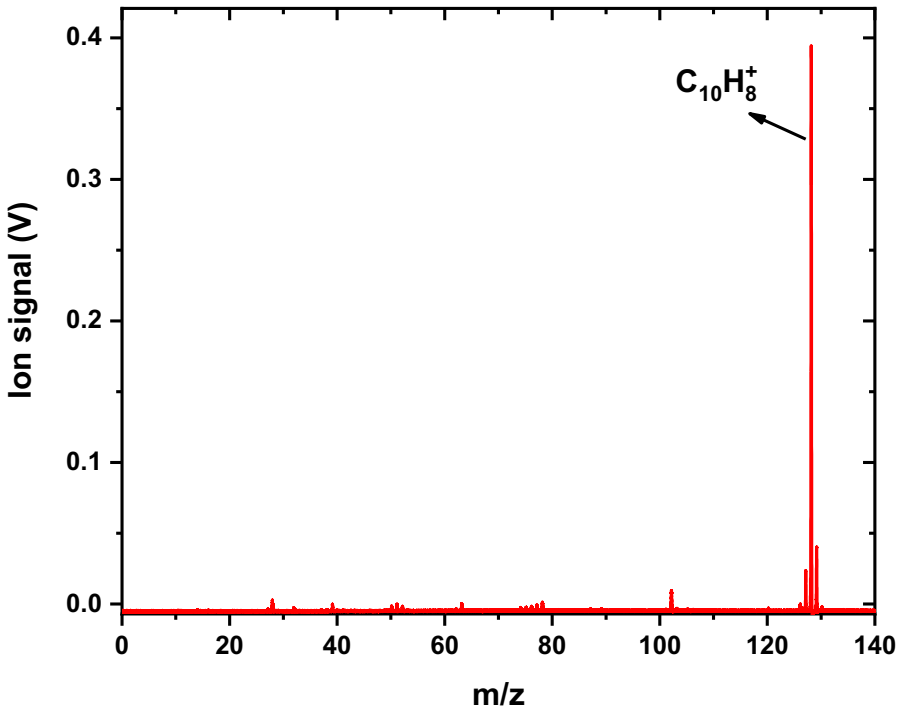

Figure 4.29 Naphthalene spectrum recorded at ionization energy of 4.6 mJ, ontime of the valve 200 µs, and average of 1000 acquisitions.

4.3.5 Configuration 6: Valve on a spectrometer port - Sample as close as possible to the valve

Schematic

The latest iteration of the experimental setup for mass spectrometry has seen significant modifications from its previous version, enhancing both its efficiency and effectiveness. A critical update in this new design is repositioning the tube within the chamber, now situated closer to the

extraction plates. In this configuration one valve (valve 1, which is connected to the vacuum chamber port) is connected and there is no valve inside the chamber.

In this streamlined setup, the sample is positioned close to the valve, allowing the directly ablated plume to enter the valve and be swiftly transported to the tube within the vacuum. This tube then channels the plume towards the ionization zone. The transfer tube inside the chamber is 23 cm stainless steel tube with diameter1/4 -inch. The sample is vertically aligned in front of the valve, ensuring that its surface is perpendicular to the valve inlet. This orientation capitalizes on the vertical rise of the desorption plume from the sample's surface, thus enhancing the injection of species for analysis.

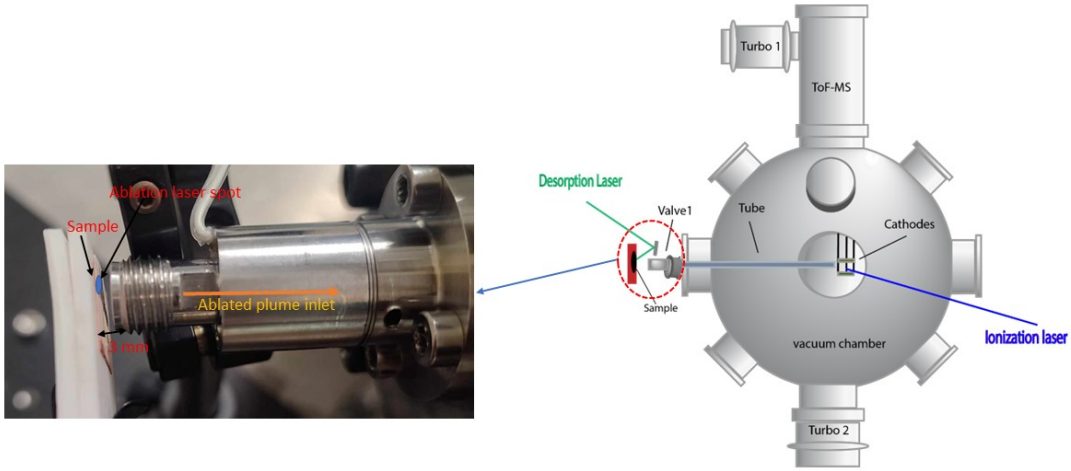

Figure 4.30 Scheme and picture of the valve and sample showing the ablation spot and distance between valve and sample.

Additionally, adjustments have been made to the desorption laser's optical path. It is now aligned at a nearly grazing angle relative to the sample, as depicted in Figure 4.30. The sample is also mounted on a translation stage, which serves two critical functions: it allows precise laser focusing on the sample surface and provides continuous access to fresh sample areas. This feature is vital for potential chemical mapping of the sample's surface, enabling a detailed and comprehensive analysis.

Heating system

The initial studies on aromatic compounds revealed that for larger, less volatile species (molecular weight > 200), heating the transfer line elements is crucial for successful observation. This heating

is necessary both to ensure the detection of these larger molecules and to prevent contamination from more volatile species (molecular weight < 200).

To address this, a two-zone heating line, designed by DIFATEC, was integrated into the system. This heating system comprises three components:

1. A 160W, 300mm cold-formable heating cartridge, which makes direct contact with the internal transfer tube of the spectrometer. This component's temperature is regulated by feedback from a type J thermocouple.
2. A 75W heating cable wrapped in fiberglass insulation is used for the line outside the spectrometer. The temperature here is monitored using a Pt100 platinum probe.
3. The entire heating system is controlled by a dual-zone regulation box (see Figure 4.31), the functionality of which is detailed in Figure 4.32.

Currently, the external part of the system is limited to a maximum temperature of 70°C. This limitation is in place to prevent damage to the valve's poppet. While this temperature cap restricts some capabilities, it also has a positive effect on reducing residual contamination from more volatile substances.

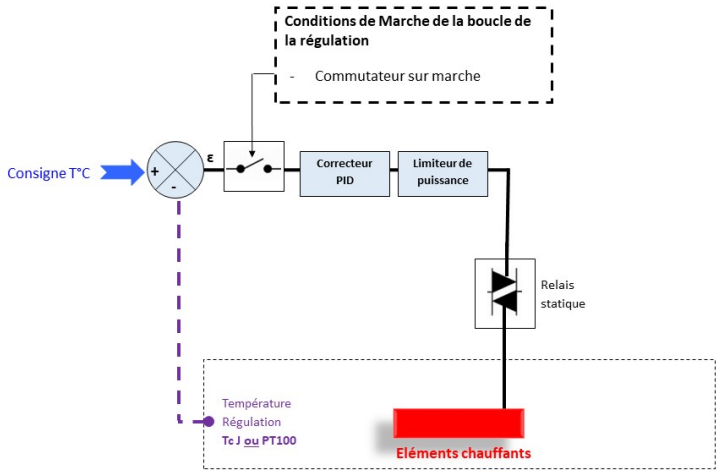

Figure 4.31 Principal diagram of operation of one or other of the heating elements used for temperature regulation of the transfer line.

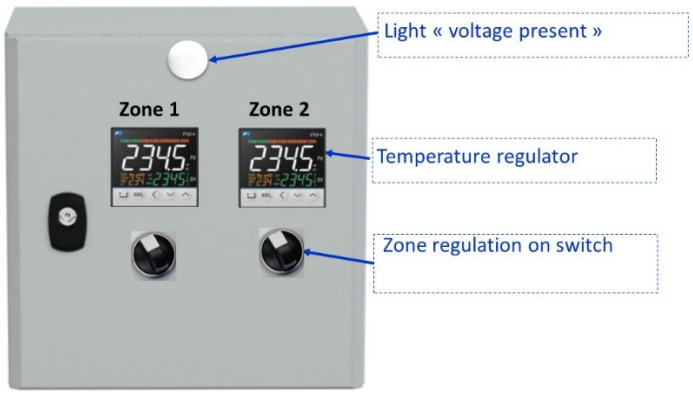

Figure 4.32 Dual zone temperature regulation box.

Results

The optimal delay between the laser desorption pulse and the valve opening (outside the chamber) was probed using the setup described in Figure 4.30. The distance between the valve and the sample was kept at 3 mm, with the sample surface oriented normal to the valve inlet. The curves presented in Figure 4.33 show the signal intensity for phenanthrene and pyrene pellets when varying the delay between valve opening and desorption (while keeping the delay between valve and ionization constant at 11.5 ms). These two molecules show two different optimal delays (450 μs, and 350 μs in case of phenanthrene and pyrene respectively) which can for instance be attributed to difference in the interaction between the laser pulses and the samples.

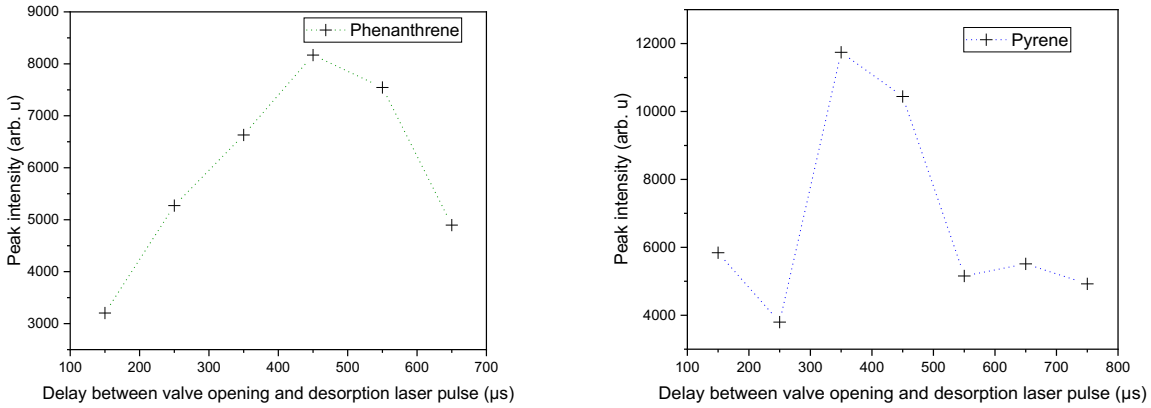

Figure 4.33 Evolution of the phenanthrene and pyrene signals in the mass spectra as a function of the delay between the opening of the pulsed valve and the desorption laser trigger.

The effectiveness of this configuration was tested using phenanthrene and pyrene pellets. The results, displayed in Figure 4.34, showed spectra for phenanthrene (left) and pyrene (right), with a delay of 11.5 ms between valve 1 and ionization laser pulse, a valve ontime of 250 µs, an ionization energy of 1.5 mJ, and a desorption energy of 1.4 mJ. These findings suggest that the single valve system is effective in transferring the ablates analytes to vacuum, by placing the sample close to the valve, and using small tube for transfer line.

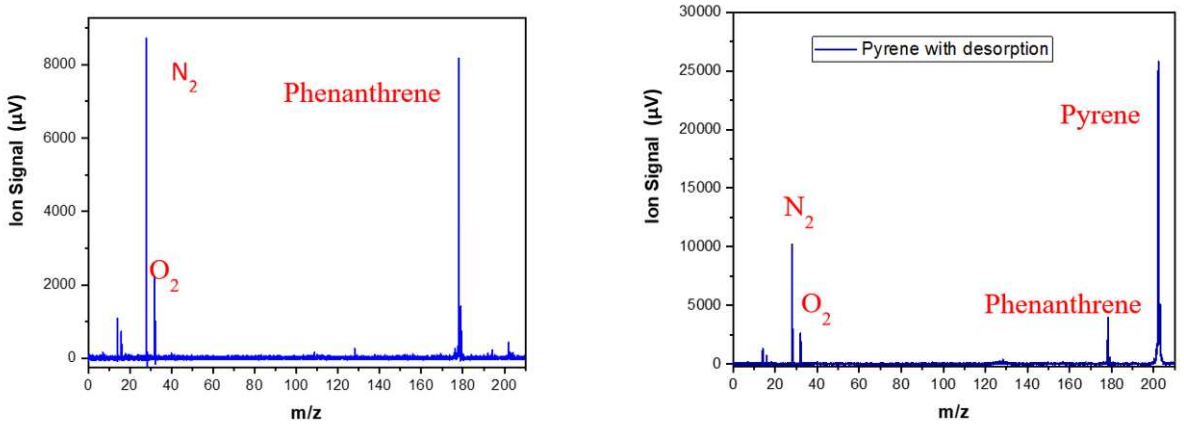

Figure 4.34 Left Phenanthrene spectrum and right Pyrene spectrum recorded using single valve (valve 1) system.

This configuration, which includes a heating system, effectively reduces condensation inside the tube and valve, resulting in improved transfer of PAH molecules, while distributions shown in Figure 4.33 suggest a limited risk of pollution of the spectrometer after laser pulses. To evaluate this setup with complex molecules, plastic samples were analyzed. The outcomes of these tests are discussed in detail in Chapter 5, Section 5.5.

4.4 Under development: Transfer of laser-desorbed analytes using a two-valve system

4.4.1 Synchronization scheme

The schematic depicted in Figure 4.35 shows the electronic connections used to synchronize the desorption laser, the two valves and the ionization laser. Other configurations could have been used.

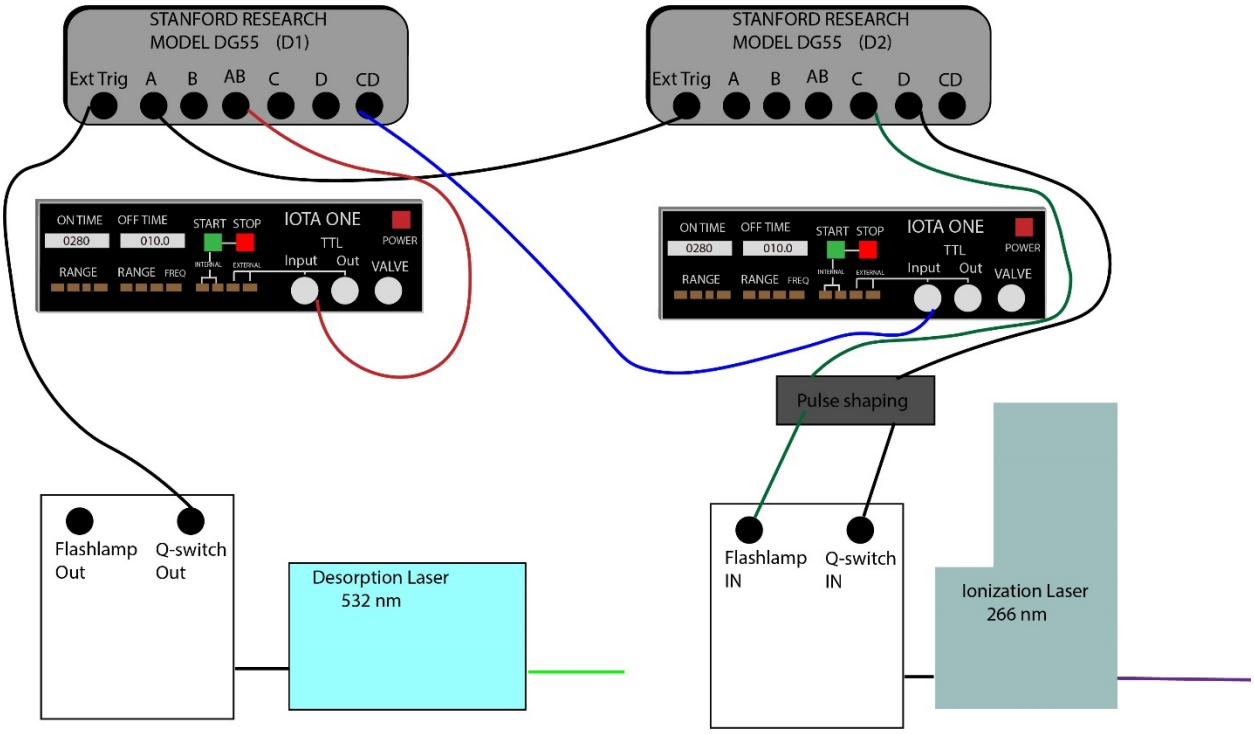

Figure 4.35 Cable schematics for synchronization of the desorption laser, the 2 valves and the ionization laser. Desorption laser is internally triggered.

To synchronize the 4 devices using two delay generators D1 and D2 (with high impedance for all channels), previous connections were modified. The desorption laser (Minilite) was internally triggered. Its Q-Switch trigger out or Flash lamp trigger out is connected to the external trigger input of D1. The former enables low jitter between the desorption laser and the other elements in the time sequence, while the latter allows us to open the valve up to 155 µs before the desorption step if we want to ensure suction during the development of the desorption plume. D1 is triggering both valve controller independently and the delay generator D2. D2 triggers the ionization laser's flash lamps and Q-switch via a pulse shaper that transforms Heaviside's C and D outputs into 15 µs wide pulses. The ontimes of the valves can be either controlled by the pulse width of D1's AB and CD outputs or by the IOTA ONE controllers if AB and CD pulse widths are fixed at a lower value (15 µs). The various delays are specified in Table 4.3 and in the time sequence of Figure 4.36. The 275 µs delay between output C and D of D2 corresponds to the delay between the Flash lamps and the Q-Switch of the ionization laser. It can be changed to adjust the output energy of the laser pulses. The 80 ns measured between the trigger signal of the second valve and the

photodiode signal collected at the ionization beam entry window in the spectrometer corresponds to additional electronic delays, as well as to the propagation time of the laser beam.

Table 4.3 Time delays applied to two delay generators to synchronize all the devices.

Delay generator **D1** (externally triggered)	$A = T + x\ \mu s$
	$B = A + y\ \mu s$
	$C = A + z\ ms$
	$D = C + u\ ms$
Delay generator **D2** (externally triggered)	$C = D - 275\ \mu s$
	$D = T + v\ ms$

The synchronization process in this context is influenced by the travel time of molecule depending on molecular mass, configuration of the inlet and capillary dimension and length, and also on the ontime of the valve. The outcomes of the different configurations tested, and their synchronization will be elaborated upon in the following chapter. This upcoming chapter aims to provide a detailed analysis and results of different configuration setups, showcasing the impact of synchronization in optimizing the overall performance of the system

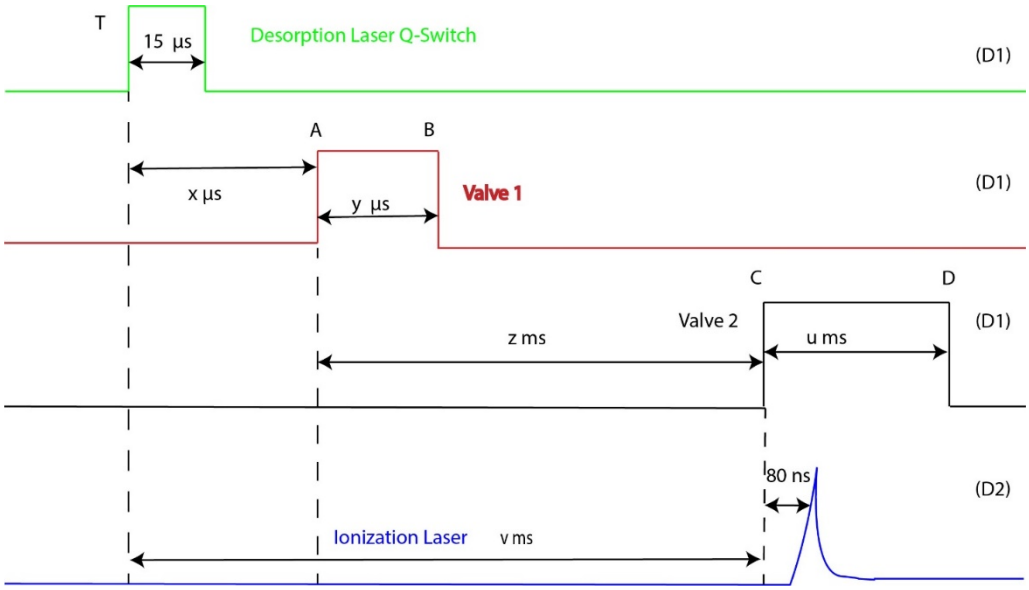

Figure 4.36 Schematic diagram of synchronization of all the elements of the transfer line with the associated characteristic times. The time T corresponds to the triggering of the desorption laser.

4.4.2 Configuration 7: Two valve system (long and bent capillary)

Schematic

Figure 4.37 depicts a setup where the desorption of samples occurs directly under ambient conditions, without the use of a sample chamber. In this configuration, a two-valve system is employed to create a differential pressure within the transport tube, aiding in the efficient movement of molecules.

One of the valves is located inside the vacuum chamber, positioned near the extraction plate, while the other valve is situated outside the vacuum chamber. These valves are connected by a 1/4-inch stainless steel tube that measures 59 cm in length. Outside vacuum chamber this valve is connected to 1/8-inch tube of 7.2 cm length. The end of this tube is bent and positioned in close proximity to the sample. The orientation of the tube and sample is perpendicular to each other, aligning with the direction of the plume that emanates normally from the sample surface. The desorption laser was focused 45^0 to the sample surface under the sample inlet.

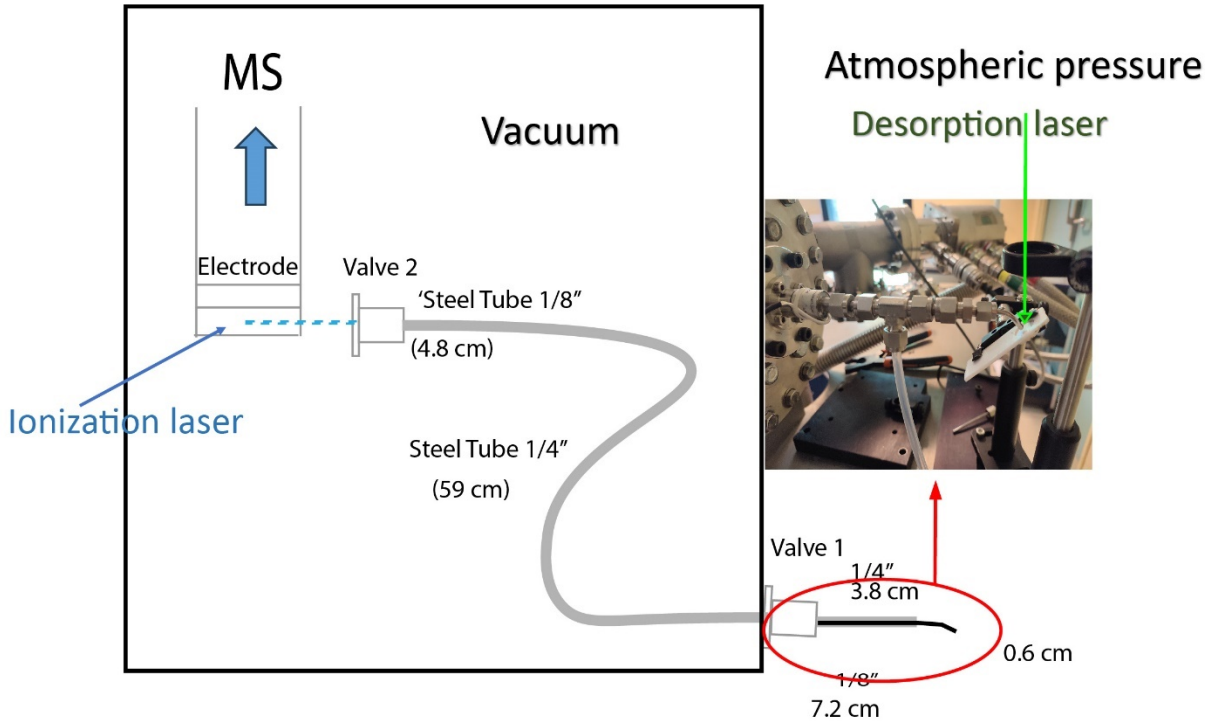

Figure 4.37 Schematic of two valve system with bent inlet tube close to the sample.

Results

Using an anthracene pellet, an intense anthracene signal was successfully recorded, affirming the compound's ease of ablation. The experiment detailed above had a 1 ms delay between valve 1 and valve 2, and a 6.7 ms delay between valve 2 and the ionization laser (this delay needs to be optimized), with the desorption laser not being synchronized. The observed spectrum, shown in Figure 4.38, revealed a prominent anthracene peak. This result suggests that the configuration, which involved reducing the length of the transfer tube, was effective in transferring molecules into the ionization region, subsequently enhancing the signal strength. This finding validates the modifications made to the system's design in improving molecular transfer efficiency.

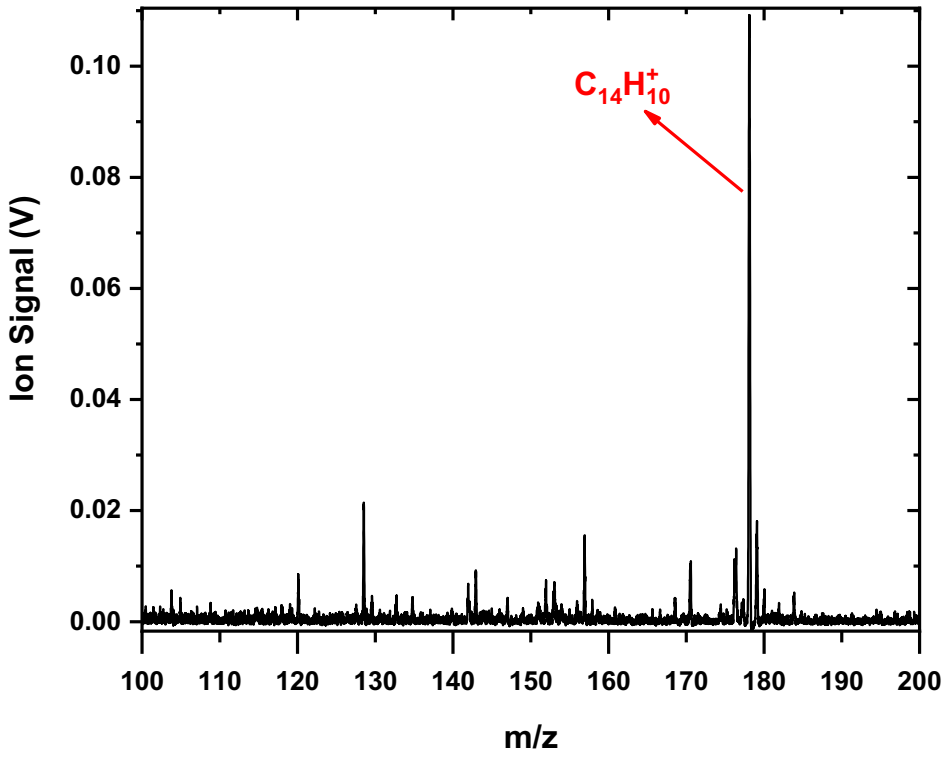

Figure 4.38 Anthracene signal recorded using anthracene pellet at ionization energy of 4.91 mJ.and ionization energy of 42.7 µJ.

4.4.3 Configuration 8: Two valve system with short and straight capillary

Schematic

In the configuration depicted in Figure 4.39, modifications were made to enhance the efficiency of molecule transfer. The key involved repositioning the sampling interface, which allowed for the use of a straight stainless-steel tube, 1/8 inch in diameter and 21 cm in length, inside the vacuum

chamber. This adjustment eliminated the need for a bent tube and reduced its overall length, aiding in the reduction of molecule condensation within the tube and improving transfer efficiency.

In this revised setup, a two-valve system was employed to establish a differential pressure environment. The valve located outside the vacuum chamber was connected to a ¼ inch capillary, which was angled to facilitate easier alignment of the desorption laser with the sample surface (see Figure 4.39). This orientation also ensured that the sample surface was perpendicular to the sampling inlet, optimizing the efficiency of the desorption process.

To further enhance the system's performance, a primary pump was integrated between the valve and the sample inlet. This pump could be activated or deactivated as needed, depending on the specific requirements of each test. This flexible arrangement provided good control over the sample handling and desorption process, contributing to the overall effectiveness of the mass spectrometry analysis.

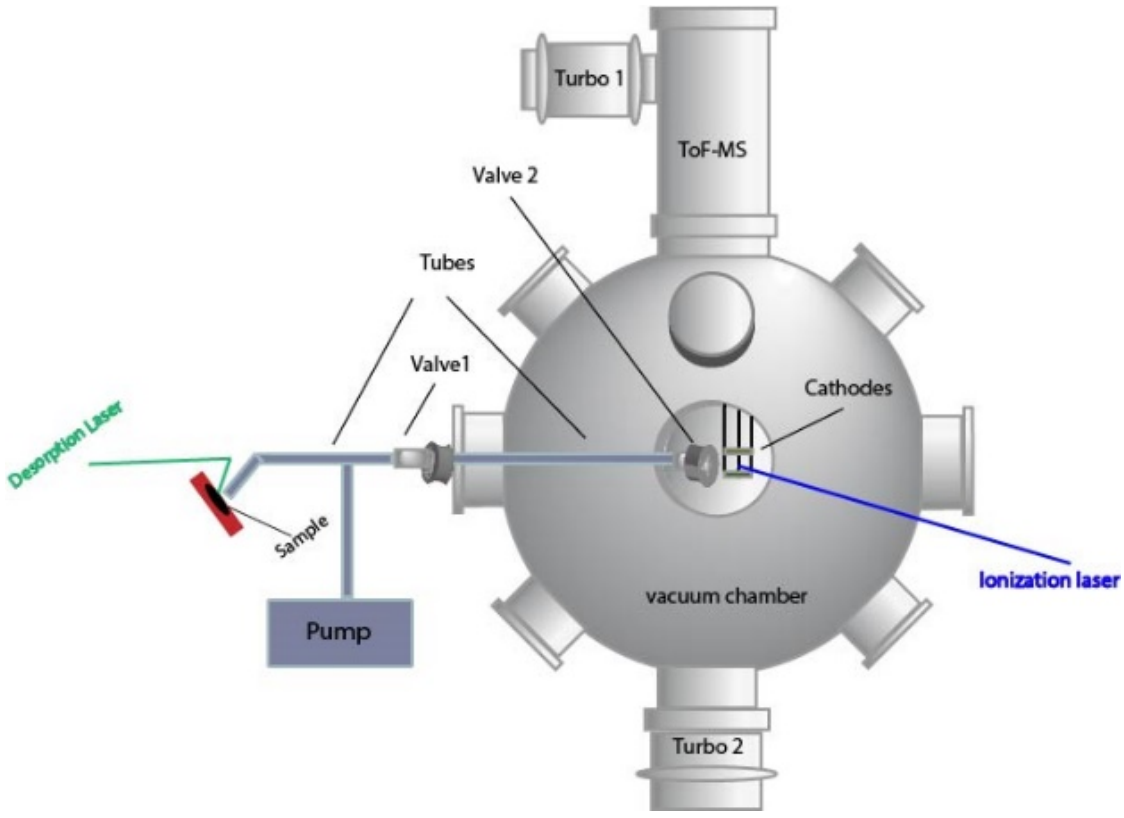

Figure 4.39 Schematic of two valve system with short and straight capillary.

Results

To evaluate the efficiency of molecule transfer and ionization, a naphthalene palette was used. The recorded spectrum, shown in Figure 4.40, was obtained using a two-valve system with specific time delays: 150 µs between valve 1 and desorption, 20 ms between valves 1 and 2, and 3 ms between valve 2 and ionization. Valve 1 opened for 300 µs, and valve 2 for 80 ms, creating a low-

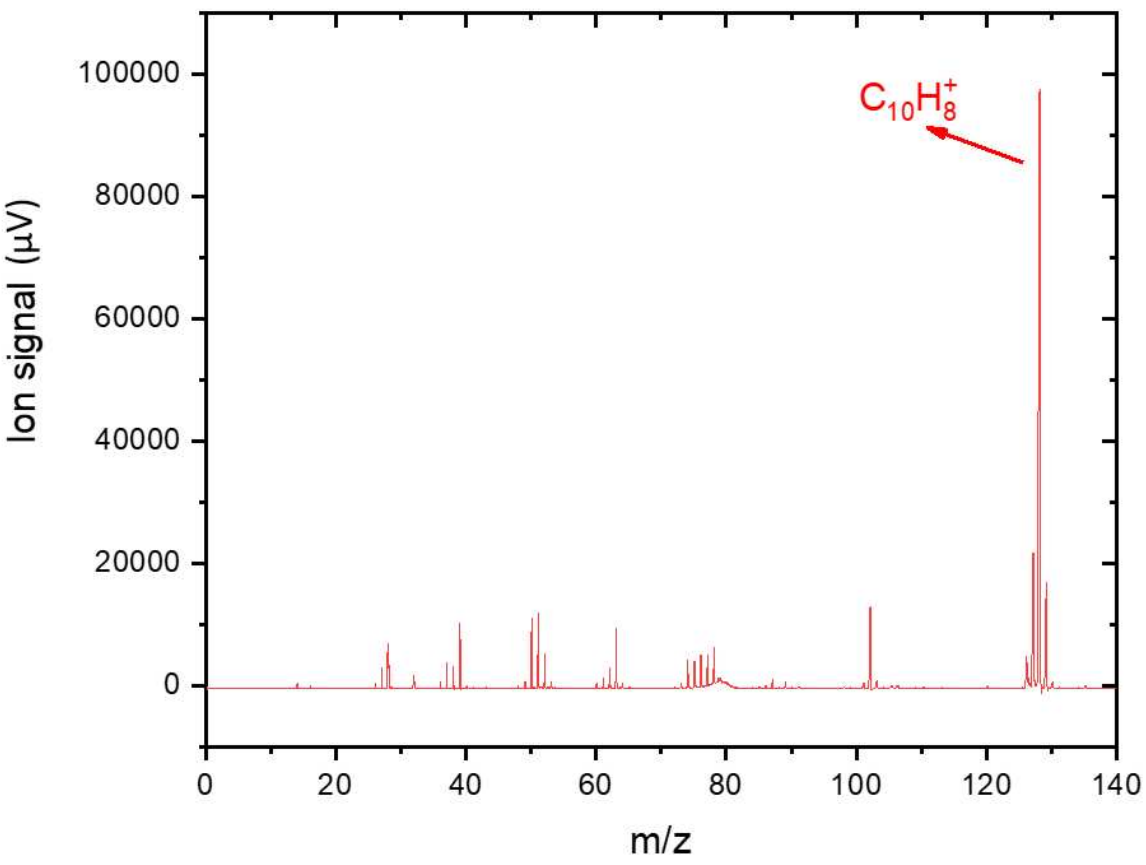

Figure 4.40 Naphthalene spectrum recorded with short and straight tube inside the chamber using two valve system averaged over 2000 acquisitions.These preliminary results are promising, but will require both thermal insulation of the transfer line from the flange which it is mounted, and the use of all-metal valves to achieve more efficient heating and thus reduce the risk of condensation. This point will be discussed in more detail in Chapter VI Conclusion and Perspectives.

Chapter 5 Optical and MS analysis of plastics

This chapter concentrates on the composition analyses of various industrial plastics using three different techniques: Raman spectroscopy, FTIR, and mass spectrometry. This work is part of the EffPhob ANR project ("Effluents d'un procédé de photodégradation de retardateurs de flamme bromés dans les DEEE", 2021-2025, PI: U. Maschke, co-PI for the PhLAM laboratory: M. Ziskind). Besides, the analysis of plastic samples, especially micro-plastics, is of strategic interest for the development of analytical instruments at industrial partner HORIBA.

In the frame of the ANR project, three distinct industrial plastics were examined: ABS (Acrylonitrile Butadiene Styrene), PC (Polycarbonate), and HIPS (High Impact Polystyrene), containing or not 10%wt of DBDE flame retardant. Identical plastics samples containing the flame retardant but subjected to a debromination protocol using UV-vis irradiation [91], [92], [93] were also available. For each of the three techniques, spectra of commercial DBDE were recorded as reference and experimental conditions were tuned to be able to detect DBDE and/or associated bromine signatures. The various plastics – pristine or containing DBDE, before and after irradiation - were analyzed with the same defined protocol to highlight the efficiency of the debromination.

In this chapter, the problematic of flame retardant is presented and followed by a detailed analysis using the 3 techniques. In the case of mass spectrometry, this study is also a first test of the atmospheric pressure interface developed in Chapter 4.

5.1 Flame retardants in plastics

Brominated Flame Retardants (BFRs) have become integral in modern manufacturing due to their effectiveness in reducing the flammability of a wide range of materials [94]. Bromine binds with high energy radicals, especially OH and H and thus reduces the fire energy and slows the burning [95]. These chemical compounds are extensively used in various industries, notably in textiles, building materials [96], insulation, automotive components, and electrical and electronic equipment (EEE) [97], [98]. The utility of BFRs stems from their ability to significantly delay the onset of fires, thereby enhancing safety standards and minimizing fire-related hazards.

Despite their apparent benefits, BFRs have been increasingly scrutinized due to their potential environmental and health impacts. Studies have shown that certain BFRs, particularly Polybrominated Diphenyl Ethers (PBDEs), can persist in the environment and bioaccumulate in wildlife and humans. This persistence raises significant concerns as these compounds have been linked to adverse health effects. Research indicates that PBDEs might disrupt endocrine and thyroid functions, impact neurobehavioral development, and cause morphological changes in liver and kidney tissues [99]. The global detection of these compounds in various biological and non-biological matrices such as soil [97], water bodies [100], air, and even in agricultural crops, fish, and birds, underscores the pervasive nature of this issue [101].

In response to these concerns, regulatory bodies worldwide have begun to restrict or ban the production and use of certain BFRs [102], recognizing them as persistent organic pollutants. However, a significant challenge remains in addressing the BFRs already present in countless products currently in use or in waste streams. This challenge is particularly pronounced in the context of Waste Electrical and Electronic Equipment (WEEE), where plastics containing BFRs are abundant. The recycling of these plastics poses a unique challenge, as it is essential to remove or neutralize the BFRs to prevent further environmental contamination.

This backdrop sets the stage for our research, which aims to explore the efficiency of methods for the debromination of BFRs in plastics [103]. Specifically, our study focuses on the use of UV-visible irradiation [91], [92], [93] as a promising approach to break down BFRs, potentially facilitating the safer recycling of plastics from WEEE.

5.1.1 DBDE, a Brominated Flame Retardants (BFRs)

The five principal Brominated Flame Retardants (BFRs) include Tetrabromobisphenol A (TBBPA), Hexabromocyclododecane (HBCD), and three commercially formulated varieties of Polybrominated Diphenyl Ethers (PBDEs), also referred to as biphenyl oxides. These are commonly identified as Decabromodiphenyl Ether (DBDE), Octabromodiphenyl Ether (OBDE), and Pentabromodiphenyl Ether (PentaBDE). The structures for these chemicals are shown in Figure 5.1.

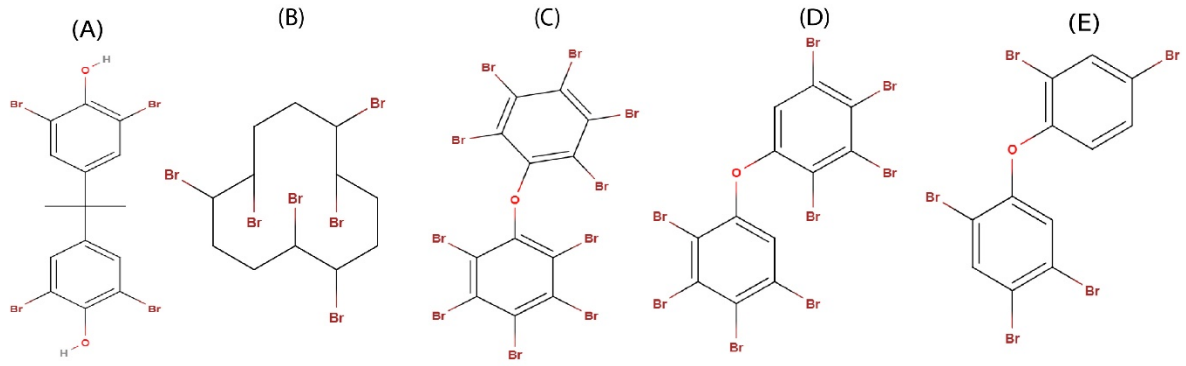

Figure 5.1 Chemical structures of (A) TBBPA, (B) HBCD, (C) DBDE, (D) OBDE, and (E) PentaBDE.

Polybrominated Diphenyl Ethers (PBDEs)

The PBDEs potentially encompass 209 distinct congeners, which vary in the number and positions of bromine atoms [104]. Similar to Polychlorinated Biphenyls (PCBs), these congeners are identified using the numbering system established by the International Union of Pure and Applied Chemistry (IUPAC). However, the actual number of PBDE congeners present in commercial mixtures is significantly lower than the theoretical maximum. This reduction is primarily due to the instability of many congeners, which often leads to their debromination.

Commercially utilized PBDEs are recognized for their chemical stability, which is a key property that makes them effective as flame retardants in various consumer products. Despite this inherent stability, research has indicated that these compounds are susceptible to debromination under specific conditions. One such method for inducing debromination is photolysis [105], [106], a process in which light energy, particularly in the form of ultraviolet radiation, initiates the breakdown of chemical bonds within the PBDE molecules. This photolytic degradation can lead to the release of bromine atoms from the compound, thereby reducing the environmental and health risks associated with these persistent organic pollutants. In our current work, we have concentrated on examining the influence of photolytic activity on the degradation of PBDEs. Through systematic analysis, we aim to understand the efficiency and conditions under which photodegradation can serve as a viable approach for the remediation of PBDEs, potentially contributing to safer waste management and environmental conservation practices.

Decabromodiphenyl Ether (DBDE)

DBDE is one of the most widely used brominated flame retardants in the world. Its high bromine content makes it particularly effective at reducing the flammability of a variety of materials, including plastics, textiles, and electronics. DBDE is a member of the polybrominated diphenyl ethers (PBDEs) family and is commonly referred to as BDE-209 due to its position as the 209th congener in the PBDE chemical series, which includes 209 possible substances.

DecaBDE, known for its persistence in the environment and bioaccumulative properties, has been a significant concern due to its widespread presence among top predators such as foxes, birds of prey, and polar bears in polar regions, as well as other animals. Traces of DecaBDE have even been found in human breast milk [107]. Although not immediately toxic, it is suspected of causing long-term adverse effects on embryonic development, specifically developmental neurotoxicity. Due to its persistent nature, DecaBDE is classified as a PBT substance (persistent, bioaccumulative, and toxic). This classification has led to calls for its ban, particularly in electronics and electrical devices. The manufacture of two other common formulations, penta- and octa-BDEs, was discontinued in the U.S. in 2004 following evidence of their bioaccumulation and disruption of biological processes such as the endocrine system, a ban which was preceded by the European Union's decision earlier that year [108], [109]. Despite the ban on penta- and octa-BDEs, DecaBDE continued to be produced and used, making up over 83% of global PBDE production in 2001 [110]. However, DecaBDE itself was banned in 2008, yet its persistent properties ensure that it remains a significant environmental contaminant [111], continuously released from products manufactured before the ban and from industries using PBDEs. This flame retardant is mixed with different plastics like ABS, PC, and HIPS which are detailed below.

In this study, industrial DBDE was used. It is known to contain other polybrominated diphenyl ethers (PBDEs) as trace level (0.3-3.0%), nonabromodiphenyl ether (NBDE) being the most abundant [112]. Commercial DBDE (GC Deca 83) was purchased from Greenchemical S.p.a (Italy).

5.1.2 Description of the analyzed plastics

Acrylonitrile butadiene styrene (ABS)

ABS is a product of systematic polymerization of monomers: acrylonitrile, 1,3-butadiene, and styrene [113]. Its chemical structure is represented in Figure 5.2 as $(C_3H_3N)_m \cdot (C_4H_6)_n \cdot (C_8H_8)_p$. ABS polymers exhibit high toughness, adequate rigidity, good thermal stability, and high resistance to chemical attack and environmental stress cracking. ABS is notably valuable because it's cheap, durable, and has low coefficient of thermal expansion.

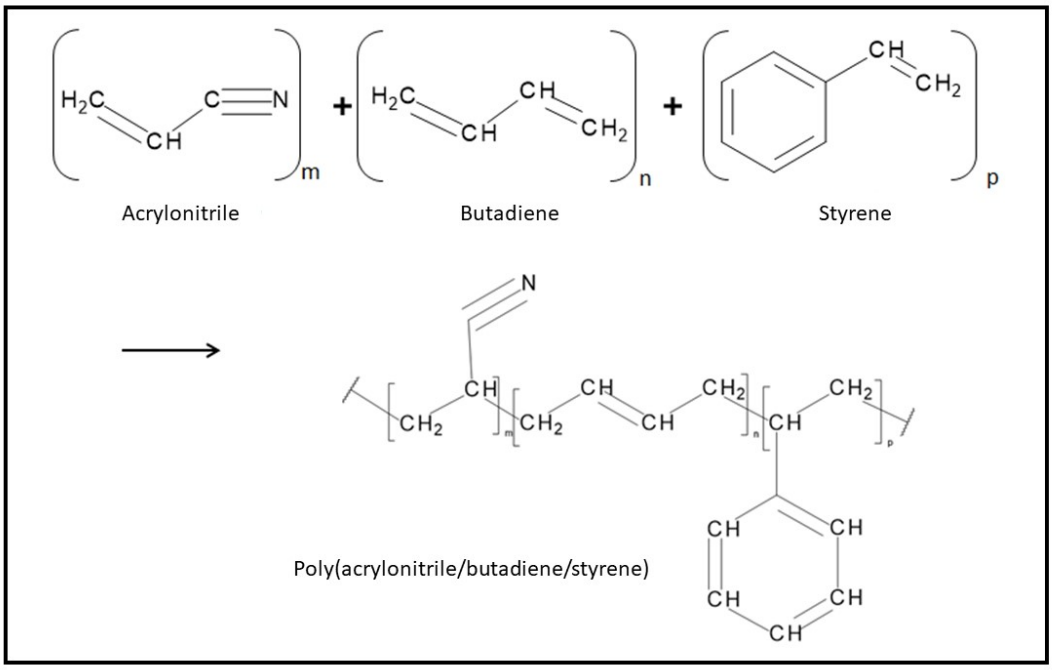

Figure 5.2 Acrylonitrile Butadiene Styrene (ABS) as product of polymerization of monomers: acrylonitrile, butadiene, styrene.

Polycarbonate (PC)

PC is a durable thermoplastic polymer used in a wide range of applications due to its exceptional transparency, high impact resistance, and good temperature resistance. The polymer represented in Figure 5.3 is composed of bisphenol A (BPA) units linked by carbonate groups (-O-(C=O)-O-) [114].

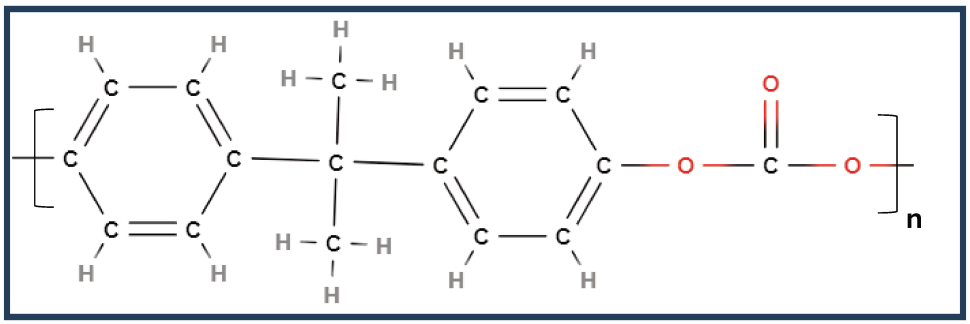

Figure 5.3 Chemical structure of Polycarbonate (PC) derived from Bisphenol A (2,2-bis(p-hydroxyphenyl) propane).

High Impact Polystyrene

HIPS is a versatile and widely used graft copolymer [115] known for its robustness and ease of processing. It features a two-phase structure represented in Figure 5.4, where a continuous phase of stiff polystyrene provides structural integrity, and a dispersed phase of polybutadiene rubber particles imbues the material with enhanced impact resistance.

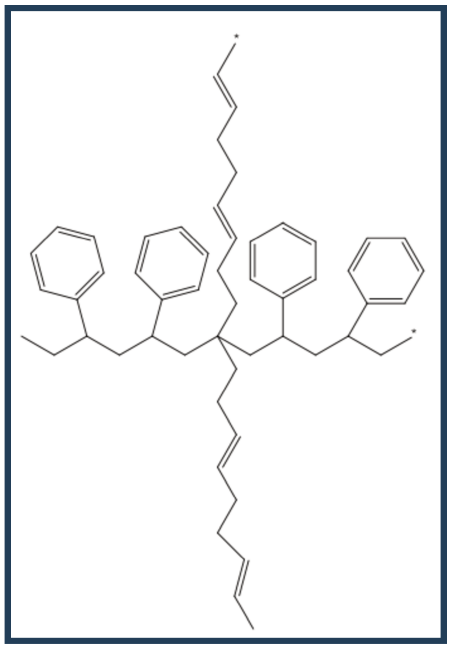

Figure 5.4 High Impact Polystyrene (HIPS) consists of the polystyrene backbone with polybutadiene chains branching from it in each direction.

5.1.3 Debromination protocol using UV-vis irradiation

The irradiation of DBDE-containing plastics was carried out with a Xenon lamp LC8 (Hamamatsu Photonics France S.A.R.L, France) at the UMET laboratory (U. Lille) in the frame of Hanene Oumeddour's PhD thesis. The lamp covers a broad spectrum in the UV–visible range, similar to the spectrum of sunlight. This light source was equipped with an optical fiber with an outer beam diameter of 5 mm. The samples were fixed horizontally in a PTFE cell equipped with a quartz window of 1 mm thickness to allow maximum irradiance. The distance between the fiber and the sample was kept at 5 mm. The light intensity was determined to be 19 mW cm^{-2} at a wavelength of 365 nm using a C6080-13 power meter (Hamamatsu Photonics France S.A.R.L., France). Plastics containing 10%wt DBDE were produced and were irradiated for different durations. Samples analyzed using mass spectrometry, ABS-DBDE, PC-DBDE, HIPS-DBDE, were irradiated for 5 min, 10 min, and 90 s, respectively. HIPS-DBDE sample analyzed using Raman and FTIR was irradiated for two different durations: 30 s and 60 s. The list of samples analyzed is given in Table 5.1. An example of untreated and treated samples is shown in Figure 5.5

Table 5.1 List of plastic samples used in debromination study using UV-Visible irradiation. Mixture with DBDE corresponds to 10%wt.

ABS	PC	HIPS
ABS-DBDE non irradiated	PC-DBDE non irradiated	HIPS-DBDE non irradiated
ABS-DBDE irradiated (5 min)	PC-DBDE irradiated (10 min)	HIPS-DBDE irradiated (30 s, 60 s, and 90 s)

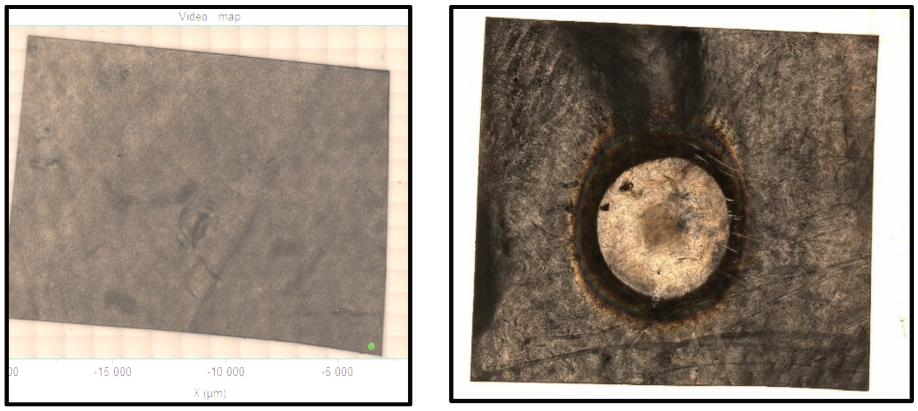

Figure 5.5 Images of ABS-DBDE samples. left: untreated (non-irradiated), right: treated (irradiated under UV-visible) at the center of the sample.

By analyzing plastics such as Acrylonitrile Butadiene Styrene (ABS), High Impact Polystyrene (HIPS), and Polycarbonate (PC) with or without Decabromodiphenyl Ether (DBDE), we seek to understand the effectiveness of UV-visible light in removing bromine, thereby mitigating the environmental and health risks associated with BFRs. To assess the effectiveness of debromination, Raman spectroscopy, FTIR and TOF mass spectrometry are used.

5.2 Raman analysis

In this section, the presence and subsequent removal of bromine from three types of plastic samples (ABS, PC and HIPS) containing commercial DBDE is investigated using Raman spectroscopy.
In a first step, the Raman spectrum of pure DBDE was recorded to establish the characteristic Raman bands of this compound, providing a reference for later comparisons to plastic samples treated with this brominated flame retardant. Then, plastic samples with or without the addition of 10%wt-DBDE were analyzed before and after being subjected to UV-visible light irradiation.

5.2.1 Analysis protocol for plastics

The first step for analyzing plastics is to find the optimized laser power for the sample to be able to analyze them without burning them. HIPS and HIPS with 10% DBDE were analyzed first to find the optimized power for the analysis. These plastic samples are very sensitive to high laser power.

Figure 5.6 Image of HIPS DBDE plastic sample untreated, showing the laser burn in red circle at 20 mW energy during Raman analysis using 100X objective at wavelength of 532 nm and exposure time of 10 s.

Figure 5.6**Error! Reference source not found.** displays a picture of HIPS-DBDE sample non irradiated (untreated) after Raman analysis using 532 nm laser at 20 mW power with the exposure time of 10 s. We found burns even at 6 mW energy at this high exposure time of 10 s, which suggests that we need to reduce the energy at exposure time of 10 s, while at 1.3 mW there are no visible burns.

The irradiated part of the sample (treated sample) becomes more sensitive to the laser, as shown in Figure 5.7 under three different circles.

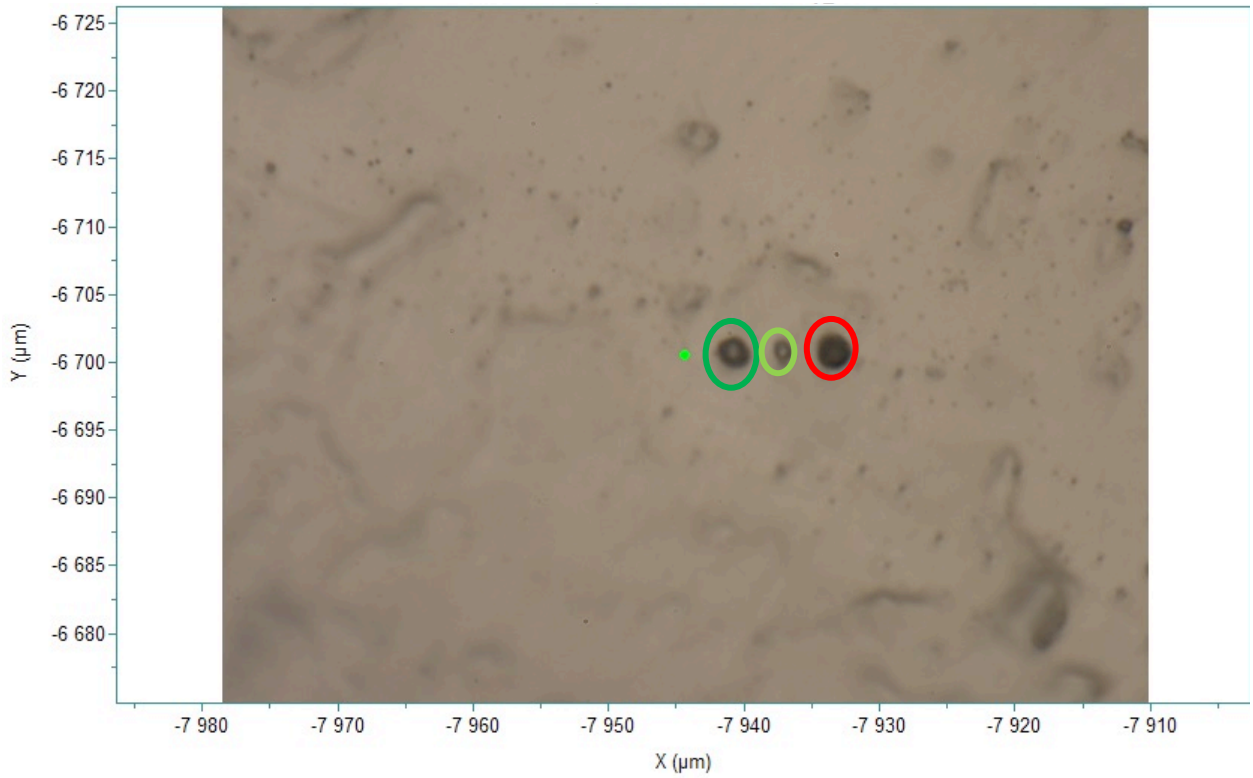

Figure 5.7 Laser burn on HIPS DBDE treated sample (UV-Vis exposed) red circle at 785 nm laser 10% (3.9 mW energy), light green circle at 532 nm laser 10% (4 mW energy), green at 532 nm laser 2% (0.80mW energy) all exposed for 10 s.

The instrument has its own response (optics, filters, detectors), so while recording the Raman spectra there are ripples in the spectrum (see Figure 5.8). To get rid of these ripples, ICS (intensity correction system) is applied, to account for the instrument response, mainly the ripples induced by filters and the efficiency of the detector.

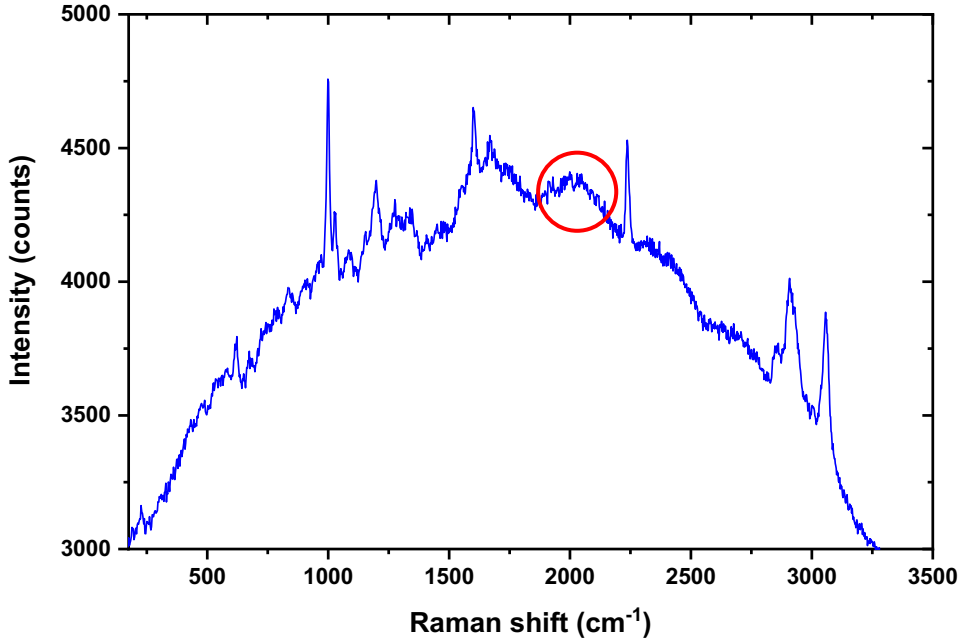

Figure 5.8 ABS-DBDE spectrum showing ripples in red circle.

A calibrated white light source is used to generate a response (which depends on the laser, the grating and the detector used). It is compared to the "source" spectrum to yield a correction factor, which is applied to raw spectrum for ICS correction. When the automatic intensity correction is activated, the software (LabSpec 6) automatically applies the appropriate correction factor based on the active laser wavelength and diffraction grating pair.

Often, the crucial details within a Raman spectrum are hidden by substantial background fluorescence, which may originate from the sample itself, the substrate, or even from optical elements like the objective. Fluorescence tends to occur much more frequently than Raman scattering, emitting a much more intense signal that can obscure the Raman signal. To circumvent this issue, selecting different excitation lasers can be effective, particularly near-infrared lasers, which are less likely to be absorbed by the molecules, hence reducing fluorescence. The absorption process is less pronounced in the near-infrared region, making it an optimal choice for such applications. The most commonly employed laser wavelength in Raman spectroscopy is 785 nm, which minimizes fluorescence while maintaining a relatively high Raman signal intensity. An example can be seen in a Figure 5.9 showing spectra of HIPS-10% DBDE exposed for 60 s under

UV-visible irradiation, excited by two different wavelengths: 532 nm and 785 nm keepi ng all the parameters sam. The spectrum taken with the 785 nm laser exhibits clear peaks that are otherwise hidden in the spectrum taken with the 532 nm laser.

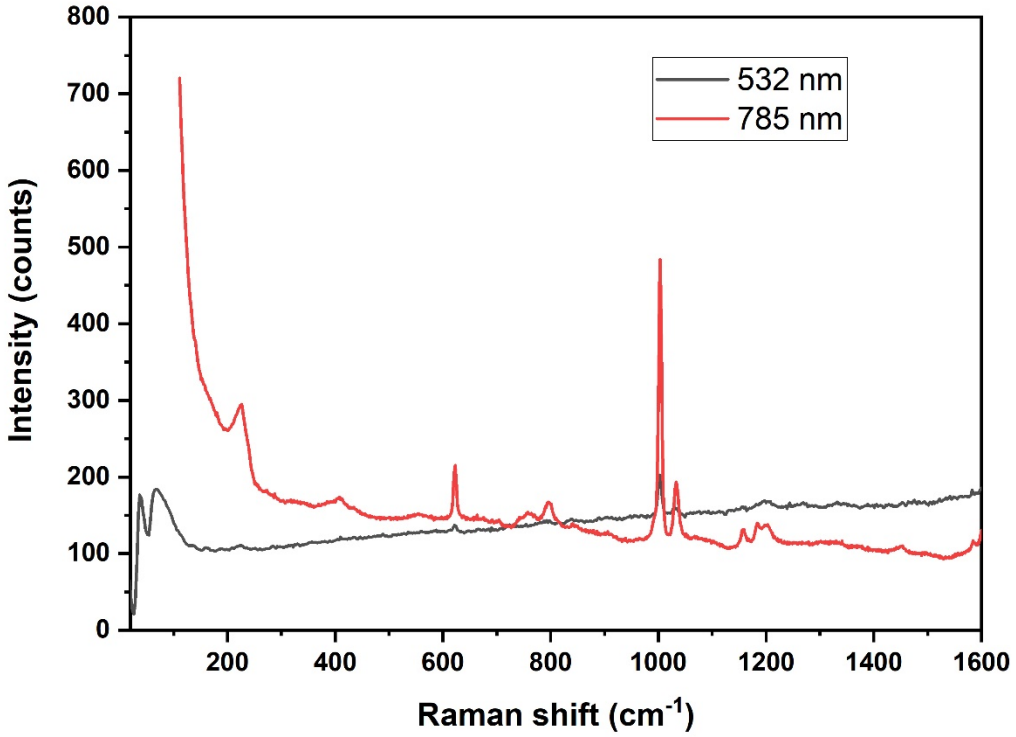

Figure 5.9 HIPS- DBDE exposed for 60 s under UV-visible irradiation Raman spectra measure with a 532 nm (black) and a 785 nm laser (red).

5.2.2 Decabromodiphenyl Ether (DBDE)

Figure 5.10 displays the Raman spectrum of Decabromodiphenyl Ether (DBDE) powder, which was obtained using 532 nm excitation. The spectrometer's aperture was set to a size of 100 μm. For this measurement, a 100x reflective objective was employed, along with a grating specified at 600 lines per millimeter for a central wavelength of 500 nm. The spectrum was compiled from 100 accumulated scans, each with an exposure time of 4 seconds. Bands were identified and assigned [116] as shown in Table 5.2.

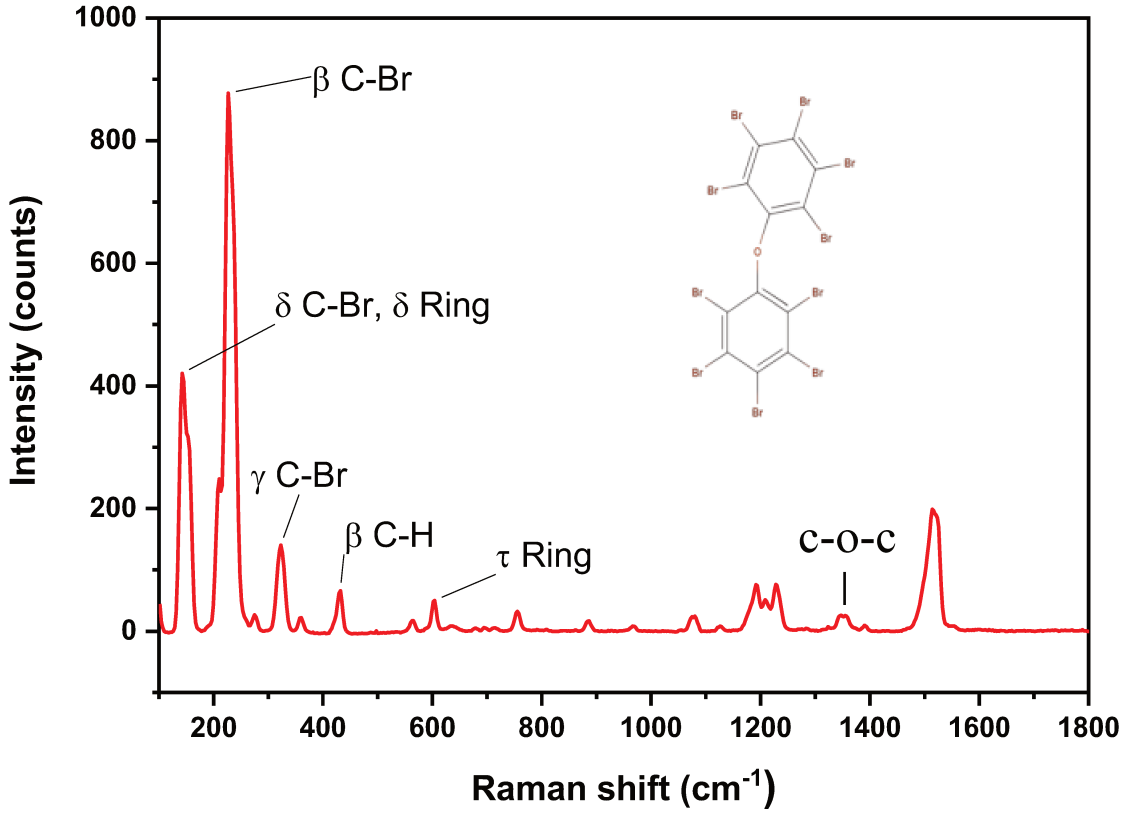

Figure 5.10 Raman spectrum of Decabromodiphenyl Ether (DBDE) in the 100-1800 cm^{-1} range using a 532 nm excitation wavelength.

Table 5.2 Raman band of commercial DBDE sample (Raman shift, strength, and attribution). s, m, w stand for strong, medium and weak, respectively. β refers to in plane bending, γ, out of plane bending, δ, deformation, and τ, torsion.

Raman shift (cm^{-1})	Stength	Assignment
142	s	$\delta\ C-Br, \delta\ Ring$
153	s	$\tau\ Ring$
226	s	$\beta\ C-Br$
275	w	
323	m	$\gamma\ C-Br$
360	W	
431	m	$\beta\ C-H$
565	w	
602	w	$\tau\ Ring$

755	**w**	
884	**w**	
1079	**w**	
1191	**m**	
1227	**m**	
1352	**w**	**c-o-c**
1514	**s**	

5.2.3 ABS & ABS_DBDE

Raman spectra of ABS and ABS mixed with DBDE were acquired using a 532 nm laser, with the spectrometer's aperture set to 200 μm. A 100X objective and a 600 lines per millimeter grating centered at 500 nm were utilized for the measurements. The spectrum of pure ABS was compiled from 10 accumulated scans, each with an exposure time of 4 seconds, whereas the spectrum of ABS with DBDE was compiled from 50 accumulated scans both with 1.3 mW power, each with an exposure time of 4 seconds.

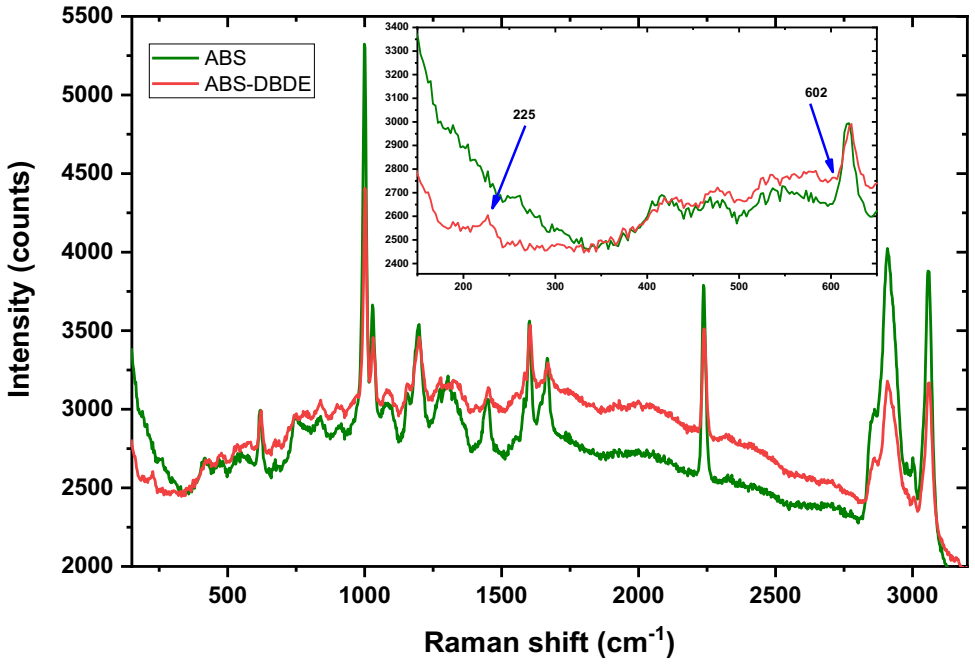

Figure 5.11 Raman spectrum of ABS (green), and ABS-DBDE (red) in the 100-3200 cm^{-1} range using a 532 nm excitation wavelength.

Raman spectroscopy was employed to distinguish between ABS and ABS with DBDE, aiming to verify the presence of DBDE in the latter. This method is pivotal for later establishing the effectiveness of debromination in plastics. In Figure 5.11, two distinct Raman spectra are showcased: one for pure ABS (depicted in green) and the other for ABS mixed with DBDE (depicted in red). A comparison of these spectra against the spectrum of pure DBDE, as shown in Figure 5.10, reveals certain bands in the ABS with DBDE sample that are absent in the pure ABS. These bands, correlating with DBDE, are located at Raman shifts of 225 and 602 cm^{-1}. Additionally, the band at 1523 cm^{-1} is also attributed to DBDE, as supported by existing literature [117], with both the 225 and 1523 cm^{-1} bands being indicative of C-Br bonds. The bands found in the ABS sample have been thoroughly identified [118] and are detailed in Table 5.3, and the bands which are associated with DBDE are highlighted in green.

Table 5.3 Raman shift in cm^{-1} present in pure ABS and ABS with DBDE and band assignment [117], [118].

ABS Raman shift (cm^{-1})	ABS-DBDE Raman shift (cm^{-1})	Reference Raman shift (cm^{-1})	Assignment
-	225.29	-	β C-Br
-	602	-	τ *Ring* DBDE
618.82	621.74	621	δ (ring) of aromatic
745.97	745.84	745	CH_2 resonance
999.54	1000.85	1002	aromatic ring breathing
1030.65	1030.38	1032	δ (C-H) in-plane aromatic
1096.15	1098.3	1099	ν (C-C) in-plane
1155.08	1155	1156	δ (C-H) out-of-plane of aromatic ring
1183.36	1182.76	1183	δ (C-H) in-plane of aromatic ring
1197.5	1199.29	1200	ν_s (C-C)
1438.13	1439.68	1441	ν_{as} (C-C) of aromatic ring
1451	1452.24	1453	δ (CH2)
1582.1	1583.55	1583	ν_{as} (C-C) of aromatic ring
1601.3	1603.67	1603	ν_s (C-C) of aromatic ring
1666.94	1668.35	1668	ν (C=C trans)
2235.37	2239.59	2239	ν (C≡N)
2854.36	2854.53	2854	ν_s (CH_2)
2904.49	2906.36	2906	ν_{as} (CH_2)

2978.18	2981.3	2981	ν (C-H) aliphatic
3001.75	3004.41	3004	ν_{as}(=C-H) of -CH=CH-R
3058.31	3060.44	3060	ν (=C-H) of aromatic ring

5.2.4 PC & PC-DBDE

Raman spectra of PC and PC with DBDE were recorded as shown in Figure 5.12. These spectra were obtained under the same experminetal setup as used for ABS, utilizing a 532 nm excitation wavelength. Spectra were recorded over 100 accumulated scans, each with an exposure time of 4 s.

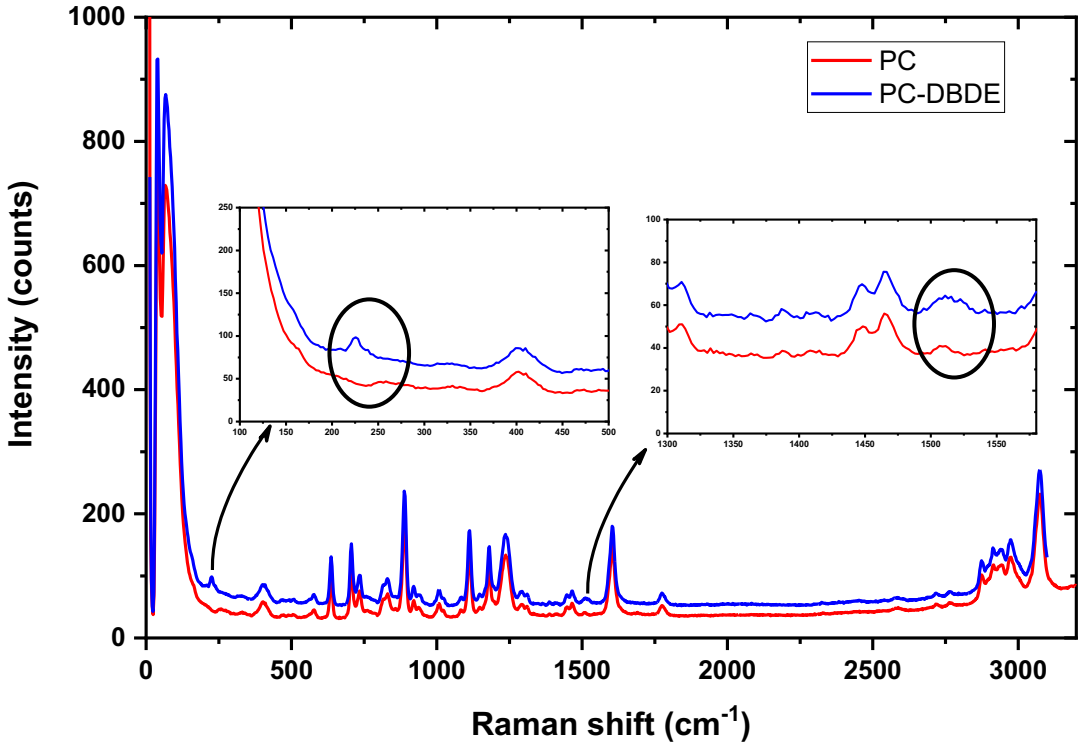

Figure 5.12 Raman spectra of PC (red) and PC with DBDE (blue) recorded utilizing irradiance wavelength of 532 nm. Two regions are zoomed to show the presence of band at 225 cm^{-1} and 1523 cm^{-1} in case of sample with DBDE, and bands are circled in black too clearly identify.

Figure 5.12 provides detailed views of the Raman spectra for Polycarbonate (PC) and PC blended with Decabromodiphenyl Ether (DBDE) across different Raman shift ranges. In zoomed spectra

on left, which focuses on the lower Raman shift range, a distinct band at 225 cm^{-1} is observed in the spectrum of the PC-DBDE sample. This band is attributed to the C-Br bond in DBDE, indicating its presence in the mixture. Conversely, on right, which zooms into the higher Raman shift spectrum, there's a noticeable difference in the PC sample with a band at 1509 cm^{-1}. For the PC-DBDE blend, this area shows a broader band that merges the 1509 cm^{-1} band with another at 1523 cm^{-1}; the latter is another characteristic band of DBDE [117]. These observations, particularly the bands at 225 cm^{-1} and 1523 cm^{-1}, serve as clear evidence of DBDE's presence in the PC-DBDE sample. A comprehensive list of bands identified in both samples is documented in Table 5.4 and the bands present due to the DBDE are highlithed green in the table.

Table 5.4 Raman shift band present in PC and PC with DBDE with highlighted band of DBDE present in DBDE.

PC Raman shift (cm^{-1})	PC-DBDE Raman shift (cm^{-1})	PC Raman shift (cm^{-1})	PC-DBDE Raman shift (cm^{-1})
40.20	40.16	1111.13	1113.07
67.57	67.87	1147.16	1148.20
-	225.50	1179.16	1181.08
402.37	401.82		
577.88	577.34	1237.04	1236.54
637.33	636.80		
706.62	706.09	1293.38	1292.05
734.79	734.80	1309.92	1311.80
		1448.12	1449.07
816.24	815.38	1464.64	1464.16
830.98	830.45	1509.54	1510.81
		-	1523.34
888.74	888.22	1603.80	1603.33
921.74	921.34	1774.51	1774.04
936.26	940.61	2874.46	2874.06
		2915.81	2913.07
1008.07	1007.55	2943.15	2943.90
1023.71	1021.27	2975.47	2975.07
1083.72	1084.26	3075.11	3074.71

5.2.5 HIPS & HIPS-DBDE

Raman spectra of HIPS and HIPS-DBDE were acquired using a 785 nm laser, with the spectrometer's aperture set to 100 μm. A 50X objective and a 600 lines per millimeter grating centered at 500 nm were utilized for the measurements. All the spectrum of HIPS and HIPS-DBDE unexposed and exposed for different time were compiled from 200 accumulated scans, each with an exposure time of 10 seconds with 39 mW power.

When comparing high-impact polystyrene (HIPS) to HIPS that has been modified with Decabromodiphenyl ether (DBDE), it is observed that the pure HIPS exhibits a band at 220 cm^{-1}, while the HIPS containing DBDE should display additionally a band at 225 cm^{-1}. This shift indicates that in the HIPS with DBDE, two bands are merged, leading to an increased intensity of the band at 225 cm^{-1}. This particular band is attributed to the C-Br bending, as identified in DBDE spectra and corroborated by existing literature.

Figure 5.13 displays the baseline-subtracted Raman spectra of HIPS, HIPS-DBDE, and HIPS-DBDE irradiated for 30, 60, and 90s. Table 5.5 summarizes the positions of the specific bands recorded in these spectra. A band around 225 cm^{-1} is observable in all spectra. A band around 225 cm^{-1} can be observed in all spectra. The delicate elimination of the baseline in the low Raman shift range, together with the proximity of the HIPS and DBDE bands, means that Raman is not the most appropriate tool for studying bromine elimination in HIPS. This is why we have chosen to use FTIR as a complementary technique for HIPS analysis only.

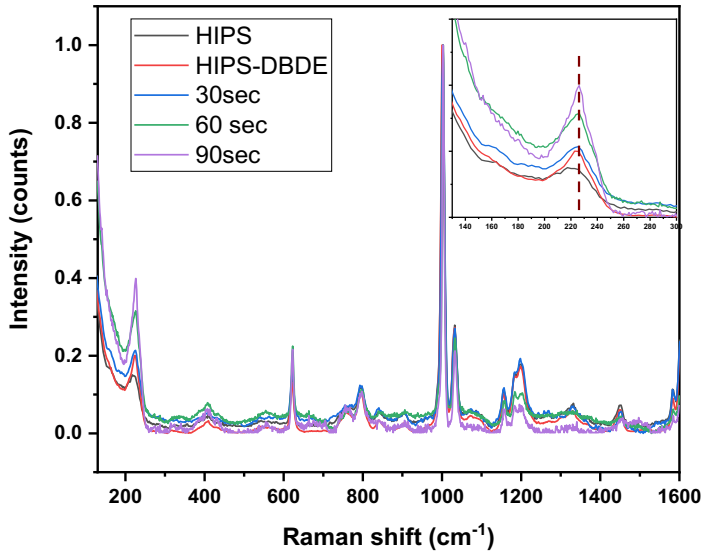

Figure 5.13 Raman spectra of HPS (black), HIPS- DBDE (red), HIPS-DBDE irradiated for 30 s (blue), 60s (green), 90s (purple), recorded using irradiance wavelength of 785 nm.

Table 5.5 Raman shift bands of HIPS, HIPS- DBDE before and after treatment for 30s, 60s, and 90s.

HIPS Raman shift (cm^{-1})	HIPS_DBDE Raman shift (cm^{-1})	30 sec Raman shift (cm^{-1})	60 sec Raman shift (cm^{-1})	90sec Raman shift (cm^{-1})
220.11	225.33	225.71	225.71	225.71
410.73	410.11	408.83	408.31	408.31
541.3	541.63	546.4	555.75	555.75
621.38	622	622	622.7	622.7
701.8	702.37			
760.43	759.36	760.02	760.17	760.17
795.62	797.35	796.76	796.5	796.5
844.2	842.65	843.73	843.51	843.51
906.19	904.66	905.89	906.9	906.9
1002.68	1002.36	1003.52	1003.09	1003.09
1032.68	1032.67	1033.23	1032.84	1032.84
1072.46	1072.06	1073.04		
1095.93	1095.3	1097.9		
1156.55	1156.91	1157.3	1157.53	1157.53
1184.91	1183.68	1183.55	1184.74	1184.74
1198.6	1198.84	1198.75	1199.3	1199.3
1306.16				

1328.66	1328.64	1327.21		
1366.79				
1450.89	1450.85	1451.54	1451.84	1451.84
1495.87	1495.3	1494.36		
	1522.91			
1584.85	1584.01	1585.53	1585.39	1585.39
1603.43	1603.05	1603.49	1603.12	1603.12
1655.26	1650.42			
1666.99	1666.07	1667.04		
2854.28	2853.78	2854.07		
2907.56	2908.12	2909.6		
2978.09	2978.91	2977.85		
3003.16	3003.39	3003.3		
3056.45	3055.95	3055.35		

5.3 FTIR analysis

The FTIR spectra of pristine HIPS, HIPS-DBDE non-irradiated, and HIPS-DBDE irradiated for 30 s and 60 s, were recorded to evaluate the degradation of DBDE against irradiation time. Most of the bands in the spectra are associated with vibrations in the plastic polymer (Figure 5.14 (a)). However, the band located at 1354 cm^{-1}, as shown in Figure 5.14 (b), corresponds to C-O-C stretching vibration and can only be assigned to the ether bond in DBDE. Due to spectral congestion, weak C-Br bands in the 500-600 cm^{-1} spectral range could not be observed.

The spectral evolution of HIPS-DBDE around 1354 cm^{-1} as a function of irradiation time is shown in Figure 5.14 (b). The spectra were baseline-corrected using LabSpec 6 software and normalized to the band located at 1181 cm^{-1}. Spectra shows a decrease in the absorbance at 1354 cm^{-1} with the irradiation time, indicating cleavage of the ether bond present in DBDE. FTIR can prove the destruction of the DBDE molecule, but not the cleavage of the C-Br bonds, nor the elimination of bromine. To solve this problem, mass spectrometry is used.

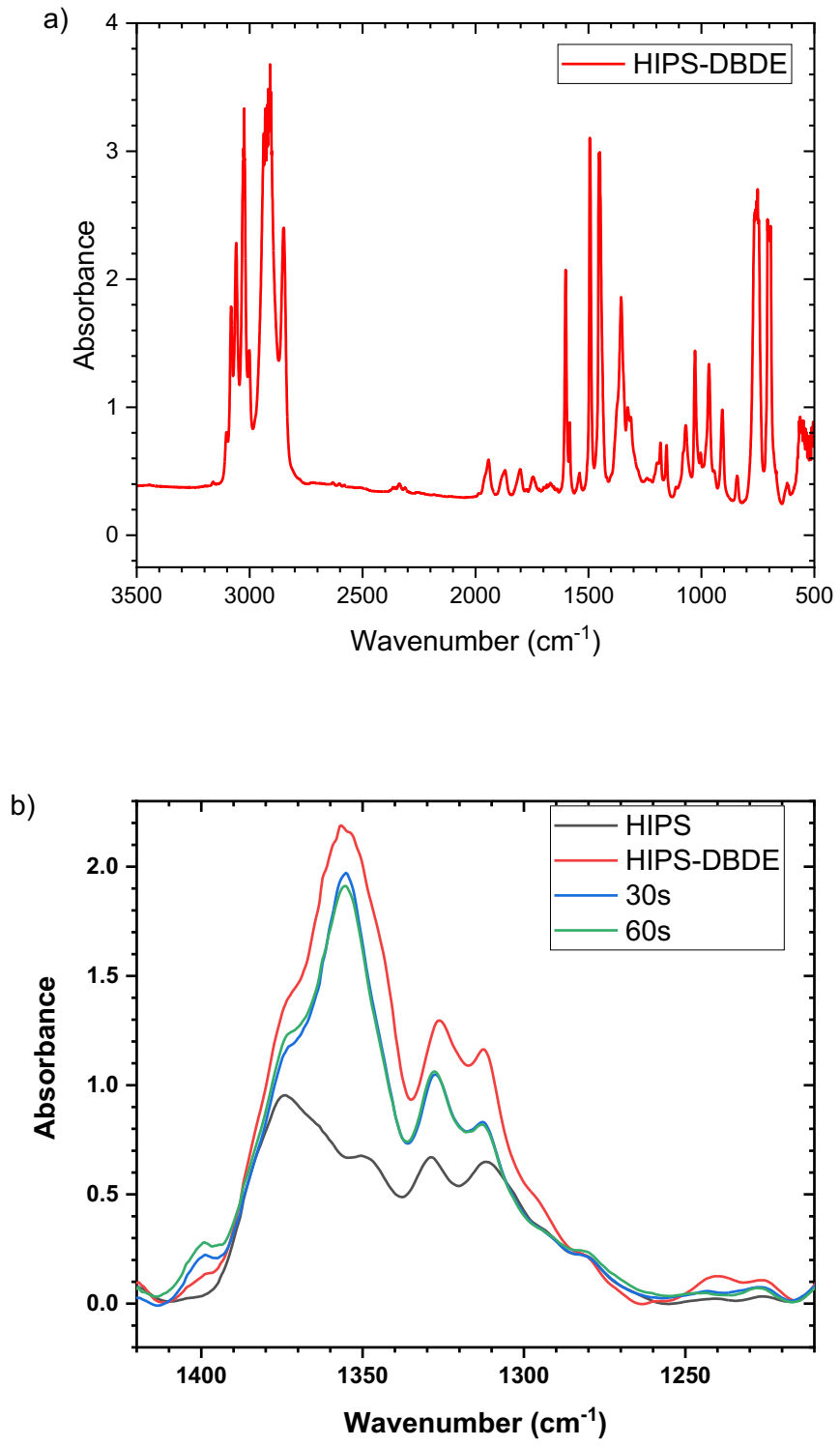

Figure 5.14 (a) Reflection FTIR spectrum of HIPS-DBDE, (b) Evolution of the 1290-1410 cm^{-1} band region in HIPS, HIPS-DBDE non-irradiated, and HIPS-DBDE irradiated in ambient air for 30 s and 60 s. The spectra are baseline-corrected and normalized to the 1181 cm^{-1} band.

5.4 HR- MS analysis

The objective of this section is manyfold: identify specific LDI/L2MS signatures of DBDE, determine experimental conditions for which these signatures can found in DBDE-containing plastics, and identify brominated compounds associated with the degradation of DBDE in plastics to evaluate the efficiency of debromination process following UV-vis exposure. Three different types of plastic containing or not commercial decabromodiphenylether (DBDE) were considered: acrylonitrile butadiene styrene (ABS), high impact polystyrene (HIPS), and polycarbonate (PC). Spectra before and after UV-vis irradiation were compared for the three types of plastic.

5.4.1 DBDE

Mass spectra of commercial DBDE were obtained under two distinct conditions to serve as benchmarks for analyzing plastic samples and assessing the degradation of DBDE and elimination efficiency of bromine. In Figure 5.15, the spectra of commercial DBDE (see 5.1.1 for chemical composition) were recorded in positive polarity using a 266 nm desorption laser (upper panel – (a)) or a 532 nm wavelength (lower panel – (b)). Post-ionization at 266 nm did neither reveal additional mass peaks or enhance the amplitude of peaks already present by laser desorption/ionization (LDI). The presented spectra correspond then to LDI.

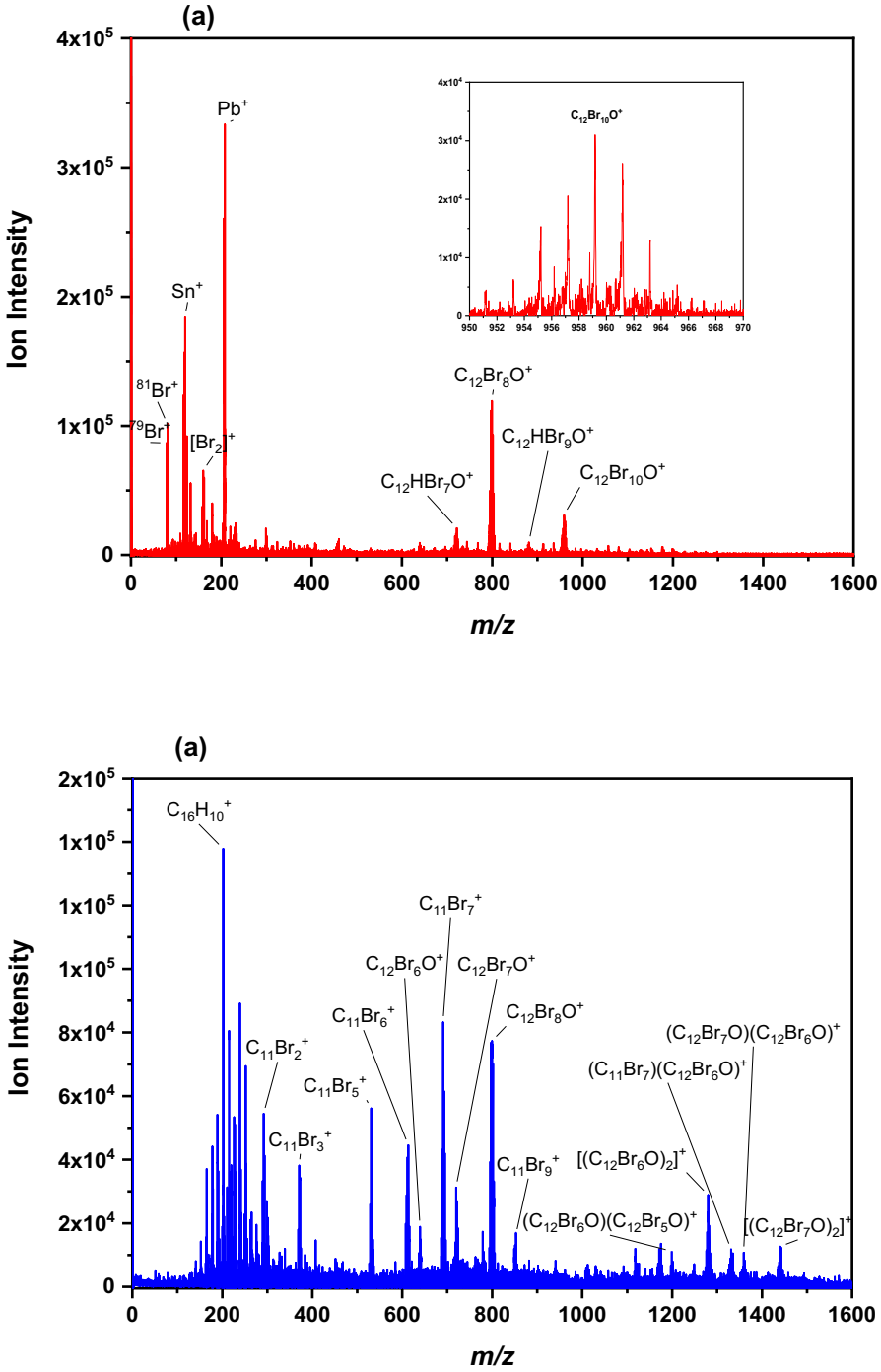

Figure 5.15 Positive polarity HR-LDI mass spectra of commercial DBDE using 532 nm (a) or 266 nm (b) with desorption energy of 1 mJ and 30 µJ respectively..

In the upper panel (a) of Figure 5.15 (532 nm desorption), several mass peak series centered at m/z 78, 160, 721, 79, 88, and 959 were identified. These peaks correspond to specific isotopic distributions of brominated compounds, including bromine cation (Br^+), dibromine cation (Br_2^+), heptabromodibenzofuran ($C_{12}HBr_7O^+$), octabromodibenzofuran ($C_{12}Br_8O^+$), nonabromodihenylether ($C_{12}HBr_9O^+$), and decabromodiphenylether ($C_{12}Br10O^+$). The relative intensity of the two latter is coherent with the expected composition of commercial DBDE. The dominating Br_7 and Br_8 derivatives probably arise from the fragmentation of DBDE and consecutive rearrangement.

In the spectrum obtained at 266 nm (lower panel of Figure 5.15), numerous fragments were observed, obscuring the characteristic DBDE peak at *m/z* ??? that is evident in the spectrum generated with desorption at 532 nm. Fragment species containing n Br atoms ($n = 2, 4-9$) are detected. At higher masses (*m/z* > 1000), dimers of the fragment species identified above could be assigned.

In the following mass spectra of plastic samples, ablation at 532 nm is chosen to produce a lower fragmentation of the DBDE additive

5.4.2 ABS & ABS-DBDE

LDI mass spectra were recorded in positive polarity for pure ABS and its 10%wt mixture with DBDE, before and after exposure to UV-visible irradiation. In the low mass range, the spectra display strong peaks (see Figure 5.16, corresponding to carbon clusters (C_n^+, with n = 10–16) in all samples. In addition, all samples reveal a peak related to deprotonated styrene ($C_8H_7^+$, *m/z* 103), styrene being part of the ABS monomer. Mass peak series centered at *m/z* 119, 799, and 959 are identified in the non-irradiated ABS with 10wt% DBDE sample. They correspond to ($C_3H_4Br^+$), octabromodiphenylether ($C_{12}Br_8O^+$, m/z 799), and DBDE (decabromodiphenyl ether) ($C_{12}Br_{10}O^+, m/z$ 959), respectively. These peaks disappear from the spectra of sample following UV-visible irradiation, suggesting an efficient debromination of the sample.

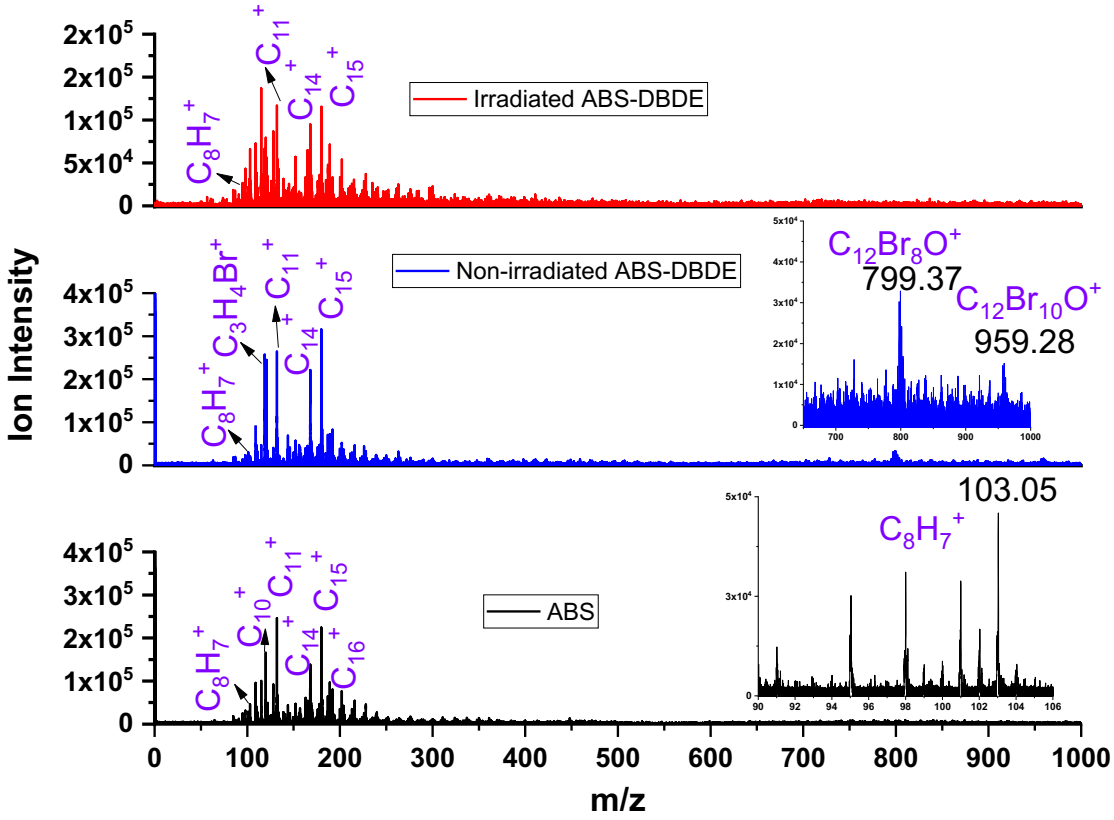

Figure 5.16 Positive polarity HR-LDI mass spectra of pristine ABS (black), and mixture of 90wt%ABS/10wt% DBDE non-irradiated (blue) or irradiated (red).

This debromination hypothesis is supported by negative mode spectra presented in Figure 5.17. In all the spectra with and without DBDE, major peaks correspond to carbon clusters C_n^- with n = 6–9. They are accompanied by C_nH^- species and are associated to the fragmentation of the ABS backbone. The spectrum of pristine ABS (black color) is represented only by these carbon clusters. The blue spectrum, representing ABS with 10wt% DBDE, shows additionally the two bromide peaks at *m/z* 78.92 and 80.92 expected in the bromine isotope distribution. The red spectrum, which corresponds to the sample made of ABS with 10wt% DBDE irradiated for 5 min by UV-vis, demonstrates that the bromine, originally added as a flame retardant, is eliminated after exposure to UV-visible light, confirming the efficiency of the debromination process.

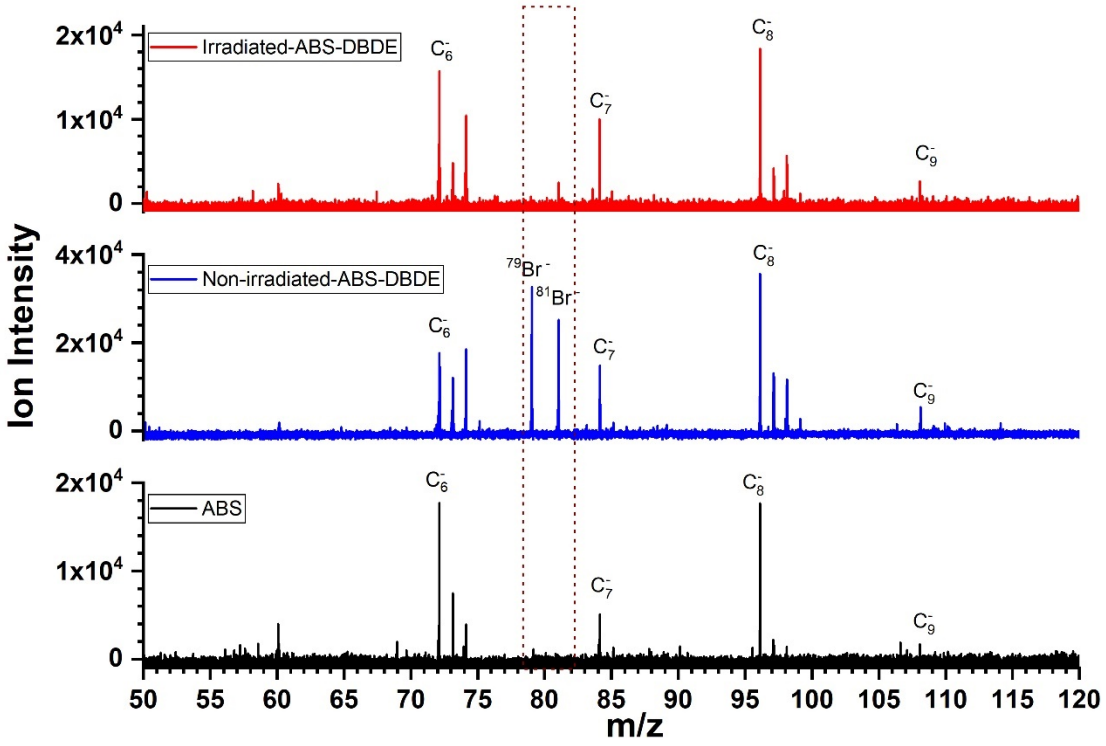

Figure 5.17 Negative polarity HR mass spectra of pristine ABS (black), and mixture of 90wt%ABS/10wt% DBDE non-irradiated (blue) or irradiated (red).

5.4.3 PC & PC-DBDE

LDI mass spectra were recorded in positive polarity for pristine PC, and its mixture with DBDE before and after exposure to UV-visible irradiation (see Figure 5.18). The recorded spectra display major peaks related to carbon clusters, C_n^+, with n = 10, 11, 12, 14, and 15, present in PC and PC with 10%wt DBDE sample, and with n = 10,11, and 15 present after treatment under UV-visible irradiation. Furthermore, PC sample reveals a peak related to protonated phenol ($C_6H_7O^+$, m/z 95.05). Additionally mass peak series centered at m/z 799.31 identified in the non-irradiated PC with 10wt% DBDE sample, which corresponds to octabromodibenzofuran ($C_{12}Br_8O^+$). These peaks disappear from the spectra of sample following UV-visible irradiation, suggesting the debromination effect.

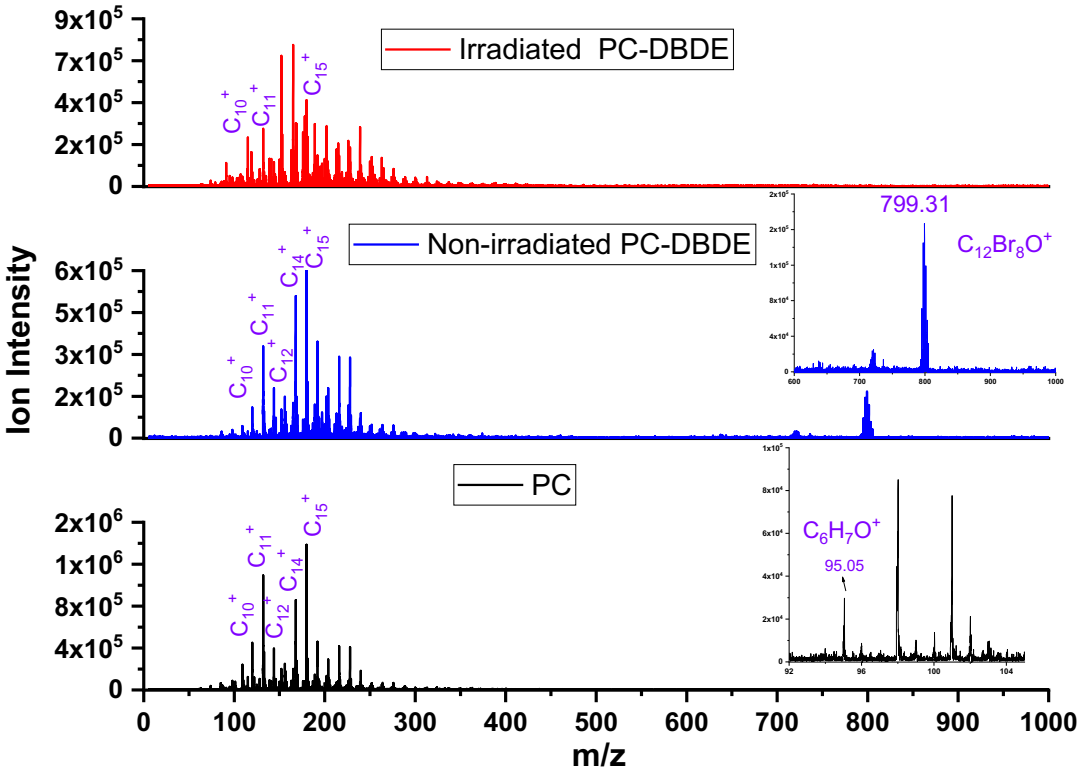

Figure 5.18 Positive polarity HR-LDI mass spectra of pristine PC (black color), mixture of 90wt% PC/10wt% DBDE non-irradiated (blue color) and irradiated (red color).

Figure 5.19 presents mass spectra for PC samples in various states, measured in negative ion mode. Across all spectra, including those with and without DBDE treatment, prominent peaks observed are attributed to carbon clusters, which serve as markers for the underlying PC polymer. The black spectrum is associated with pure PC showing carbon cluster C_n^- with n = 6, 7, and 8 and no significant peaks at the mass-to-charge (m/z) ratios typically related to bromine, confirming the absence of bromine in PC material. The blue spectrum, linked to PC containing a 10% weight of DBDE, showing high intensity peak of carbon cluster C_n^- with n = 6, 7, 8, and 9 of ABS and also reveals distinct peaks at *m/z* 79 and 81, aligning with the bromine isotopes, indicating the presence of brominated compounds. In contrast, the red spectrum corresponds to the PC with 10wt% DBDE after being subjected to UV-visible irradiation for 10 min, shows high intensity carbon cluster C_n with n = 6,7, and 8 as for pure PC, and the absence of bromine peaks here suggests successful removal of bromine, showcasing the effectiveness of the irradiation in the debromination process.

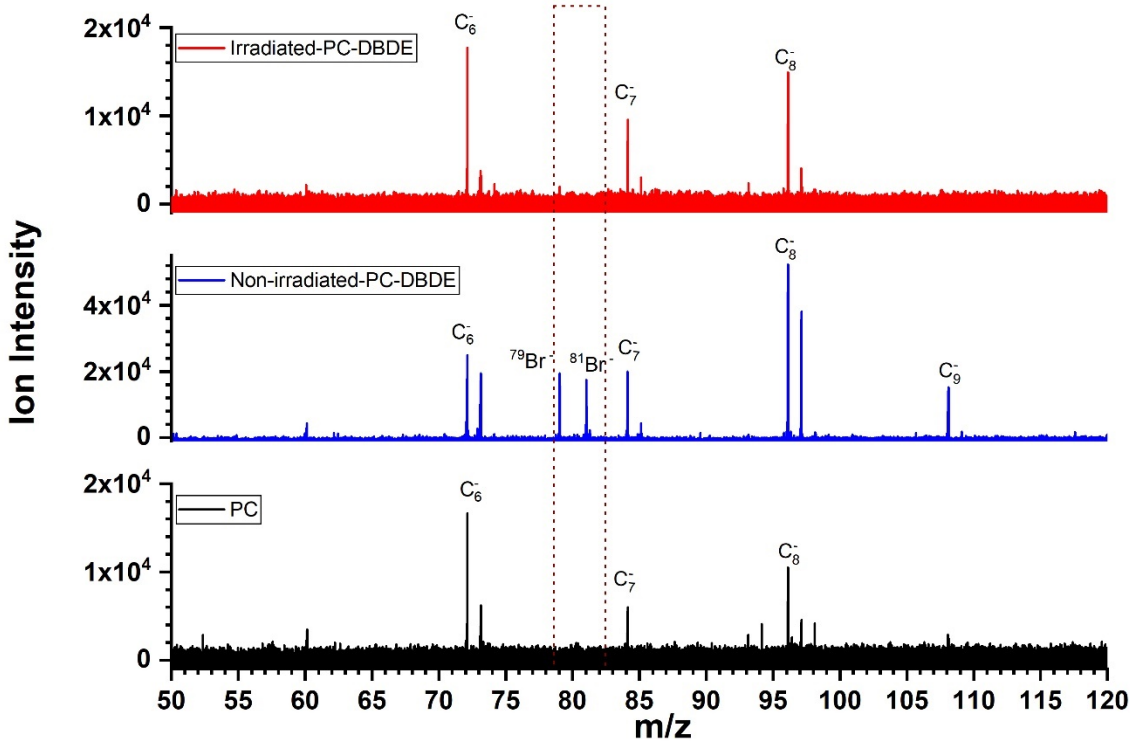

Figure 5.19 Negative polarity HR-LDI mass spectra of pristine PC (black color), mixture of 90wt% PC/10wt% DBDE non-irradiated (blue color) and irradiated (red color).

5.4.4 HIPS & HIPS-DBDE

LDI spectra were recorded in positive polarity for pure HIPS and its mixture with DBDE before and after UV-visible irradiation (see Figure 5.20). The spectra for HIPS (displayed in black) and HIPS with 10% DBDE before irradiation (shown in blue) exhibit strong peaks corresponding to carbon clusters, C_n^+, with *n*=10-20. Besides the carbon clusters, the spectra also show a peak for PAH $C_{16}H_{10}^+$ at *m/z* 202. In the non-irradiated HIPS with 10% DBDE sample, a mass peak series centered at *m/z* 799 is identified, corresponding to octabromodibenzofuran ($C_{12}Br_8O^+$). In the spectra of HIPS with 10% DBDE after irradiation, the presence of PAHs is evident. The peak at m/z 799.35 in the blue spectra disappears in the red spectra, indicating the debromination effect. However, peaks at *m/z* 248, 246, 264, and 266, suggesting bromine isotopic distribution, are

present but cannot be assigned due to low resolution. The irradiated sample was exposed to UV-visible irradiation for 90 s, which appears insufficient to achieve complete debromination.

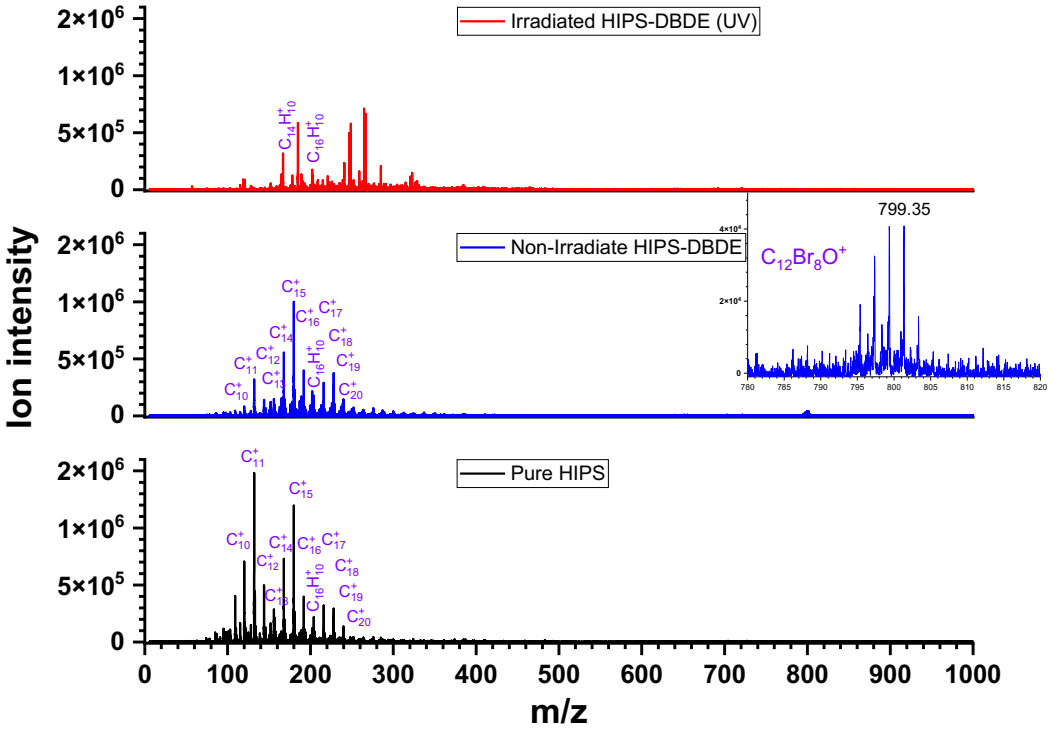

Figure 5.20 Positive polarity HR-LDI mass spectra of HIPS (black color), mixture of 90wt% HIPS/10wt% DBDE non-irradiated (blue color) and irradiated (red color).

Mass spectra recorded for pure HIPS, HIPS with 10wt% DBDE, irradiated and non-irradiated in negative mode is shown in Figure 5.21. High intensity peaks detected in all spectra corresponds to carbon cluster, C_n^-, n=5-9 and are associated with pristine HIPS. Black spectrum represents pure HIPS in which there is no peak of bromine which signifies that there are no bromine additives in pure HIPS plastic. Blue spectrum is for HIPS with 10wt% DBDE without treatment, bromine peak at 79 and 81 *m/z* can be seen which are for two isotopes of bromine. In the case of the red spectrum which represents the HIPS with 10wt% DBDE after UV-visible irradiation for 90 s, these bromine isotope peaks are reduced by one order of magnitude.

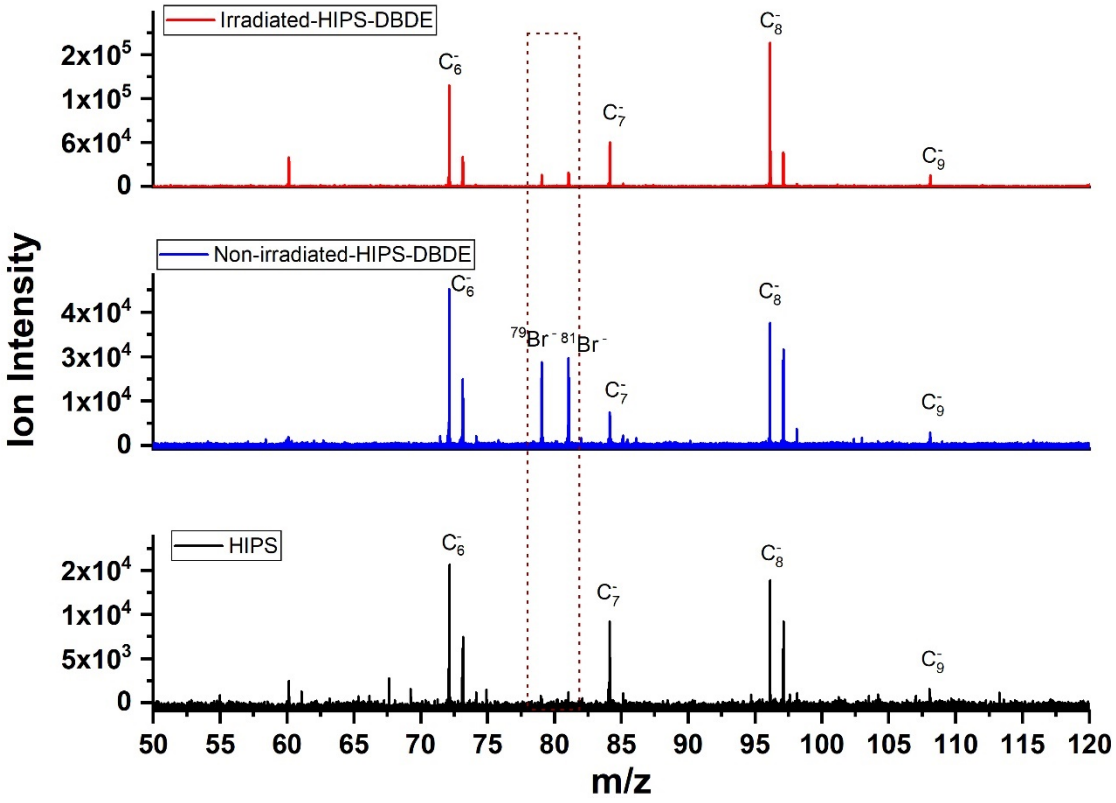

Figure 5.21 Ngative polarity LHR-LDI mass spectra of pristine HIPS (black color), mixture of 90wt% HIPS/10wt% DBDE non-irradiated (blue color) and irradiated (red color).

5.5 SR-L2MS analysis using the atmospheric-pressure interface

Instrumental development discussed in chapter 4 allowed us to progress in the direct analysis of solid sample at atmospheric pressure. Configuration 6 in section 4.3.5 seems to be the more prone in transferring molecules to the vacuum chamber's extraction region and ionizing them effectively. To further assess the efficiency of the sampling interface, particularly challenging materials like plastics were tested. Specifically, ABS with 10% DBDE and HIPS, both containing Styrene monomer ($C_8H_8^+$; 104 *m/z*), were analyzed.

The spectrum shown in this section with desorption using a Nd:YAG laser at 266 nm and 380 µJ energy, and ionization with the same laser type at 3.02 mJ energy. The timing was controlled: a 400 µs delay between desorption and opening the valve, followed by a 11.5 ms gap before ionization. The valve itself was opened for 200 µs. The significant observation in Figure 5.22 and

5.23 was the styrene peak, indicating the successful transfer of plastic monomers into the vacuum for analysis.

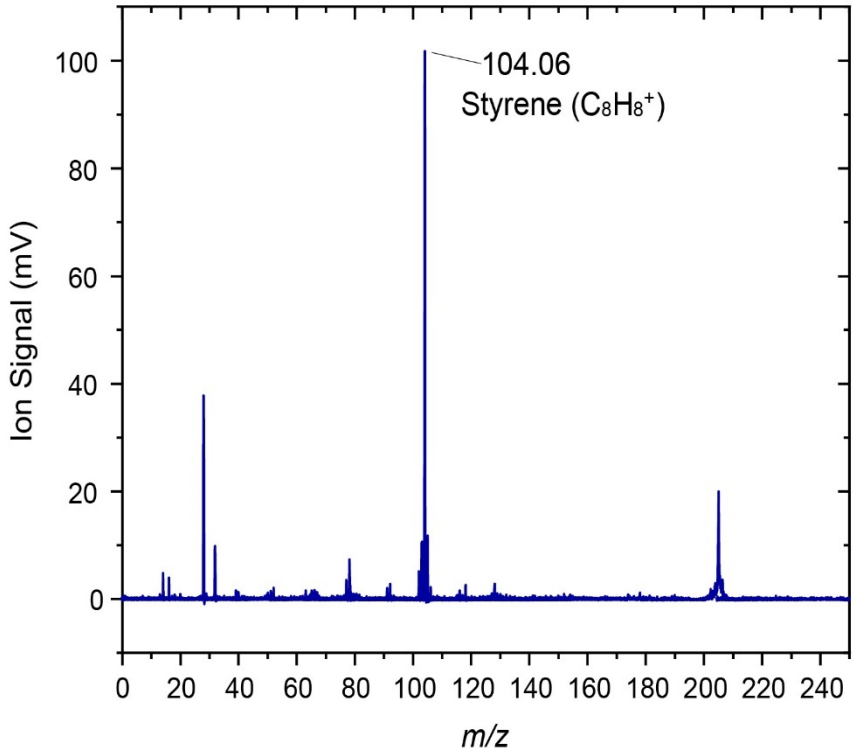

Figure 5.22 ABS (Acrylonitrile Butadiene Styrene)- 10% DBDE (Decabromodiphenyl ether) spectrum showing styrene mass peak.

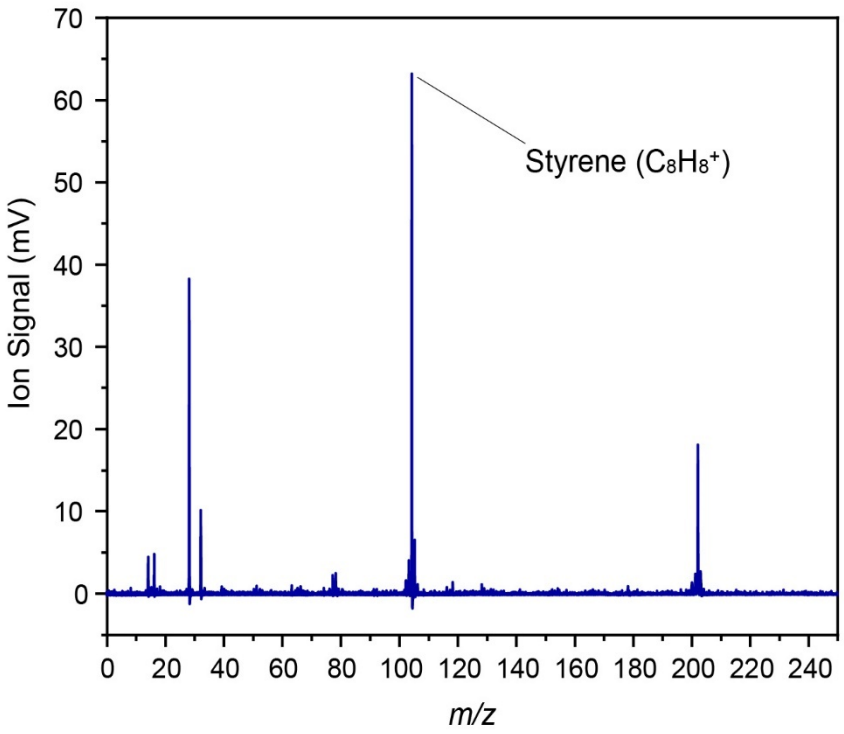

Figure 5.23 HIPS (High Impact Polystyrene) spectrum showing styrene mass peak recorded using 266 nm ionization and desorption laser wavelength.

At first sight, these spectra seem very poor when compared with those presented in section 5.4.2 (ABS) and 5.4.4 (HIPS). No bromine signal is evidenced, and only styrene is easily observable, but this comparison should be relativized. Firstly, the HR-TOF is a state-of-the-art instrument, operating under high vacuum in both positive and negative mode, whereas the device used to implement the interface is homemade, and operates only in positive mode (preventing the detection of many brominated compounds, Br^- for instance). Above all, the previous results were obtained using LDI and not L2MS configuration. Figure 5.24 shows both L2MS and LDI spectra of HIPS 10% DBDE recorded with the HR-TOF in positive mode. While it appears richer than that obtained by SR-TOF, the peaks observed in HR-L2MS are all associated with plastic only, Interestingly, the styrene peak (dehydrogenated) is intense in HR-L2MS (and does not present in LDI). while no DBDE or any bromine compound can be detected. From this point of view, the spectra recorded via the interface and using the HR-TOF are very similar.

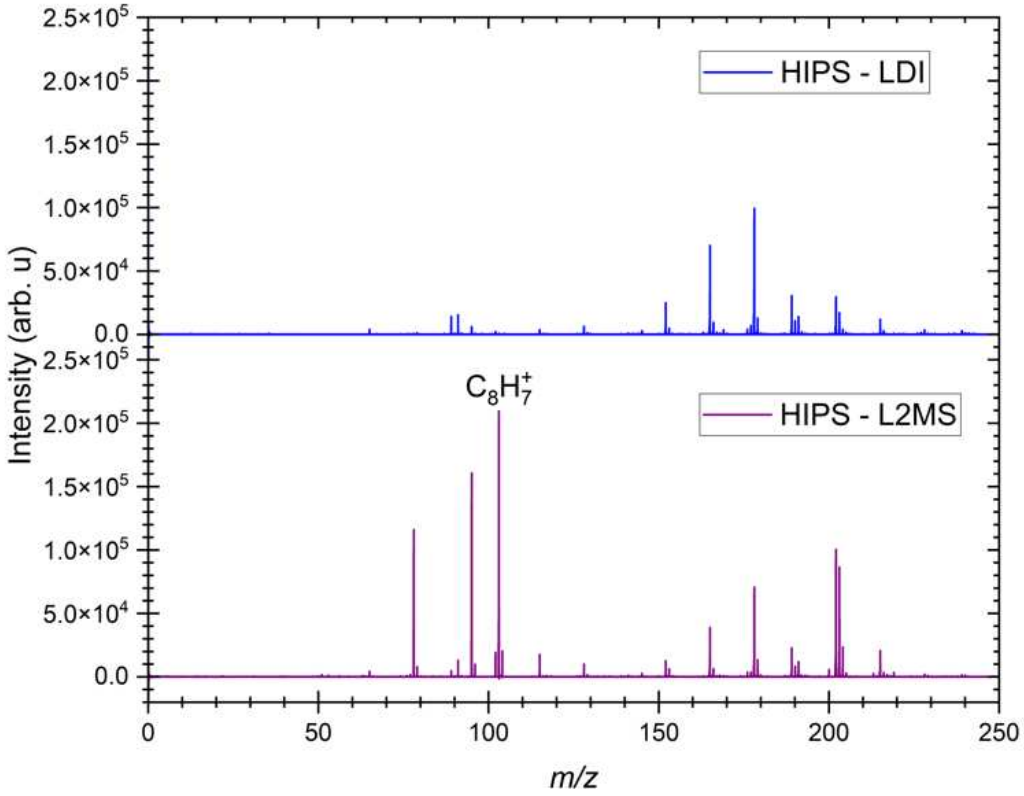

Figure 5.24 Positive polarity HR-LDI and L2MS mass spectra of mixture of 90wt% HIPS 10wt% DBDE

Chapter 6 Conclusion and Perspectives

This thesis is divided into two main parts. The first concerns the development and optimization of a new atmospheric pressure interface for two-stage laser mass spectrometry. The second part concerns the study of the degradation process of brominated flame retardants in plastics under UV-visible radiation. It provides a proof of concept for the interface developed in the first part.

The thesis begins with an in-depth discussion of mass spectrometry technics. The chapter 2 outlines the components of mass spectrometry, including the ionization source, mass analyzer, and the detector, and delves into the operation principles and classification.
In the development of atmospheric pressure interface coupled to mass spectrometry lots of research is going on. Firstly, they are classified based on their ionization technique. Then we explored the different solutions for sampling interface from atmosphere to MS, from pinhole sampling to continuous differential pressure sampling or discontinuous sampling interface.

Chapter 3 provides an in-depth examination of the experimental devices and methodologies employed from which we developed a coupling interface for analyzing solid samples at atmospheric pressure using mass spectrometry. The chapter delves into the analytical techniques utilized, including Two-Step Laser Mass Spectrometry (L2MS), Raman Spectroscopy, and FTIR spectroscopy, detailing their fundamental principles, experimental setups, and specific applications in this research.

A significant focus was placed on the steps of the L2MS technique, which integrates laser desorption, laser ionization, and ToF-MS. The chapter highlighted the differences between the homemade SR-L2MS instrument used for initial testing and the commercial and cutting-edge high-resolution HR-L2MS instrument used for brominated plastic analysis. In exploring laser desorption and ionization, the chapter discussed the interaction of laser light with solid targets and the subsequent processes of desorption, ablation, and ionization. We examined the importance of laser wavelength, irradiance, and synchronization in achieving efficient sample analysis.

Chapter 4 provides an examination of the development and optimization of the atmospheric interface for transferring samples from atmospheric pressure to a vacuum environment for analysis, through detailed descriptions of various configurations and their respective performances and limitations. The development and implementation of pulsed valves, including the construction of a custom pulse driver, were also covered, emphasizing their role in controlling gas flow and pressure within the vacuum chamber.

For liquid samples, two configurations utilizing a single valve were explored, differing mainly in its location in the sampling interface. For solid samples, a more extensive investigation was conducted, with five different configurations tested. These configurations varied in the number of valves and the positioning of the sampling interface within the vacuum chamber. Key findings highlighted the importance of tube length, valve operation timing, and the position of the sampling interface in achieving efficient molecule transfer.

The analysis of vapor samples, specifically kerosene, provided critical insights into the system's capability to handle volatile compounds. The synchronization of the ionization laser with the valve operation was crucial in ensuring effective ionization and accurate mass spectrometric analysis.

For solid samples, the experiments demonstrated that effective molecule transfer and ionization could be achieved through careful design and optimization of the sampling interface. The tests with pyrene, anthracene, naphthalene, phenanthrene, and pyrene revealed varying degrees of success, with certain configurations proving more effective in reducing molecule condensation, contamination of the vacuum chamber and enhancing signal strength. The synchronization studies highlighted the critical role of precise timing between valve operation and laser ionization in optimizing the system's performance. The velocity distribution measurements for different molecules underscored the need for tailored delays between valve opening, ionization, and desorption, and the necessity for a heating system of the interface to limit condensation.

Overall, this chapter demonstrated the development of an atmospheric interface capable of transferring both liquid and solid samples into a vacuum for mass spectrometric analysis. The iterative testing and refinement of various configurations led to significant improvements in molecule transfer efficiency and ionization accuracy. These advancements pave the way for further

research and optimization, ultimately enhancing the analytical capabilities of the system for a wide range of chemical samples.

Chapter 5 methodically explores the use of UV-visible irradiation as a viable method for the debromination of various plastics containing a Brominated Flame Retardants (BFRs), with a focused examination on Acrylonitrile Butadiene Styrene (ABS), Polycarbonate (PC), and High Impact Polystyrene (HIPS), both with and without the addition of Decabromodiphenyl Ether (DBDE). Through detailed Raman spectroscopy and mass spectrometry analyses, we have successfully identified the presence of DBDE in samples with DBDE by detecting characteristic bands associated with C-Br bands, specifically at Raman shifts of 225 cm^{-1} and 1523 cm^{-1}, among others. Analyzing non-irradiated samples using Raman spectroscopy was relatively straightforward due to minimal fluorescence interference. However, the Raman analysis of UV-visible irradiated samples proved challenging because of heightened fluorescence, which can mask the Raman bands. Attempts to mitigate this fluorescence by experimenting with various laser wavelengths were unsuccessful. While it still requires more refinement of analytical techniques to improve the detection and quantification of BFRs in complex matrices.

Analysis of irradiated sample was difficult using Raman spectroscopy due to which further analysis was done using FTIR spectroscopy and shows DBDE bands at 1354 cm^{-1}.

The irradiation experiments conducted with a Xenon lamp demonstrated that UV-visible light can effectively reduce the bromine content in these plastics, indicating the process's potential for enhancing the safety and environmental sustainability of recycling practices. The findings from the mass spectrometry analysis corroborate this, showing a significant reduction in bromine peaks for samples that experienced UV-vis irradiation, which further confirms the debromination effect.

In summary, this research contributes valuable insights into the debromination of BFR-containing plastics, an endeavor that holds significant implications for environmental health and safety. The persistence of BFRs in the environment and their potential health risks necessitate effective strategies for their removal from waste streams. Our study underscores the efficacy of UV-visible irradiation as a promising approach for the debromination of plastics containing PBDEs. Future work will need to focus on optimizing this process, exploring its applicability to a broader range of BFRs, and addressing the challenges identified during spectral analysis. By advancing our understanding and capabilities in this area, we can make significant strides toward mitigating the

impact of persistent organic pollutants and enhancing the sustainability of plastic recycling processes.

This work provided an opportunity to test the SR-TOF interface developed in the previous section on brominated plastics. The presence of styrene, characteristic of the plastics studied, is extremely encouraging, as it demonstrates the possibility to analyze more complex samples than the standard samples used up to now. If no brominated species was detected, they were also not detected in HR-TOF with analogous parameters.

Perspectives

The advancements made in this thesis regarding the development of the coupling interface pave the way for significant improvements in atmospheric mass spectrometry (MS) analysis. While various configurations were tested with different samples, there is substantial scope for further optimization and enhancement of the system.

One of the primary areas for future work involves refining the synchronization of critical parameters. Although we demonstrated the capability of transferring ambient analytes, achieving better alignment between the desorption, valve operation, and ionization timing could significantly enhance the signal quality. Fine-tuning these delays will ensure a more coherent and robust signal, improving the overall sensitivity and accuracy of the analysis.

Expanding the range of samples tested with the developed instrument is another important step forward. While the initial experiments provided valuable insights, a more extensive testing regimen involving a diverse array of samples will help in fine-tuning the instrument’s performance. This iterative process will lead to a more reliable and versatile tool, capable of handling a broader spectrum of analytes with greater efficiency.

The use of all-metal valves will also achieve more efficient heating, far beyond the 70°C use to prevent damage to the current valve's poppet. This should reduce residual contamination from more volatile species and further prevent any risk of condensation.

Automation also presents a promising avenue for improving the consistency and precision of sample analysis. Integrating a piezoelectric stage for automated sample movement could significantly enhance signal quality by precisely controlling the sample's positioning. This would ensure a fresh sample surface for each analysis and maintain an optimal distance between the sample and the sampling inlet. Such automation is not only expected to improve the consistency of measurements but also facilitate MS imaging at atmospheric pressure, opening new possibilities for detailed spatial analysis of samples.

Moreover, the system's versatility could be greatly enhanced by coupling it with high-resolution laser mass spectrometry (HR-L2MS) (see Figure 6.1) and complementary techniques such as Raman Spectroscopy and Laser-Induced Breakdown Spectroscopy (LIBS). These integrations would provide a multifaceted approach to sample analysis, combining the strengths of each method to yield more comprehensive data. For instance, while MS offers detailed mass analysis, Raman Spectroscopy can provide molecular structure information, and LIBS can deliver elemental composition. Together, they would create a powerful analytical toolkit capable of addressing complex scientific questions.

The work on the debromination of plastics and subsequent analysis using various techniques lays a strong foundation for future research into other brominated flame retardants (BFRs). This study's findings serve as a reference point, highlighting effective methods for BFR analysis and suggesting pathways for further investigation. Future studies can build on this foundation to explore the debromination and environmental impact of a wider range of BFRs, potentially leading to more environmentally friendly disposal and recycling methods for plastic waste.

In conclusion, the future perspectives for this research are vast and varied. By focusing on improving synchronization, expanding the range of tested samples, integrating automation, and coupling with additional analytical techniques, we can significantly enhance the capabilities and applications of atmospheric interface for MS analysis. The groundwork laid by this thesis offers a robust platform for future innovations, driving forward the field of environmental analysis and beyond.

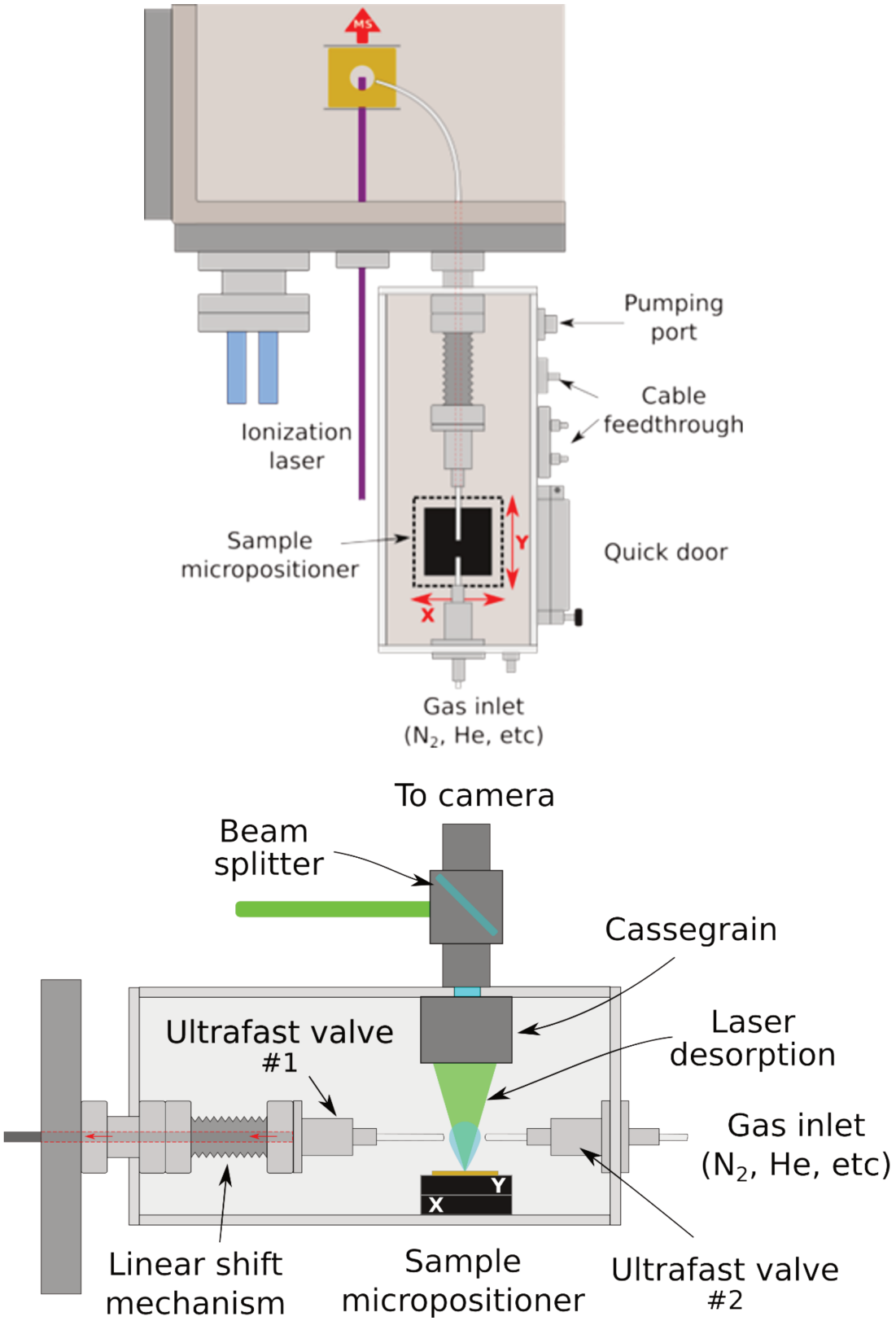

Figure 6.1 Schematic of the atmospheric pressure interface to be coupled to the HR-L2MS. It includes translation stages for imaging capacities.

References

[1] J. Laskin, A. Laskin, and S. A. Nizkorodov, 'Mass Spectrometry Analysis in Atmospheric Chemistry', *Anal Chem*, vol. 90, no. 1, pp. 166–189, Jan. 2018, doi: 10.1021/ACS.ANALCHEM.7B04249.

[2] S. Rankin-Turner and L. M. Heaney, 'Applications of ambient ionization mass spectrometry in 2020: An annual review', Apr. 01, 2021, *John Wiley and Sons Inc*. doi: 10.1002/ansa.202000135.

[3] Y. Pan, L. Hu, and T. Zhao, 'Applications of chemical imaging techniques in paleontology', Oct. 01, 2019, *Oxford University Press*. doi: 10.1093/nsr/nwy107.

[4] C. J. Perez, A. K. Bagga, S. S. Prova, M. Yousefi Taemeh, and D. R. Ifa, 'Review and perspectives on the applications of mass spectrometry imaging under ambient conditions', 2019, *John Wiley and Sons Ltd*. doi: 10.1002/rcm.8145.

[5] A. Römpp and B. Spengler, 'Mass spectrometry imaging with high resolution in mass and space', Jun. 2013. doi: 10.1007/s00418-013-1097-6.

[6] J. H. Gross, *Mass spectrometry: A textbook: Second edition*. Springer Berlin Heidelberg, 2011. doi: 10.1007/978-3-642-10711-5.

[7] Y. Wang, J. Sun, J. Qiao, J. Ouyang, and N. Na, 'A "soft" and "hard" Ionization Method for Comprehensive Studies of Molecules', *Anal Chem*, vol. 90, no. 24, pp. 14095–14099, Dec. 2018, doi: 10.1021/ACS.ANALCHEM.8B04437.

[8] D. M. Mazur, M. E. Zimens, T. B. Latkin, N. V. Ul'yanovskii, V. B. Artaev, and A. T. Lebedev, 'Reduction Reactions in the Ion Source in Electron Ionization Mass Spectrometry', *Journal of Analytical Chemistry*, vol. 75, no. 13, pp. 1685–1692, Dec. 2020, doi: 10.1134/S1061934820130092/TABLES/3.

[9] Y. Zhu and T. Lu, 'Ionization source for electrospray ionization mass spectrometry and MS analysis', US 9 , 972 , 481 B2, Oct. 21, 2016

[10] F. H. Field, 'Chemical Ionization Mass Spectrometry', *Ion-Molecule Reactions*, pp. 261–313, 1972, doi: 10.1007/978-1-4757-0088-6_6.

[11] J. T. Dowell, J. S. Hollis, and C. W. Russ, 'Chemical ionization source for mass spectrometry', 6,037,587, Oct. 17, 1997

[12] C. Dass, 'Fundamentals of contemporary mass spectrometry.', 2006, doi: 10.1002/0470118490.

[13] M. Z. Israr, D. Bernieh, A. Salzano, S. Cassambai, Y. Yazaki, and T. Suzuki, 'Matrix-assisted laser desorption ionisation (MALDI) mass spectrometry (MS): Basics and clinical applications', *Clin Chem Lab Med*, vol. 58, no. 6, pp. 883–896, Jun. 2020, doi: 10.1515/CCLM-2019-0868/XML.

[14] F. Hillenkamp, T. W. Jaskolla, and M. Karas, 'The MALDI Process and Method', *MALDI MS*, pp. 1–40, Nov. 2013, doi: 10.1002/9783527335961.CH1.

[15] L. Sangely *et al.*, 'Secondary Ion Mass Spectrometry', *Sector Field Mass Spectrometry for Elemental and Isotopic Analysis*, pp. 439–499, Nov. 2014, doi: 10.1039/9781849735407-00439.

[16] G. R. Parr and J. W. Taylor, 'Photoionization mass spectrometry IV. Carbon dioxide', *InternationaI Journal of Mass Spectrametry and Ion Physics*, vol. 14, pp. 467–477, 1974, doi: 10.1016/0020-7381(74)80077-X.

[17] R. Zimmermann and L. Hanley, *Photoionization and photo-induced processes in mass spectrometry : fundamentals and applications*. 2020. doi: 10.1002/9783527682201.
[18] 'Introduction to LC-MS Part6 : SHIMADZU (Shimadzu Corporation)'. Accessed: Oct. 10, 2024. [Online]. Available: https://www.shimadzu.com/an/service-support/technical-support/analysis-basics/lcms-intro/61intro.html
[19] W. Wang and Y. Li, 'Design and Implementation of an Orbitrap Mass Spectrometer Data Acquisition System for Atmospheric Molecule Identification', Apr. 25, 2023. doi: 10.20944/preprints202304.0922.v1.
[20] S. Eliuk and A. Makarov, 'Evolution of Orbitrap Mass Spectrometry Instrumentation', 2015, doi: 10.1146/annurev-anchem-071114-040325.
[21] P. B. Kyle, 'Toxicology: GCMS', *Mass Spectrometry for the Clinical Laboratory*, pp. 131–163, Jan. 2017, doi: 10.1016/B978-0-12-800871-3.00007-9.
[22] J. H. Barnes and G. M. Hieftje, 'Recent advances in detector-array technology for mass spectrometry', *Int J Mass Spectrom*, vol. 238, pp. 33–46, 2004, doi: 10.1016/j.ijms.2004.08.004.
[23] C. L. Feider, A. Krieger, R. J. Dehoog, and L. S. Eberlin, 'Ambient Ionization Mass Spectrometry: Recent Developments and Applications', Apr. 02, 2019, *American Chemical Society*. doi: 10.1021/acs.analchem.9b00807.
[24] N. M. Morato and R. G. Cooks, 'Desorption Electrospray Ionization Mass Spectrometry: 20 Years', *Acc Chem Res*, vol. 56, no. 18, pp. 2526–2536, Sep. 2023, doi: 10.1021/ACS.ACCOUNTS.3C00382.
[25] E. Sandström, C. Vettorazzo, C. L. Mackay, L. G. Troalen, and A. N. Hulme, 'Development and Application of Desorption Electrospray Ionization Mass Spectrometry for Historical Dye Analysis', *Anal Chem*, vol. 95, no. 11, pp. 4846–4854, Mar. 2023, doi: 10.1021/acs.analchem.2c03281.
[26] A. Hollerbach, S. Ayrton, A. Jarmusch, and R. G. Cooks, 'Desorption Electrospray Ionization: Methodology and Applications', *Encyclopedia of Spectroscopy and Spectrometry*, pp. 401–408, Jan. 2017, doi: 10.1016/B978-0-12-409547-2.12133-X.
[27] P. M. Lalli *et al.*, 'Fingerprinting and aging of ink by easy ambient sonic-spray ionization mass spectrometry', *Analyst*, vol. 135, no. 4, pp. 745–750, Mar. 2010, doi: 10.1039/B923398A.
[28] R. M. Alberici, P. H. Vendramini, and M. N. Eberlin, 'Easy ambient sonic-spray ionization mass spectrometry for tissue imaging', *Analytical Methods*, vol. 9, no. 34, pp. 5029–5036, Aug. 2017, doi: 10.1039/C7AY00858A.
[29] E. M. McBride *et al.*, 'Paper spray ionization: Applications and perspectives', *TrAC - Trends in Analytical Chemistry*, vol. 118, pp. 722–730, Sep. 2019, doi: 10.1016/J.TRAC.2019.06.028.
[30] Z. Ouyang *et al.*, 'Development, characterization, and application of paper spray ionization', *Anal Chem*, vol. 82, no. 6, pp. 2463–2471, Mar. 2010, doi: 10.1021/AC902854G.
[31] I. X. Peng, R. R. Ogorzalek Loo, E. Margalith, M. W. Little, and J. A. Loo, 'Electrospray-assisted laser desorption ionization mass spectrometry (ELDI-MS) with an infrared laser for characterizing peptides and proteins', *Analyst*, vol. 135, no. 4, pp. 767–772, Mar. 2010, doi: 10.1039/B923303B.
[32] C. Y. Cheng *et al.*, 'Electrospray-assisted laser desorption/ionization mass spectrometry for continuously monitoring the states of ongoing chemical reactions in organic or aqueous

solution under ambient conditions', *Anal Chem*, vol. 80, no. 20, pp. 7699–7705, Oct. 2008, doi: 10.1021/AC800952E.

[33] J. Shiea *et al.*, 'Electrospray-assisted laser desorption/ionization mass spectrometry for direct ambient analysis of solids', *Rapid Commun Mass Spectrom*, vol. 19, no. 24, pp. 3701–3704, 2005, doi: 10.1002/RCM.2243.

[34] K. T. Knizner *et al.*, 'Next-Generation Infrared Matrix-Assisted Laser Desorption Electrospray Ionization Source for Mass Spectrometry Imaging and High-Throughput Screening', *J Am Soc Mass Spectrom*, vol. 33, no. 11, pp. 2070–2077, Nov. 2022, doi: 10.1021/jasms.2c00178.

[35] J. S. Sampson, A. M. Hawkridge, and D. C. Muddiman, 'Generation and Detection of Multiply-Charged Peptides and Proteins by Matrix-Assisted Laser Desorption Electrospray Ionization (MALDESI) Fourier Transform Ion Cyclotron Resonance Mass Spectrometry', *J Am Soc Mass Spectrom*, vol. 17, no. 12, pp. 1712–1716, Dec. 2006, doi: 10.1016/j.jasms.2006.08.003.

[36] R. R. Kibbe, A. L. Mellinger, and D. C. Muddiman, 'Novel matrix strategies for improved ionization and spatial resolution using IR-MALDESI mass spectrometry imaging', *Journal of Mass Spectrometry*, vol. 57, no. 8, Aug. 2022, doi: 10.1002/jms.4875.

[37] E. Tobolkina, 'New analytical tools combining gel electrophoresis and mass spectrometry', 2014. doi: 10.13140/RG.2.1.4866.5125.

[38] R. E. Deimler, T. T. Razunguzwa, B. R. Reschke, C. M. Walsh, M. J. Powell, and G. P. Jackson, 'Direct analysis of drugs in forensic applications using laser ablation electrospray ionization-tandem mass spectrometry (LAESI-MS/MS)', *Analytical Methods*, vol. 6, no. 13, pp. 4810–4817, Jun. 2014, doi: 10.1039/C4AY01043D.

[39] S. C. Cheng, C. Shiea, Y. L. Huang, C. H. Wang, Y. T. Cho, and J. Shiea, 'Laser-based ambient mass spectrometry', *Analytical Methods*, vol. 9, no. 34, pp. 4924–4935, Aug. 2017, doi: 10.1039/C7AY00997F.

[40] S. C. Moyer, L. A. Marzilli, A. S. Woods, V. V Laiko, V. M. Doroshenko, and R. J. Cotter, 'Atmospheric Pressure Matrix-Assisted Laser Desorption/Ionization Mass Spectrometry', *Int J Mass Spectrom*, vol. 226, pp. 133–150, 2003.

[41] V. V. Laiko, M. A. Baldwin, and A. L. Burlingame, 'Atmospheric pressure matrix-assisted laser desorption/ionization mass spectrometry', *Anal Chem*, vol. 72, no. 4, pp. 652–657, Feb. 2000, doi: 10.1021/AC990998K.

[42] J. M. Daniel, S. Ehala, S. D. Friess, and R. Zenobi, 'On-line atmospheric pressure matrix-assisted laser desorption/ionization mass spectrometry', *Analyst*, vol. 129, no. 7, pp. 574–578, Jun. 2004, doi: 10.1039/B404178J.

[43] C. Creaser and L. Ratcliffe, 'Atmospheric Pressure Matrix-Assisted Laser Desorption/Ionisation Mass Spectrometry: A Review', *Curr Anal Chem*, vol. 2, no. 1, pp. 9–15, Dec. 2005, doi: 10.2174/157341106775197420.

[44] M. Woolman *et al.*, 'Optimized Mass Spectrometry Analysis Workflow with Polarimetric Guidance for ex vivo and in situ Sampling of Biological Tissues', *Sci Rep*, vol. 7, no. 1, Dec. 2017, doi: 10.1038/s41598-017-00272-y.

[45] M. Woolman *et al.*, 'Rapid determination of medulloblastoma subgroup affiliation with mass spectrometry using a handheld picosecond infrared laser desorption probe', *Chem Sci*, vol. 8, no. 9, pp. 6508–6519, 2017, doi: 10.1039/c7sc01974b.

[46] S. K. I. Funke *et al.*, 'Plug-and-play laser ablation-mass spectrometry for molecular imaging by means of dielectric barrier discharge ionization', *Anal Chim Acta*, vol. 1177, Sep. 2021, doi: 10.1016/j.aca.2021.338770.

[47] M. Bouza *et al.*, 'Ion Heating in Advanced Dielectric Barrier Discharge Ion Sources for Ambient Mass Spectrometry', *J Am Soc Mass Spectrom*, vol. 34, no. 6, pp. 1145–1152, Jun. 2023, doi: 10.1021/jasms.3c00087.

[48] Q. Lu, Z. Xu, X. You, S. Ma, and R. Zenobi, 'Atmospheric Pressure Mass Spectrometry Imaging Using Laser Ablation, Followed by Dielectric Barrier Discharge Ionization', *Anal Chem*, vol. 93, no. 15, pp. 6232–6238, Apr. 2021, doi: 10.1021/acs.analchem.1c00549.

[49] H. Wang *et al.*, 'Coupling laser desorption with corona beam ionization for ambient mass spectrometric analysis of solution and powder samples', *Talanta*, vol. 179, pp. 364–368, Mar. 2018, doi: 10.1016/j.talanta.2017.11.039.

[50] B. Fatou *et al.*, 'In vivo Real-Time Mass Spectrometry for Guided Surgery Application', *Sci Rep*, vol. 6, May 2016, doi: 10.1038/srep25919.

[51] N. Ogrinc *et al.*, 'Water-assisted laser desorption/ionization mass spectrometry for minimally invasive in vivo and real-time surface analysis using SpiderMass', *Nature Protocols 2019 14:11*, vol. 14, no. 11, pp. 3162–3182, Oct. 2019, doi: 10.1038/s41596-019-0217-8.

[52] N. Ogrinc *et al.*, 'Robot-Assisted SpiderMass forIn VivoReal-Time Topography Mass Spectrometry Imaging', *Anal Chem*, vol. 93, no. 43, pp. 14383–14391, Nov. 2021, doi: 10.1021/acs.analchem.1c01692.

[53] J. L. Berry *et al.*, 'Laser Ablation-Aerosol Mass Spectrometry-Chemical Ionization Mass Spectrometry for Ambient Surface Imaging', *Anal Chem*, vol. 90, no. 6, pp. 4046–4053, Mar. 2018, doi: 10.1021/acs.analchem.7b05255.

[54] B. A. Thomson, 'Atmospheric Pressure Ionization and Liquid Chromatography/Mass Spectrometry Together at Last', *J Am Soc Mass Spectrom*, vol. 9, no. 3, pp. 187–193, Mar. 1998, doi: 10.1016/S1044-0305(97)00285-7.

[55] E. C. Horning, M. G. Horning, D. I. Carroll, I. Dzidic, and R. N. Stillwell, 'New Picogram Detection System Based on a Mass Spectrometer with an External Ionization Source at Atmospheric Pressure', *Anal Chem*, vol. 45, no. 6, pp. 936–943, May 1973, doi: 10.1021/AC60328A035.

[56] S. Prosser, J. Henion, S. Thompson, and V. Parr, 'Atmospheric pressure ionization inlet for mass spectrometers', US 8.487,247 B2, Jul. 16, 2013

[57] M. M. Nudnova, L. Zhu, and R. Zenobi, 'Active capillary plasma source for ambient mass spectrometry', *Rapid Communications in Mass Spectrometry*, vol. 26, no. 12, pp. 1447–1452, Jun. 2012, doi: 10.1002/rcm.6242.

[58] L. Gao, R. G. Cooks, and Z. Ouyang, 'Breaking the pumping speed barrier in mass spectrometry: Discontinuous atmospheric pressure interface', *Anal Chem*, vol. 80, no. 11, pp. 4026–4032, Jun. 2008, doi: 10.1021/AC800014V.

[59] Y. Wei, C. Bian, Z. Ouyang, and W. Xu, 'A pulsed pinhole atmospheric pressure interface for simplified mass spectrometry instrumentation with enhanced sensitivity', *Rapid Communications in Mass Spectrometry*, vol. 29, no. 8, pp. 701–706, Apr. 2015, doi: 10.1002/rcm.7140.

[60] R. Sto *et al.*, 'Nanoscale Atmospheric Pressure Laser Ablation-Mass Spectrometry', *Int. J. Mass Spectrom. Ion Processes*, vol. 44, no. 1, pp. 1399–1402, 1984, doi: 10.1021/ac001440b.

[61] P. Setz, T. Schmitz, R. Z.-R. of scientific instruments, and undefined 2006, 'Design and performance of an atmospheric pressure sampling interface for ion-trap/time-of-flight mass spectrometry', *aip.scitation.org*, vol. 77, no. 2, 2006, doi: 10.1063/1.2165550.

[62] T. A. Schmitz, G. Gamez, P. D. Setz, L. Zhu, and R. Zenobi, 'Towards nanoscale molecular analysis at atmospheric pressure by a near-field laser ablation ion trap/time-of-flight mass spectrometer', *Anal Chem*, vol. 80, no. 17, pp. 6537–6544, Sep. 2008, doi: 10.1021/AC8005044.

[63] L. Zhu, J. Stadler, T. A. Schmitz, F. Krumeich, and R. Zenobi, 'Atmospheric pressure sampling for laser ablation based nanoscale imaging mass spectrometry: Ions or neutrals?', *Journal of Physical Chemistry C*, vol. 115, no. 4, pp. 1006–1013, Feb. 2011, doi: 10.1021/JP105178Q.

[64] T. R. Covey, B. A. Thomson, and B. B. Schneider, 'Atmospheric pressure ion sources', *Mass Spectrom Rev*, vol. 28, no. 6, pp. 870–897, Nov. 2009, doi: 10.1002/MAS.20246.

[65] A. Faccinetto, C. Focsa, P. Desgroux, and M. Ziskind, 'Progress toward the Quantitative Analysis of PAHs Adsorbed on Soot by Laser Desorption/Laser Ionization/Time-of-Flight Mass Spectrometry', *Environ Sci Technol*, vol. 49, no. 17, pp. 10510–10520, Sep. 2015, doi: 10.1021/ACS.EST.5B02703.

[66] R. Kelly and A. Miotello, 'Comments on explosive mechanisms of laser sputtering', *Appl Surf Sci*, pp. 205–215, 1996, doi: 10.1016/0169-4332(95)00481-5.

[67] L. V. Zhigilei, E. Leveugle, B. J. Garrison, Y. G. Yingling, and M. I. Zeifman, 'Computer simulations of laser ablation of molecular substrates', *Chem Rev*, vol. 103, no. 2, pp. 321–347, Feb. 2003, doi: 10.1021/CR010459R.

[68] R. F. Haglund, 'Microscopic and mesoscopic aspects of laser-induced desorption and ablation', *Appl Surf Sci*, vol. 96–98, pp. 1–13, Apr. 1996, doi: 10.1021/ac990998k.

[69] L. V Zhigilei and B. J. Garrison, 'Microscopic mechanisms of laser ablation of organic solids in the thermal and stress confinement irradiation regimes', *J. Appl. Phys*, vol. 88, pp. 1281–1298, 2000, doi: 10.1063/1.373816.

[70] S. M. Eggins, L. P. J. Kinsley, and J. M. G. Shelley, 'Deposition and element fractionation processes during atmospheric pressure laser sampling for analysis by ICP-MS', *Appl Surf Sci*, vol. 127, 1998, doi: 10.1016/S0169-4332(97)00643-0.

[71] D. Günthera and C. A. Heinrichb, 'Comparison of the ablation behaviour of 266 nm Nd5YAG and 193 nm ArF excimer lasers for LA-ICP-MS analysis', Sep. 1999. doi: 10.1039/A901649J.

[72] T. E. Jeffriesa, N. J. G. Pearcea, W. T. Perkins, and A. Raithb, 'Chemical Fractionation During Infrared and Ultraviolet Laser Ablation Inductively Coupled Plasma Mass Spectrometry-Implications for Mineral Microanalysis', 1996. doi: 10.1039/AC9963300035.

[73] R. E. Russo, X. Mao, H. Liu, J. Gonzalez, and S. S. Mao, 'Laser ablation in analytical chemistry-a review', *Talanta*, vol. 57, pp. 425–451, 2002, doi: 10.1016/s0039-9140(02)00053-x.

[74] S. S. Mao, X. Mao, R. Greif, and R. E. Russo, 'Simulation of a picosecond laser ablation plasma', *Appl. Phys. Lett*, vol. 76, pp. 3370–3372, 2000, doi: 10.1063/1.126651.

[75] S. S. Mao, X. Mao, R. Greif, and R. E. Russo, 'Initiation of an early-stage plasma during picosecond laser ablation of solids', *Appl. Phys. Lett*, vol. 77, pp. 2464–2466, 2000, doi: 10.1063/1.1318239.

[76] X. Mao and R. E. Russo, 'Observation of plasma shielding by measuring transmitted and reflected laser pulse temporal profiles', Springer-Verlag, 1997. doi: 10.1007/s003390050437.
[77] H. C. Liu, X. L. Mao, J. H. Yoo, and R. E. Russo, 'Early phase laser induced plasma diagnostics and mass removal during single-pulse laser ablation of silicon', *Spectrochimica Acta Part B*, vol. 54, no. 11, pp. 1607–1624, 1999, doi: 10.1016/S0584-8547(99)00092-0.
[78] J. L. Holmes, C. Aubry, and P. M. Mayer, 'Assigning Structures to Ions in Mass Spectrometry', *J Am Soc Mass Spectrum*, vol. 18, 2007, doi: 10.1016/j.jasms.2007.02.014.
[79] 'Welcome to the NIST WebBook'. Accessed: Dec. 11, 2023. [Online]. Available: https://webbook.nist.gov/
[80] P. Desgroux, X. Mercier, and K. A. Thomson, 'Study of the formation of soot and its precursors in flames using optical diagnostics', 2012, doi: 10.1016/j.proci.2012.09.004.
[81] W. C. Wiley and I. H. McLaren, 'Time-of-flight mass spectrometer with improved resolution', *Review of Scientific Instruments*, vol. 26, no. 12, pp. 1150–1157, 1955, doi: 10.1063/1.1715212.
[82] B. A. Mamyrin, 'Time-of-flight mass spectrometry (concepts, achievements, and prospects)', *International Jornal of Mass Spectrometry*, vol. 206, pp. 251–266, 2001, doi: 10.1016/S1387-3806(00)00392-4.
[83] U. Boesl, 'Time-of-flight mass spectrometry: Introduction to the basics', Jan. 01, 2017, *John Wiley and Sons Inc.* doi: 10.1002/mas.21520.
[84] J. Fjeldsted, 'Time-of-Flight Mass Spectrometry Technical Overview', Dec. 2003, [Online]. Available: https://www.agilent.com/cs/library/technicaloverviews/Public/5989-0373EN%2011-Dec-2003.pdf
[85] M. Guilhaus, 'Principles and Instrumentation in Time-of-flight Mass Spectrometry Physical and Instrumental Concepts', *JOURNAL OF MASS SPECTROMETRY*, vol. 30, pp. 1519–1532, 1995, doi: 10.1002/jms.1190301102.
[86] 'DET210-HIGH-SPEED SILICON DETECTOR DESCRIPTION', [Online]. Available: www.thorlabs.com
[87] M. Prochazka, 'Basics of Raman Scattering (RS) Spectroscopy', in *Surface-Enhanced Raman Spectroscopy: Bioanalytical, Biomolecular and Medical Applications*, Cham: Springer International Publishing, 2016, pp. 7–19. doi: 10.1007/978-3-319-23992-7_2.
[88] D. Wu, R. Burton, G. Schoenau, and D. Bitner, 'Modelling of orifice flow rate at very small openings', *International Journal of Fluid Power*, vol. 4, no. 1, pp. 31–39, Oct. 2003, doi: 10.1080/14399776.2003.10781153.
[89] B. B. High-Tech, 'EL-FLOW® Select series Thermal Mass Flow Meters and Controllers Instruction Manual', 2023. [Online]. Available: www.bronkhorst.com/int/about/conditions-of-sales/
[90] 'MODEL DG535 Digital Delay / Pulse Generator', 1994, [Online]. Available: https://www.thinksrs.com/downloads/pdfs/manuals/DG535m.pdf
[91] C. Koch *et al.*, 'Degradation of polymeric brominated flame retardants: Development of an analytical approach using PolyFR and UV irradiation', *Environ Sci Technol*, vol. 50, no. 23, pp. 12912–12920, Dec. 2016, doi: 10.1021/acs.est.6b04083.
[92] C. Koch *et al.*, 'Degradation of the Polymeric Brominated Flame Retardant "polymeric FR" by Heat and UV Exposure', *Environ Sci Technol*, vol. 53, no. 3, pp. 1453–1462, Feb. 2019, doi: 10.1021/acs.est.8b03872.

[93] H. Oumeddour *et al.*, 'Degradation processes of brominated flame retardants dispersed in high impact polystyrene under UV–visible radiation', *Waste Management and Research*, 2023, doi: 10.1177/0734242X231219626.
[94] Clarke Frederic B., 'The effects of brominated flame retardants on the elements of fire hazard: a re-examination of earlier results', *Fire Mater*, vol. 23, no. 3, pp. 109–116, Sep. 1999, doi: 10.1002/(SICI)1099-1018(199905/06)23:3<109::AID-FAM674>3.0.CO;2-W.
[95] 'Brominated Flame Retardant: Function and Effectiveness for Protection from Flame - LEVITEX'. Accessed: Dec. 05, 2024. [Online]. Available: https://levitex.com/brominated-flame-retardant/
[96] L. Minet *et al.*, 'High Production, Low Information: We Need to Know More about Polymeric Flame Retardants', *Environ Sci Technol*, vol. 55, no. 6, pp. 3467–3469, Mar. 2021, doi: 10.1021/ACS.EST.0C08126.
[97] S. Ling *et al.*, 'Distribution characteristics and risks assessment of brominated flame retardants in surface soil from both a legacy and a new e-waste dismantling site', *J Clean Prod*, vol. 373, p. 133970, 2022, doi: 10.1016/j.jclepro.2022.133970.
[98] M. Alaee, P. Arias, A. Sjödin, and A. ˚ Ke Bergman, 'An overview of commercially used brominated flame retardants, their applications, their use patterns in different countries/regions and possible modes of release', 2003, doi: 10.1016/S0160-4120(03)00121-1.
[99] M. F. Fernandez *et al.*, 'PBDEs and PBBs in the adipose tissue of women from Spain', vol. 28, p. 101, 2006, doi: 10.1016/j.chemosphere.2006.04.065.
[100] L. Liu, X. Zhen, X. Wang, D. Zhang, L. Sun, and J. Tang, 'Spatio-temporal variations and input patterns on the legacy and novel brominated flame retardants (BFRs) in coastal rivers of North China *', 2021, doi: 10.1016/j.envpol.2021.117093.
[101] A. Bocio, J. M. Llobet, J. L. Domingo, J. Corbella, A. Teixidó, and C. Casas, 'Polybrominated diphenyl ethers (PBDEs) in foodstuffs: Human exposure through the diet', *J Agric Food Chem*, vol. 51, no. 10, pp. 3191–3195, May 2003, doi: 10.1021/JF0340916.
[102] M. Sharkey, S. Harrad, M. Abou-Elwafa Abdallah, D. S. Drage, and H. Berresheim, 'Phasing-out of legacy brominated flame retardants: The UNEP Stockholm Convention and other legislative action worldwide', 2020, doi: 10.1016/j.envint.2020.106041.
[103] R. K. Benmammar *et al.*, 'Electron Beam Processing as a Promising Tool to Decontaminate Polymers Containing Brominated Flame Retardants', *Molecules 2023, Vol. 28, Page 7753*, vol. 28, no. 23, p. 7753, Nov. 2023, doi: 10.3390/MOLECULES28237753.
[104] L. S. Birnbaum and D. F. Staskal, 'Brominated flame retardants: Cause for concern?', 2004, *Public Health Services, US Dept of Health and Human Services*. doi: 10.1289/ehp.6559.
[105] G. Söderström, U. Sellström, C. A. De Wit, and M. Tysklind, 'Photolytic Debromination of Decabromodiphenyl Ether (BDE 209)', *Environ Sci Technol*, vol. 38, no. 1, pp. 127–132, Jan. 2004, doi: 10.1021/ES034682C.
[106] N. Kajiwara, Y. Noma, and H. Takigami, 'Photolysis Studies of Technical Decabromodiphenyl Ether (DecaBDE) and Ethane (DeBDethane) in Plastics under Natural Sunlight', *Environ Sci Technol*, vol. 42, no. 12, pp. 4404–4409, 2008, doi: 10.1021/es800060j.
[107] M. Y. Shin *et al.*, 'Polybrominated Diphenyl Ethers in Maternal Serum, Breast Milk, Umbilical Cord Serum, and House Dust in a South Korean Birth Panel of Mother-Neonate Pairs', *International Journal of Environmental Research and Public Health 2016, Vol. 13, Page 767*, vol. 13, no. 8, p. 767, Jul. 2016, doi: 10.3390/IJERPH13080767.

[108] R. Renner, 'Government Watch: In US, flame retardants will be voluntarily phased out', *Environ Sci Technol*, pp. 14A-14A, 2004.
[109] Y. Wang, G. Jiang, P. K. S. Lam, and A. Li, 'Polybrominated diphenyl ether in the East Asian environment: A critical review', *Environ Int*, vol. 33, no. 7, pp. 963–973, Oct. 2007, doi: 10.1016/J.ENVINT.2007.03.016.
[110] M. J. La Guardia, R. C. Hale, and E. Harvey, 'Detailed polybrominated diphenyl ether (PBDE) congener composition of the widely used penta-, octa-, and deca-PBDE technical flame-retardant mixtures', *Environ Sci Technol*, vol. 40, no. 20, pp. 6247–6254, Oct. 2006, doi: 10.1021/ES060630M.
[111] Y. Su, H. Hung, E. Sverko, P. Fellin, and H. Li, 'Multi-year measurements of polybrominated diphenyl ethers (PBDEs) in the Arctic atmosphere', *Atmos Environ*, vol. 41, no. 38, pp. 8725–8735, Dec. 2007, doi: 10.1016/J.ATMOSENV.2007.07.032.
[112] 'BIS(PENTABROMOPHENYL) ETHER SUMMARY RISK ASSESSMENT REPORT', 2003. [Online]. Available: https://echa.europa.eu/documents/10162/0d251331-31ea-4963-aeb0-f97ea886d594
[113] S. Olivera, H. B. Muralidhara, K. Venkatesh, K. Gopalakrishna, and C. S. Vivek, 'Plating on acrylonitrile–butadiene–styrene (ABS) plastic: a review', Apr. 01, 2016, *Springer New York LLC*. doi: 10.1007/s10853-015-9668-7.
[114] K. Takeuchi, '5.16 - Polycarbonates', in *Polymer Science: a Comprehensive Reference: Volume 1-10*, vol. 1–10, Elsevier, 2012, pp. 363–376. doi: 10.1016/B978-0-444-53349-4.00148-5.
[115] J. A. Jansen, 'Characterization of the Structure and Properties of PPE+HIPS'. [Online]. Available: https://madisongroup.com/characterization-of-the-structure-and-properties-of-ppe-hips/
[116] S. Ghosal and J. Wagner, 'Correlated Raman micro-spectroscopy and scanning electron microscopy analyses of flame retardants in environmental samples: A micro-analytical tool for probing chemical composition, origin and spatial distribution', *Analyst*, vol. 138, no. 13, pp. 3836–3844, Jul. 2013, doi: 10.1039/C3AN00501A.
[117] T. Sormunen *et al.*, 'Characterizing plastics containing brominated flame retardants with combined LIBS and Raman spectroscopy', *J Phys Conf Ser*, vol. 2346, no. 1, 2022, doi: 10.1088/1742-6596/2346/1/012014.
[118] G. Bikulčius, I. Ignatjev, and A. Ručinskiene, 'Rapid method to determine suitability of ABS plastics for metallisation', *Transactions of the Institute of Metal Finishing*, vol. 92, no. 1, pp. 47–51, Jan. 2014, doi: 10.1179/0020296713Z.000000000138.